MODELING GRANULAR MATERIAL MIXING AND SEGREGATION USING A FINITE ELEMENT METHOD AND ADVECTION-DIFFUSION-SEGREGATION EQUATION MULTI-SCALE MODEL

by

Yu Liu

A Thesis

Submitted to the Faculty of Purdue University

In Partial Fulfillment of the Requirements for the degree of

Doctor of Philosophy

School of Mechanical Engineering

West Lafayette, Indiana

May 2019

THE PURDUE UNIVERSITY GRADUATE SCHOOL
STATEMENT OF COMMITTEE APPROVAL

Dr. Carl Wassgren, Co-chair
School of Mechanical Engineering
Dr. Marcial Gonzalez, Co-chair
School of Mechanical Engineering
Dr. Steven Son
School of Mechanical Engineering
Dr. R.P. Kingsly Ambrose
School of Agricultural & Biological Engineering

Approved by:
Dr. Jay P. Gore
Head of the Graduate Program

Dedicated to my beloved parents

ACKNOWLEDGMENTS

I would like to thank those who helped me though the process of completing this thesis. First, I would like to express the deepest appreciation to Prof. Carl Wassgren and Prof. Marcial Gonzalez, my advisors, who guided me and supported me to grow as a researcher. Without their guidance and persistent help this thesis would not have been possible. Thanks to Prof. Kingsly Ambrose and Prof. Steven Son for their service as my committee members and their valuable feedback and help. Thanks to the whole research group who gave me suggestions and ideas. Specially, I appreciate Rohit Kumar for his accompany at lab and Shrikant Swaminathan for his guidance and support.

I am also grateful to the School of Mechanical Engineering at Purdue University, the Graduate School at Purdue University and the United States Department of Energy for financial support.

In addition, I want to thank my parents. They give all their love to me and supported every decision I made. Their support allows me to concentrate on my research works. I also want to thank my girlfriend, Rose. She gave me the motivation to pursue my degree and supported me through all the hard time. Finally, I want to thank all my friends for their support and love. I will miss all the time I spent with them and all the games we played.

TABLE OF CONTENTS

LIST OF TABLES

LIST OF FIGURES

NOMENCLATURE

c	material concentration
D	diffusion coefficient
v	velocity
$\dot{\gamma}$	shear rate
d	particle diameter
D_{drum}	drum diameter
W_{drum}	drum width
k_1	spanwise diffusion constant
k_2	streamwise diffusion constant
τ	shear stress
σ	normal stress
$\bar{c}$	cohesion
f_i	internal friction angle
ε	strain
E	Young's modulus
ν	Poisson's ratio
δ	perpendicular distance along the center of the drum bed
h	maximum level depth of the drum bed
I	segregation intensity
σ^2	measured variance of concentration
${\sigma_0}^2$	variance of concentration for a fully segregated system
${\sigma_r}^2$	variance of concentration for a randomly mixed system
N_s	number of samples
N_p	number of particles
N_n	number of nodes
Fr	Froude number
f_w	wall friction angle
ρ	material density

g	gravity
ω	rotation speed
f_v	filling volume fraction
RSD	relative standard deviation
v_p	percolation velocity
S	percolation length scale
R_0	radius of the rotating drum
x_i	the mass fraction of fines collected in a given sample
x_f	the initial mass fraction of fines
M	cumulative mass discharged
M_{total}	initial total mass inside the hopper

ABSTRACT

Author: Liu, Yu. PhD
Institution: Purdue University
Degree Received: May 2019
Title: Modeling Granular Material Mixing and Segregation Using a Finite Element Method and Advection-Diffusion-Segregation Equation Multi-Scale Model
Committee Chair: Carl Wassgren and Marcial Gonzalez

Granular material blending plays an important role in many industries ranging from those that manufacture pharmaceuticals to those producing agrochemicals. The ability to create homogeneous powder blends can be critical to the final product quality. For example, insufficient blending of a pharmaceutical formulation may have serious consequences on product efficacy and safety. Unfortunately, tools for quantitatively predicting particulate blending processes are lacking. Most often, parameters that produce an acceptable degree of blending are determined empirically.

The objective of this work was to develop a validated model for predicting the magnitude and rate of granular material mixing and segregation for binary mixtures of granular material in systems of industrial interest. The model utilizes finite element method simulations to determine the bulk-level granular velocity field, which is then combined with particle-level diffusion and segregation correlations using the advection-diffusion-segregation equation.

An important factor to the success of the finite element method simulation used in the current work is the material constitutive model used to represent the granular flow behavior. In this work, the Mohr-Coulomb elastoplastic (MCEP) model was used. The MCEP model parameters were calibrated both numerically and experimentally and the procedure is described in the current work. Additionally, the particle-level diffusion and segregation correlations are important to the accurate prediction of mixing and segregation rates. The current work derived the diffusion and segregation correlations from published literatures and determined a methodology for obtaining the particle diffusion and segregation parameters from experiments.

The utility of this modelling approach is demonstrated by predicting mixing patterns in a rotating drum and Tote blender as well as segregation patterns in a rotating drum and during the discharge

of conical hoppers. Indeed, a significant advantage of the current modeling approach compared to previously published models is that arbitrary system geometries can be modeled.

The model predictions were compared with both DEM simulation and experiment results. The model is able to quantitatively predict the magnitude and rate of powder mixing and segregation in two- and three-dimensional geometries and is computationally faster than DEM simulations. Since the numerical approach does not directly model individual particles, this new modeling approach is well suited for predicting mixing and segregation in large industrial-scale systems.

CHAPTER 1. INTRODUCTION

Blending of particulate materials is a common manufacturing unit operation and plays an important role in many industries, such as those that produce chemicals, pharmaceuticals, food products, and agrochemicals. Generating a homogeneous mixture can be critical to product quality and performance and, thus, proper design and operation of a blending operation is essential [1]. Unintentionally heterogeneous powder blends can result in inconsistencies during processing and unacceptable product quality. For example, insufficient blending of a pharmaceutical formulation may have serious consequences on product efficacy and safety.

A wide variety of blenders are available in the marketplace [2,3]. Unfortunately, predictive engineering design of industrial powder blenders remains underdeveloped due to the lack of quantitative modeling tools. As a result, design and scale-up of blending equipment often relies on empirical studies and parameters that produce an acceptable degree of blending are determined empirically. Numerical simulations using the discrete element method (DEM) have been used in recent years to predict blending unit operations and are considered state-of-the-art. However, this modeling approach is not well-suited for modeling industrial-scale blenders due to computational limitations [4]. These models must assume particle sizes orders of magnitude larger than the true particle sizes [5–11]. This assumption calls into question the quantitative accuracy of the predictions, particularly at smaller scales of scrutiny. Moreover, determining particle-level input parameters to use in such models is challenging and not widely agreed upon [12–14].

In this work, we present a new multi-scale modeling approach for predicting mixing and segregation of granular materials in different geometries. A finite element method (FEM) simulation is used to predict the shape of the material domain and the advective flow field. The velocity field results are used within a finite difference formulation of the advection-diffusion-segregation (ADS) equation, which predicts the concentration evolution, i.e., mixing and segregation, of the material. The model is considered multi-scale in the sense that a continuum model is used for bulk flow behavior while a local model is used for particle diffusive behavior.

In the multi-scale model, the diffusion and segregation parameters used within the ADS equation were calibrated through experiments or derived from previous literature. Different geometries were considered, such as the rotating drum, the Tote blender, and conical hoppers. The model is able to quantitatively predict the magnitude and rate of powder mixing and segregation in two- and three-dimensional geometries and is computationally faster than DEM simulations. This new modeling approach is well suited for predicting mixing and segregation in industrial-scale systems, which are beyond the scope of current DEM modeling techniques.

CHAPTER 2. BACKGROUND

The components of a granular mixture typically have different properties, such as size and shape, which can result in the segregation of the components. Many phenomena can result in segregation, such as vibration-driven percolation and convection [15–17] and elutriation [18]. In particular, gravity-driven segregation in dense, sheared granular flows, known as shear-driven percolation [19–21], is a common mechanism that occurs during industrial processing. In shear-driven percolation, small particles have a larger probability of falling through the gaps that form between larger particles when the particle assembly is subject to shear. As a result, smaller particles collect below the shear layer leaving the larger particles at the top [19,20,22–26].

The computational discrete element method (DEM) has been used extensively for predicting particle mixing and segregation dynamics and is considered state-of-the-art [7,11,27,28]. DEM simulations are particularly helpful for understanding blending physics at the particle level. For example, recent DEM simulations by Fan et al. [29] and Khola et al. [30] produced expressions for particle diffusion coefficients and segregation rates using simple heap flow and shear cell geometries, respectively. Other studies have investigated the effects of particle size, shape and cohesion, also in simple geometries [27,28,31,32]. Although these studies have provided valuable qualitative insight, they are limited in their quantitative predictions by computational requirements, at least using realistic particle sizes. Typical DEM simulations model on the order of 10^6 particles at most, with some simulations reaching as many as 10^8 particles. However, even a small, lab-scale blender containing 100 μm particles contains more than 10^{10} particles, far exceeding what is possible to model with standard computational tools. Typically, to maintain the same fill level in the model that is used in the real process, particle sizes are made artificially larger in the DEM simulations, often by two to three orders of magnitude. Although DEM can still produce qualitatively reasonable behavior using such large particles, it is not clear that the models are accurate quantitatively. Indeed, previous work [27,33] has shown that particle size can have an influence on the rate and extent of blending. Hence, DEM may not produce quantitatively accurate results for systems of industrial interest

In addition to issues related to particle size, the use of DEM simulations also requires knowledge of a number of particle material properties, such as elastic modulus and Poisson's ratio, and particle interaction properties, such as coefficients of restitution and sliding and rolling friction coefficients. Direct measurements of these properties are often impractical, particularly for particles smaller than 1 mm. Often, parametric studies are performed to determine the sensitivity of the simulation results on the unknown properties in order to account for parameter value uncertainty. Back-fitting of bulk simulation results to bulk experimental measurements is becoming increasingly common, but questions remain as to whether (a) different sets of parameters might also fit the experimental results well, and (b) inaccuracies in the DEM model are disguised by parameter fitting [12,14]. Ideally, those simulations would rely on a small number of well-defined, easy-to-perform bulk level measurements.

Besides computational DEM models, analytical continuum models have also been proposed for modeling mixing and segregation [19,34,35]. A number of studies have modeled shear-driven percolation segregation using a continuum approach that incorporates advection due to mean flow, percolation-driven segregation, and diffusion [19,34–39]. Most of these models were used to gain a qualitative understanding of the complex physics while some showed good agreement with experiments [40,41]. Recently developed continuum models utilized discrete element method (DEM) simulations to derive particle diffusion and segregation correlations at a local, i.e., particle-level, scale and combined these correlations with analytically-derived advection fields at the macro-scale [31,42,43]. Predictions from these studies were shown to be quantitatively accurate compared with DEM-only simulations and experiments. However, since they depend on analytical solutions for the macroscopic flow field, their use is restricted to simple two-dimensional geometries, such as a simple heap flow.

A variety of flows have been studied using the continuum approach, such as chute [31,38,40], plug [35], annular shear [37], and rotating drum [42] flows. However, the domains of these flows were simple, two-dimensional geometries amenable to analytical solutions for the macroscopic flow field. Indeed, the shear layers in these geometries are often approximated as having linear or exponential velocity profiles located at a free surface.

To study more complex geometries, a computational approach is needed for obtaining the macroscopic flow field. For continuum modeling, this means that a constitutive model describing the stress-strain behavior is required. Many constitutive models have been developed to describe granular flow dynamics, such as the Schaeffer model [44,45], the μ(I) model [46–48], and the hydrodynamic model [49–51]. These models have been used to predict the flow behavior of granular materials in more complex configurations than those studied analytically, such as silos and hoppers [47,49,50], a high-shear granulator [48], and an asymmetric double cone mixer [51]. Although good agreement with DEM simulations and experiments have been observed for several aspects of these flows, such as velocity fields and wall stress profiles [50,52], these flows were still mainly restricted to two-dimensional geometries. Recently, finite element method (FEM) simulations with Drucker–Prager [53–55] and Mohr-Coulomb [56–58] constitutive material models have been used to study the granular flow behavior in both two- and three-dimensional systems, and quantitatively accurate predictions were observed. The advantages of using FEM simulations with an elasto-plastic material model over previous constitutive models are that (a) unsteady granular flows in three-dimensional configurations can be simulated, and (b) experimental characterization of the required material properties is usually straightforward using, for example, standard shear cell equipment.

Only recently have researchers begun to combine computationally predicted velocity fields with expressions for particle diffusion and segregation. For example, Bertuola et al. [59] predicted segregation in a discharging two-dimensional hopper using segregation correlations derived by Fan et al. [31] and Hajra et al. [60], and combined these correlations with flow field predictions using a hydrodynamic model for particle flow. The model was able to quantitatively predict the degree of segregation compared with published experiments after key model parameters were fitted to the experimental data. It is worth noting that the hydrodynamic model used to simulate the macroscopic flow behavior was less accurate than the one predicted by a Mohr-Coulomb model [57,58]. Bai et al. [61] used an FEM model assuming Mohr-Coulomb constitutive behavior to predict the velocity field in a cylindrical, bladed mixer, which was shown to be qualitatively accurate compared to DEM simulations. They also predicted the degree of blending by assuming convective mixing only, but observed a dependence of the mixing rate on FEM mesh size.

CHAPTER 3. THESIS GOAL AND OBJECTIVES

Based on the prior research in the field of granular material mixing and segregation modeling, the following goal and objectives are proposed for this thesis work.

3.1 Thesis goal

Develop a validated model for predicting the magnitude and rate of granular material mixing and segregation in systems of industrial interest.

3.2 Thesis objectives

The following objectives are derived for this thesis work:

- Develop a finite element method (FEM) model with Mohr-Coulomb material properties to predict the advective flow field of granular materials.
- Develop a multi-scale model that combines particle diffusion and segregation correlations with the advective flow field information from FEM simulations to predict the mixing and segregation of granular materials.
- Determine a methodology for obtaining the Mohr-Coulomb material properties.
- Determine a methodology for obtaining the particle diffusion and segregation correlations.
- Develop experiments using different equipment to validate that the multi-scale model is able to quantitatively predict the magnitude and rate of granular material mixing and segregation.
- Extend the multi-scale model to study the mixing and segregation of materials with different material properties.

CHAPTER 4. TWO-DIMENSIONAL MULTI-SCALE MIXING MODEL

* The content of this chapter has been published in the AIChE Journal (doi:10.1002/aic.16179).

This chapter investigates mixing in a rotating drum using the multi-scale modeling approach. Section 4.1 introduces the finite element modeling approach and its implementations; Section 4.2 describes the advection-diffusion equation used in the multi-scale model and the numerical method used to solve it; Section 4.3 describes the DEM simulations used for comparison and the material calibration methods; Section 4.4 describes the comparisons between the DEM simulations and multi-scale model predictions; Section 4.5 describes the parametric studies performed to help understand the effects of different parameters in the multi-scale model.

4.1 Finite element method model

A three-dimensional FEM model is used in the present chapter to provide predictions of the advective flow field in a cylindrical rotating drum. Prior works by Zheng and Yu [56,57] have shown that FEM models can provide good predictions of the flow behavior of bulk granular materials. The following sub-sections describe the FEM model implementations used in the present chapter.

4.1.1 Model geometry and boundary conditions

The FEM model used here is derived from the one described by Zheng and Yu [56]. For convenience, several aspects of this model are presented here. The commercial FEM package Abaqus/Explicit V6.14 is used to perform the simulations. The system geometry is shown in Figure 4.1 for a lab scale rotating drum with a diameter of 140 mm. A narrow width of 1 cm is used for computational efficiency. Note that both the front and back sides of the Eulerian mesh are regarded as planes of symmetry in the model, which is analogous to having periodic boundaries. The drum wall is meshed separately as a rigid shell, with the only degree of freedom being rotation about the z axis. The rotational speed remains constant throughout the simulations and equal to 6 rpm (0.628 rad/s). Gravity is included in the model with $g = 9.8$ m/s^2 directed in the negative y direction.

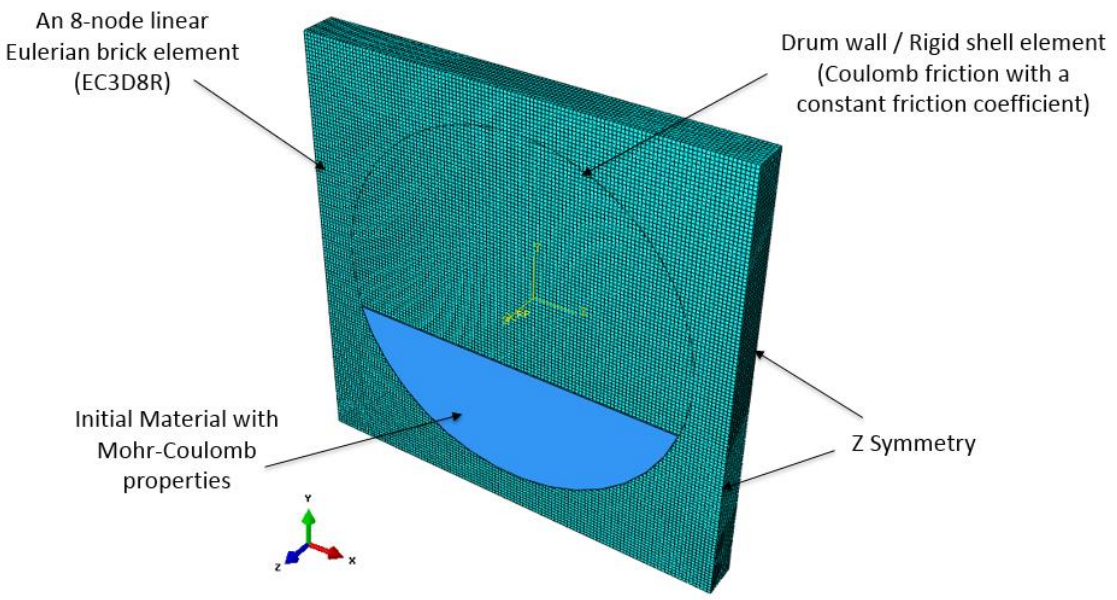

Figure 4.1 A schematic of the geometry modeled in the FEM simulations.

Because the material in the drum is anticipated to deform substantially, an Eulerian element formulation is used in the model to contend with potential mesh distortion issues. The entire simulation domain is modeled using 8-node, linear, Eulerian brick elements (EC3D8R) while the drum circumference is assumed to be a non-deformable, frictional, Lagrangian boundary. Within the Eulerian domain, the material stress-strain behavior is modeled using the Mohr-Coulomb elastoplastic (MCEP) model. Upon yielding, the material flows plastically. The continuity equation is discretized using a coupled Eulerian-Lagrangian formulation to efficiently model free surfaces and rigid walls. Details of this model can be found in Abaqus documentation [62]. Previous work [56–58] has shown that the MCEP model can describe the behavior of flowing granular materials well. Moreover, as reported by Zheng and Yu [56], the Young's modulus, Poisson's ratio, and bulk density of the material have little influence on the material flow behavior and, hence, can be treated as constant values. Note that although the FEM algorithm includes inertial terms in the momentum equation, there is no stress dependence on strain rate in the MCEP material model. There are other constitutive models available that do include strain-rate effects [63,64]. The methodology for obtaining the MCEP material properties used within the simulation are described in the following sections.

4.1.2 Abaqus implementation

Since an Eulerian element formulation is used in the current model to eliminate mesh distortion, the Coupled Eulerian-Lagrangian (CEL) approach in Abaqus is applied to handle interactions between the highly deformable material elements and stiff wall elements. Details of this approach can be found in the Abaqus documentation [62]. In the Eulerian framework, elements do not represent specific masses of material, but instead represent specific regions in space. The volume of material within an element is represented by the Eulerian Volume Fraction (EVF). A value of EVF = 0 indicates that no material is present in the element while EVF = 1 indicates that the element is completely filled with material.

All Eulerian elements were initially empty (EVF = 0) and the initial bed state was generated by filling a fraction of the elements with material (EVF = 1), which is highlighted in blue in Figure 4.1. Next, the material was allowed to settle as the gravitational acceleration was slowly increased from zero to its final value. At this point, the drum was allowed to rotate and the simulation was considered started. This gravity-varying filling procedure was used to fill the drum and reduce the time needed for the material to completely settle before rotation. The filling level of the drum, defined as the maximum level bed depth divided by the drum diameter, was 0.35.

Although the current chapter uses the FEM model to predict the macroscopic flow field in a rotating cylindrical drum, several trials were also performed to investigate the material stresses in the drum. Zheng and Yu [56] showed that the CEL approach does not impose specific requirements on the shape or dimensions of the Eulerian element mesh since the mesh can cover the entire domain of the modeled system. However, in the current work it was observed that the predicted material stresses are sensitive to the Eulerian domain shape. Figure 4.2 shows two different meshing schemes for the Eulerian domain. Figure 4.2(a) is the rectangular structured mesh used by Zheng and Yu while Figure 4.2(b) is a cylindrical structured mesh tested in the current work. Note that the central hole in Figure 4.2(b) is used to maintain the structured mesh for the cylindrical domain and does not affect the results since there is no material within that region. Mesh dependence tests were carried out for both meshing algorithms to verify that the meshes were sufficiently resolved for the moving system. As shown in Figure 4.3, the cylindrical structured mesh provides better predictions of the hydrostatic stress field, especially near the rigid drum wall,

since this meshing geometry ensures that the rigid wall does not cut through Eulerian elements and allows for better contact detection. Nevertheless, since the current work does not rely on a predicted stress field, no further study was performed on this topic. As mentioned previously, the mesh geometry plays little role on the velocity field; hence, a rectangular structured mesh was used due to its computational efficiency.

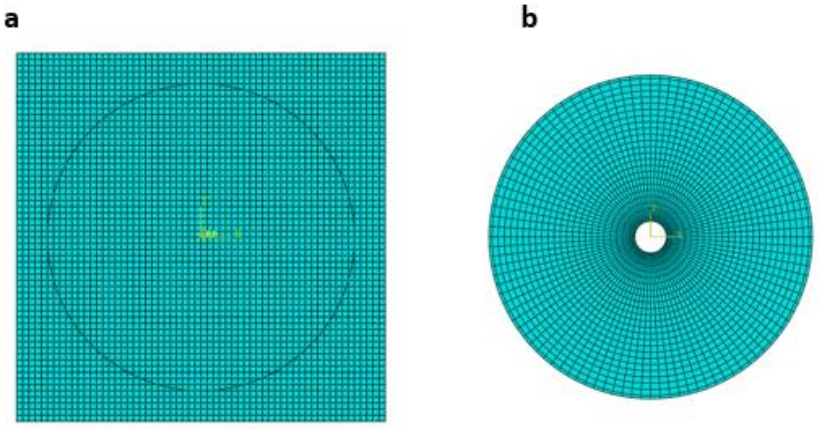

Figure 4.2 Two different meshing algorithms for the cylindrical drum (side view): (a) rectangular structured mesh, (b) cylindrical structured mesh, for the Eulerian domain.

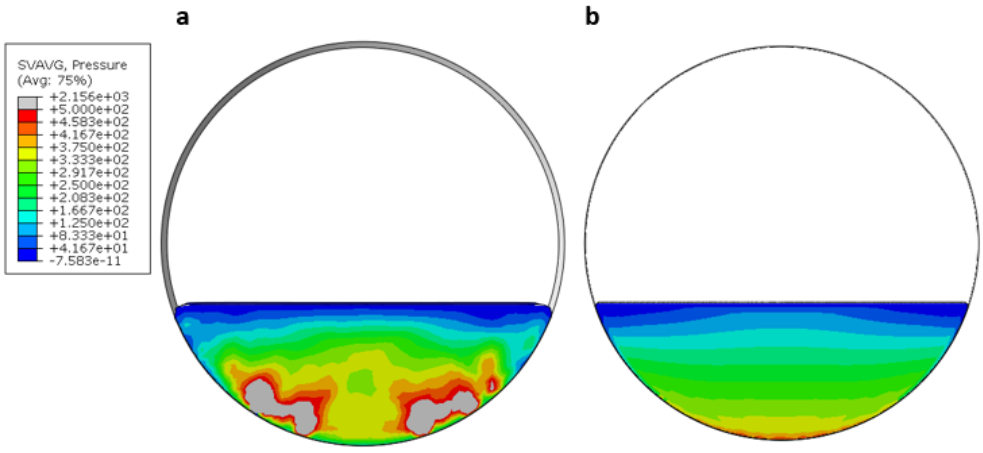

Figure 4.3 Stress distributions for the two meshes shown in Figure 4.2 when gravity is applied: (a) rectangular structured mesh, (b) cylindrical structured mesh. The colors represent pressure in Pascals.

4.2 The multi-scale mixing model

4.2.1 Advection-diffusion equation

As mentioned previously, the FEM simulations provide only the velocity field information for material movement in the blender. Hence, in order to model the spatiotemporal evolution of the concentration of a particular material species, *c*, an additional model is needed. This model is the advection-diffusion equation,

$$\frac{\partial c}{\partial t} = \nabla \cdot \left(\boldsymbol{D} \nabla c \right) - \nabla \cdot \left(\boldsymbol{v} c \right), \tag{4.1}$$

where *c* is the local concentration of a particular species of material, $\boldsymbol{D}$ is the diffusion coefficient for that species, and $\boldsymbol{v}$ is the local advective velocity vector. For simplicity, incompressible flow is assumed in the current work, which gives the local mass conservation equation,

$$\nabla \cdot \boldsymbol{v} = 0 . \tag{4.2}$$

Previous studies [31,42,65] have been devoted to understanding the underlying mechanisms governing particle mixing and segregation and developing analytical and numerical methods for predicting blending dynamics. These modeling frameworks incorporated advective movement of material using either DEM simulation measurements or theoretical expressions for simple geometries, such as steady flow down a free surface. The primary difference with the present work is that the advective flow field is generated using an FEM model, which greatly increases the types and sizes of systems that can be modeled.

Since the current system of interest, a cylindrical rotating drum, is nominally two-dimensional, the advection-diffusion equation is simplified for a two-dimensional case. Note that there are no significant limitations to modeling fully three-dimensional flows, however. Since the current model only focuses on self-diffusion during blending, no segregation is considered. Chapter 6 will incorporate a segregation component into the multi-scale modeling framework.

Previous works [31,42] have treated the self-diffusion coefficient $\boldsymbol{D}$ as a constant value for simplicity. However, studies [66–68] have shown that $\boldsymbol{D}$ is, in fact, a tensor quantity with components D_{ij}. Utter et al. [66] found that the off-diagonal components D_{xy} and D_{yx} are an order of magnitude smaller than the diagonal components D_{xx} and D_{yy} and, hence, can be reasonably

ignored. The advection-diffusion equation (Eq. (4.1)) written in index notation and making use of Eq. (4.2) is,

$$\frac{\partial c}{\partial t} = \frac{\partial}{\partial x_i}\left(D_{ij} \frac{\partial c}{\partial x_j} \right) - v_i \frac{\partial c}{\partial x_i}, \tag{4.3}$$

which may be expanded to give,

$$\frac{\partial c}{\partial t} = \left(\frac{\partial D_{xx}}{\partial x} - v_x \right) \frac{\partial c}{\partial x} + D_{xx} \frac{\partial^2 c}{\partial x^2} + \left(\frac{\partial D_{yy}}{\partial y} - v_y \right) \frac{\partial c}{\partial y} + D_{yy} \frac{\partial^2 c}{\partial y^2}, \tag{4.4}$$

taking into account the diffusion coefficient assumptions. Utter et al. [66] also found that the particle diffusivity is proportional to the local shear rate and is approximately 1.9 times larger along the mean flow direction than it is in the perpendicular direction. A similar relationship has been reported by Hsiau et al. [67]. More recently, Fan et al. [29] measured the self-diffusion coefficient *D* in the spanwise direction of a heap flow and found that when the shear rate is not too small,

$$D \sim \dot{\gamma} \bar{d}^2, \tag{4.5}$$

where $\dot{\gamma}$ is the local shear rate in the direction perpendicular to bed free surface and $\bar{d}$ is the local mean particle diameter.

Combining Eq. (4.5) with Utter et al.'s relationship and dividing the local shear rate into *x* and *y* directions, the shear rate-dependent diffusion coefficient ***D*** can be written as,

$$\begin{aligned} D_{xx} &= k_1 \dot{\gamma}_y \bar{d}^2 + k_2 \dot{\gamma}_x \bar{d}^2 \\ D_{yy} &= k_1 \dot{\gamma}_x \bar{d}^2 + k_2 \dot{\gamma}_y \bar{d}^2 \end{aligned}. \tag{4.6}$$

where $\dot{\gamma}_y = \left| \partial v_y / \partial x \right|$ and $\dot{\gamma}_x = \left| \partial v_x / \partial y \right|$. The constant k_1 can be found from experiments or small-scale DEM simulations. In the current work, k_1 = 0.04, which is derived from the previous computational work by Fan et al. [29]. Making use of Utter et al.'s findings, $k_2 = 1.9k_1$.

4.2.2 Numerical method

Many numerical techniques have been developed to solve the advection diffusion equation, such as the finite difference method, finite element method, finite volume method, and the domain decomposition method. Previous works [31,42,65] also introduced an operator splitting approach,

which solves the advection step and a combined diffusion and segregation step separately. A matrix mapping method is used in these previous works due to its high accuracy [69]. Since the current model is two-dimensional and only self-diffusion is considered, a finite difference method using a central explicit scheme is used here to solve Eq. (4.4) due to its simplicity and computational efficiency.

Previous work [70] has shown that a simple combination of individual finite differences in different axes without appropriate cross terms can cause numerical instability. The generalization of explicit finite difference schemes for the advection-diffusion equation to multiple dimensions is not simply the sum of individual one-dimensional contributions. Hence, in order to maintain a high computational efficiency without losing accuracy, a second-order Tylor Lax-Wendroff scheme is used in the current model to rewrite Eq. (4.4) as,

$$c_{ij}^{n+1} = c_{ij}^{n} - \left[\nu_x \Delta_{x0} c_{ij}^{n} - \left(\frac{1}{2}\nu_x^2 + \mu_x \right) \delta_x^2 c_{ij}^{n} \right] - \left[\nu_y \Delta_{y0} c_{ij}^{n} - \left(\frac{1}{2}\nu_y^2 + \mu_y \right) \delta_y^2 c_{ij}^{n} \right] + \nu_x \nu_y \Delta_{x0} \Delta_{y0} c_{ij}^{n} \quad (4.7)$$

where,

$$\nu_x = \frac{\left[v_x + \Delta_{x0} \left(D_{xx} \right)_{ij} \right] \Delta t}{\Delta x}, \quad (4.8)$$

$$\nu_y = \frac{\left[v_y + \Delta_{y0} \left(D_{yy} \right)_{ij} \right] \Delta t}{\Delta y}, \quad (4.9)$$

$$\mu_x = \left(D_{xx} \right)_{ij} \frac{\Delta t}{\Delta x^2}, \quad (4.10)$$

$$\mu_y = \left(D_{yy} \right)_{ij} \frac{\Delta t}{\Delta y^2}, \quad (4.11)$$

$$\Delta_{x0} c_{ij}^{n} = \frac{c_{i,j+1}^{n} - c_{i,j-1}^{n}}{2}, \quad (4.12)$$

$$\Delta_{y0} c_{ij}^{n} = \frac{c_{i+1,j}^{n} - c_{i-1,j}^{n}}{2}, \quad (4.13)$$

$$\delta_x^2 c_{ij}^{n} = c_{i,j+1}^{n} - 2c_{ij}^{n} + c_{i,j-1}^{n}, \quad (4.14)$$

$$\delta_y^2 c_{ij}^n = c_{i+1,j}^n - 2c_{ij}^n + c_{i-1,j}^n , \tag{4.15}$$

$$\Delta_{x0}\Delta_{y0} c_{ij}^n = \frac{\left(c_{i+1,j+1}^n - c_{i-1,j+1}^n - c_{i+1,j-1}^n + c_{i-1,j-1}^n\right)}{4}, \tag{4.16}$$

$$\Delta_{x0}\left(D_{xx}\right)_{ij} = \frac{\left(D_{xx}\right)_{i,j+1} - \left(D_{xx}\right)_{i,j-1}}{2}, \quad \text{and} \tag{4.17}$$

$$\Delta_{y0}\left(D_{yy}\right)_{ij} = \frac{\left(D_{yy}\right)_{i+1,j} - \left(D_{yy}\right)_{i-1,j}}{2}. \tag{4.18}$$

This finite difference formula is illustrated using the computational molecule shown in Figure 4.4, which can be used independently of the directions of the velocity components. Details of this scheme, including its Taylor series expansion and the iteration process, can be found in the work by Sousa [70].

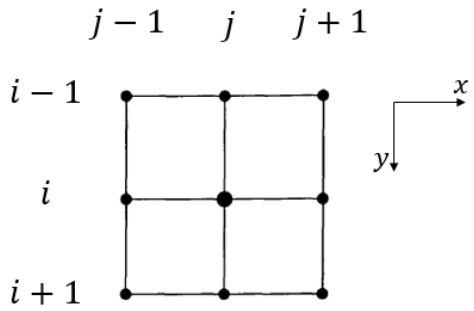

Figure 4.4 Computational molecule for the second-order Taylor-Wendroff scheme. The larger circle denotes the center node.

Note that since an explicit finite difference scheme is used here, solutions of the current model are not unconditionally stable. Hence, the Von Neumann conditions must be checked before the iteration to ensure the stability of the numerical computations. Details of this stability analysis can be found in the published literature [70]. However, in practice, an easier way to ensure numerical stability is to continuously decrease the time step until reaching a critical value below which the numerical computation remains stable. Using this approach, the time step in the current model is

determined as 5e-4 s (20,000 time steps per drum rotation) with the grid length of 3e-4 m (467 elements span the drum diameter).

To determine the initial particle concentrations used in the multi-scale model, the material region in the FEM model was divided into two equal parts by assigning two different material colors as shown in Figure 4.5(a). All of the materials had the same properties, however. The drum was then allowed to move in an unsteady fashion according to the FEM predictions as the drum started to rotate and the material advected until a steady velocity field was achieved, which occurred after 0.25 revolutions (Figure 4.5(b)). Particle diffusion was not considered during this stage of the model. This assumption is addressed further in the following sections. Once a steady velocity field was established in the FEM model, the velocity components were then used within the advection-diffusion equation (Eq. (4.4)) to model material mixing.

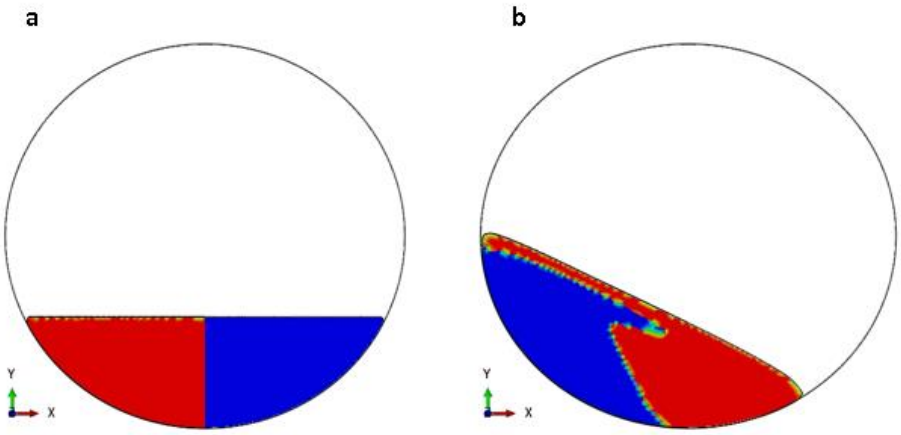

Figure 4.5 Material concentration distributions from a typical FEM simulation (a) initial filling and (b) after reaching steady state.

Because a steady state velocity field was used in the current model, the boundaries of the material domain remained the same throughout the entire computation. Hence, a control volume boundary condition was used in the current model and no moving boundary was considered. Note that in computational fluid dynamics (CFD) simulations, a polynomial fitting approach is often used and the species concentration of the boundary node is set equal to the extrapolated value of inner nodes of the control volume [71]. The same idea was used in the current algorithm and the material

concentration of the boundary node was set to equal the value of the node that was one grid point inward.

Post-processing of the FEM simulation data was required to determine the extent of the material domain. As mentioned previously, the computational mesh in an Eulerian FEM does not represent the material and instead, the Eulerian Volume Fraction (EVF) is used to determine the volume and position of materials within the Eulerian mesh. Hence, nodal EVF values for the two materials must be generated first so that empty elements and boundaries can be identified.

A MATLAB program was used to iterate the finite difference form of the advection-diffusion equation given in Eq. (4.7). After obtaining the material domain and steady velocity field information from the FEM simulation, initial conditions were interpolated into a structured rectangular mesh that covered the entire material domain. The grid width was determined such that it was sufficiently small to achieve a converged result. Iteration was used for all interpolated nodes and a threshold was set to ensure the material concentration value remained between 0 and 1. As described previously, a small time step was carefully chosen to ensure the stability of the explicit scheme.

4.3 Discrete element method (DEM) simulations

4.3.1 DEM rotating drum simulation

Although DEM simulation is not well suited for industrial-scale blenders, it can still accurately predict the mixing and segregation for large particles [5–11]. Thus, a three-dimensional DEM model with large particles was developed in the current work to compare to the predictions from the multi-scale model. The commercial DEM package EDEM^{TM} (DEM Solutions, Inc., Lebanon, NH) was used to perform the simulation. The system geometry is shown in Figure 4.6(a). Note that the front and back boundaries were periodic, consistent with the FEM model although the FEM symmetric boundary condition did not allow for material movement through the boundary while the DEM periodic boundaries did. Note that previous work has shown that sidewall friction can play an important role in the surface flow dynamics [72]. In the simulation, a drum was filled with two different colored, but otherwise identical, spherical particles, which were initially separated side by side as shown in Figure 4.6(b). Once the bed was fully settled, the drum rotated

at a constant speed and the particle began mixing. The DEM parameters used in the simulation are listed in Table 4.1.

Table 4.1 DEM simulation parameters.

Parameter	Value
Drum diameter (mm)	140
Domain width (mm)	10
Number of particles (-)	53445
Particle diameter (mm)	1
Particle density (kg/m3)	2500
Particle shear modulus (MPa)	10
Poisson’s ratio (-)	0.3
Particle-particle friction coefficient (-)	0.4
Particle-wall friction coefficient (-)	0.3
Rolling friction coefficient (-)	0.01
Filling level (% of max level depth)	35
Rotation speed (rpm)	6
Simulated time (s)	30

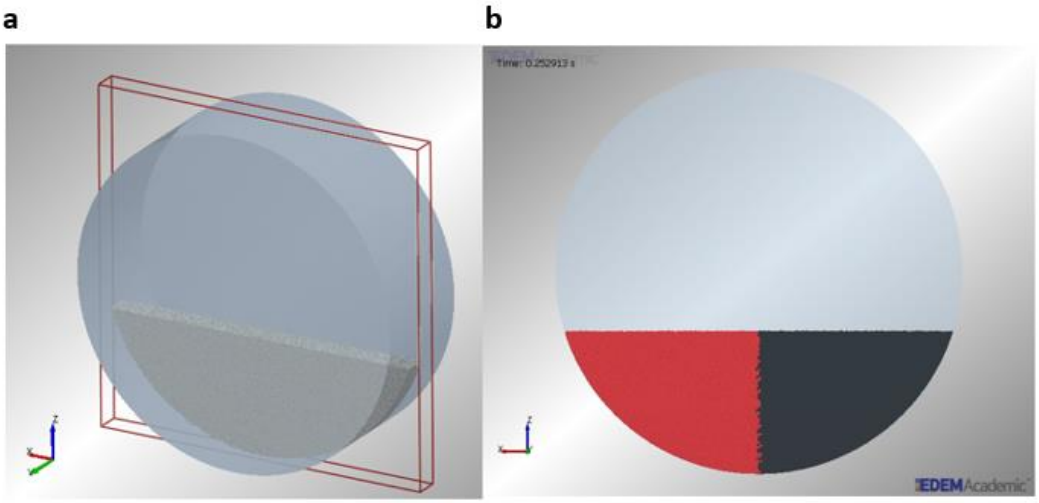

Figure 4.6 DEM simulation: (a) drum and domain geometry; (b) initial state.

4.3.2 Calibration of material properties

In order to justify a comparison between the multi-scale model and the DEM simulations, the Mohr-Coulomb properties used in the FEM simulations were determined from the DEM particle properties specified in Table 4.1. The Mohr-Coulomb properties, namely the internal friction angle, cohesion, and dilation angle, were calibrated using a DEM simulation of an annular shear cell with periodic boundaries (Figure 4.7(a)). Analogous to a real annular shear tester, vertical fins were attached to the top and bottom plates to ensure failure within the material. A constant normal pressure was applied to the top plate while the bottom plate moved with a constant rotation speed and the tangential shear stress was recorded and evaluated to determine the bulk internal friction angle after a constant stress level was reached.

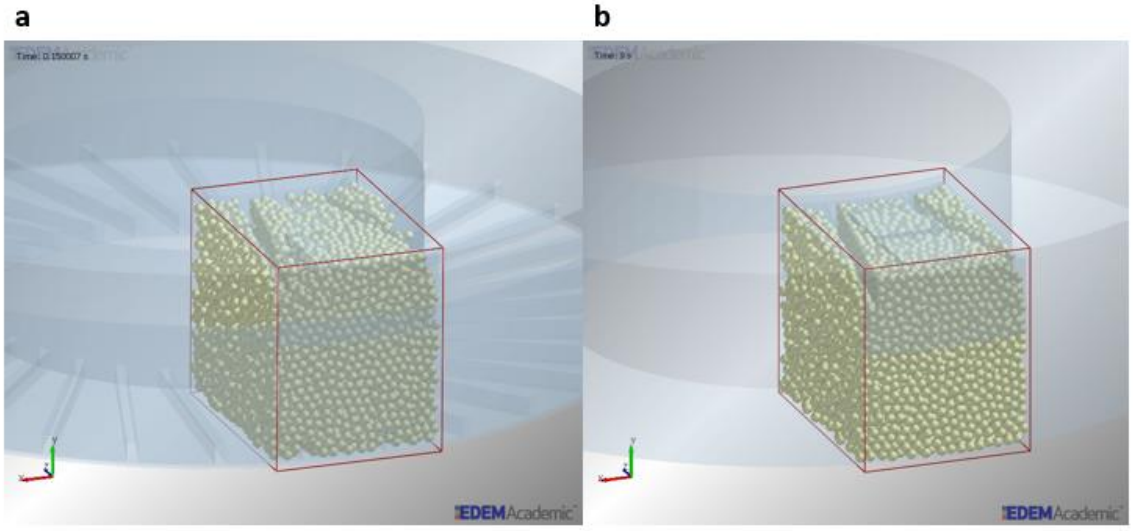

Figure 4.7 A snapshot showing the computational domain for the DEM annular shear cell simulations for (a) internal friction angle and (b) wall friction angle. Periodic boundary conditions are used in the *x* direction.

The defining feature of a Mohr-Coulomb material is its shear failure criterion,

$$\tau = \bar{c} + \sigma \cdot \tan(f_i), \tag{4.19}$$

where τ and σ are the failure shear stress and the applied normal stress acting on the failure plane, respectively. The parameter $\bar{c}$ is the bulk cohesion of the material and the parameter f_i is the internal friction angle of the material. These parameters were found using two different shear cell simulations with different top plate normal pressures: one at 2 kPa and the other at 4 kPa. Figure 4.8 plots the results from these two simulations along with a best fit line based on a least squares fit to Eq. (4.19). The results clearly demonstrate that the bulk material can be treated as cohesionless (c = 0) with an internal friction angle of 23.6°. The dilation angle of material was set to 0.1° since the dilation of cohesionless granular materials is usually small, as stated by Zheng and Yu [56]. A wall friction simulation was also performed using a similar DEM annular shear cell, but with a flat bottom boundary surface, to determine the material-wall friction angle. This simulation gave a bulk material-wall friction coefficient of 0.324, which is close to the particle-wall friction coefficient.

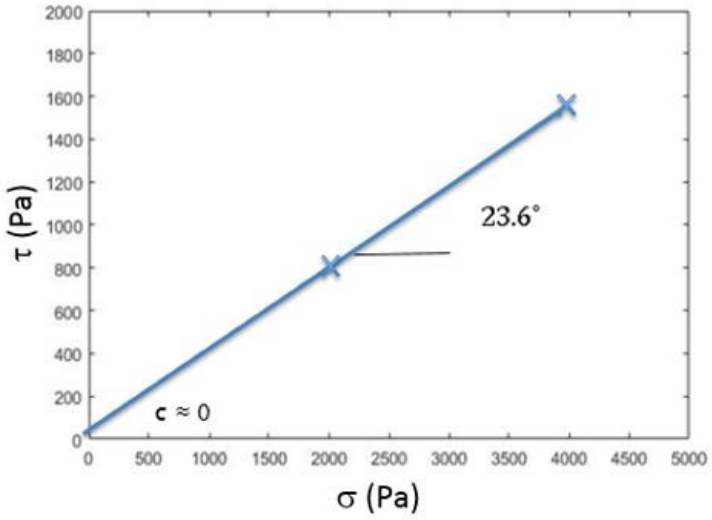

Figure 4.8 Critical state shear stress plotted as a function of the applied normal stress from the DEM shear cell simulations using the material properties listed in Table 4.1. Two data points are shown in the plot along with a fitting line.

Although previous work [56] has indicated that Mohr-Coulomb FEM simulations of bulk material flow is insensitive to the elastic modulus, Poisson's ratio, and bulk density of the material, they were still measured from the DEM simulations in the current work for completeness. The bulk density was taken to be 0.6 of the particle density, which is consistent with loosely packed, non-cohesive spheres. The bulk elastic parameters, namely, elastic modulus E and Poisson's ratio ν, were obtained from a separate uniaxial compression DEM simulation in which the axial and radial stresses were measured as a function of axial strain during both compression and decompression of the material, as shown in Figure 4.9. The initial slope of the unloading curves were used to compute both parameters,

$$\nu = \frac{\frac{d\sigma_{rr}}{d\varepsilon_{zz}^{e}}}{\frac{d\sigma_{rr}}{d\varepsilon_{zz}^{e}} + \frac{d\sigma_{zz}}{d\varepsilon_{zz}^{e}}}, \tag{4.20}$$

$$E = \frac{d\sigma_{zz}}{d\varepsilon_{zz}^{e}} - 2\nu\frac{d\sigma_{rr}}{d\varepsilon_{zz}^{e}}, \tag{4.21}$$

where σ_{zz} is the axial stress, σ_{rr} is the radial stress, and ε^{e}_{zz} is the elastic axial strain. Details of this method can be found in the work of Swaminathan et al [73].

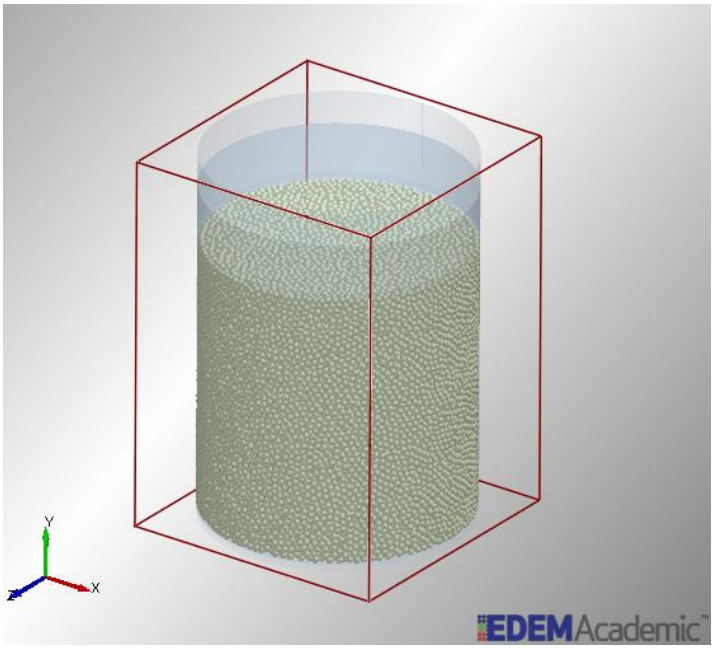

Figure 4.9 A snapshot showing the computational domain for the DEM uniaxial compression simulations.

Figure 4.10 shows the compression and decompression curves from the DEM simulation using the properties listed in Table 4.1. Previous work [73–75] has shown that the bulk elastic properties are functions of the relative density, which in turn is a function of the applied stress. From the FEM simulation, the stresses acting on material vary throughout the drum. Several DEM uniaxial compression simulations with maximum applied stresses between 20 kPa and 40 kPa have been performed and give values of (elastic modulus, Poisson's ratio) between (2.8 MPa, 0.055) and (3.7 MPa, 0.065). For simplicity, the elastic properties used in the current FEM model were determined for a single stress condition corresponding to Figure 4.10. The bulk elastic modulus E and Poisson's ratio ν determined for this condition were 3.65 MPa and 0.065, respectively. Previous works [73–75] have shown that the Poisson's ratio ν is typically small at relative densities near the poured relative density for a variety of different materials, which is consistent with the value measured in the current work. As mentioned previously, the bulk material flow behavior is insensitive to the elastic modulus and Poisson's ratio so the variation in elastic properties is expected have little influence on the results. Indeed, FEM simulations performed as part of this work with different elastic properties produced little variation in the bulk material kinematics. A summary of the FEM simulation material parameters is given in Table 4.2. The drum geometry and rotation speed were identical between the two models. It is important to emphasize that the

FEM model parameters in Table 4.2 were found from independent, standard material tests rather than being back-fit to the blending data. Since the present work compares the multi-scale model blending performance to results from a DEM simulation, DEM simulations were used to determine the FEM material parameters for consistency. For a more practical case, however, the FEM material parameters would be found from the same characterization tests (i.e., shear cell and uniaxial compression) but performed experimentally. Although spherical particles are used in the current work for simplicity, particle shape and size effects can be considered indirectly via the bulk material properties and diffusion coefficient used in the model. The diffusion coefficient could be measured experimentally or possibly found via DEM simulation [29].

Table 4.2 Parameters used in the FEM simulation.

Parameter	Value
Material density (kg/m^3)	1500
Young's modulus (MPa)	3.65
Poisson's ratio (-)	0.065
Internal friction angle (degree)	23.6
Cohesion (Pa)	0
Dilation angle (degree)	0.1
Wall friction coefficient (-)	0.324

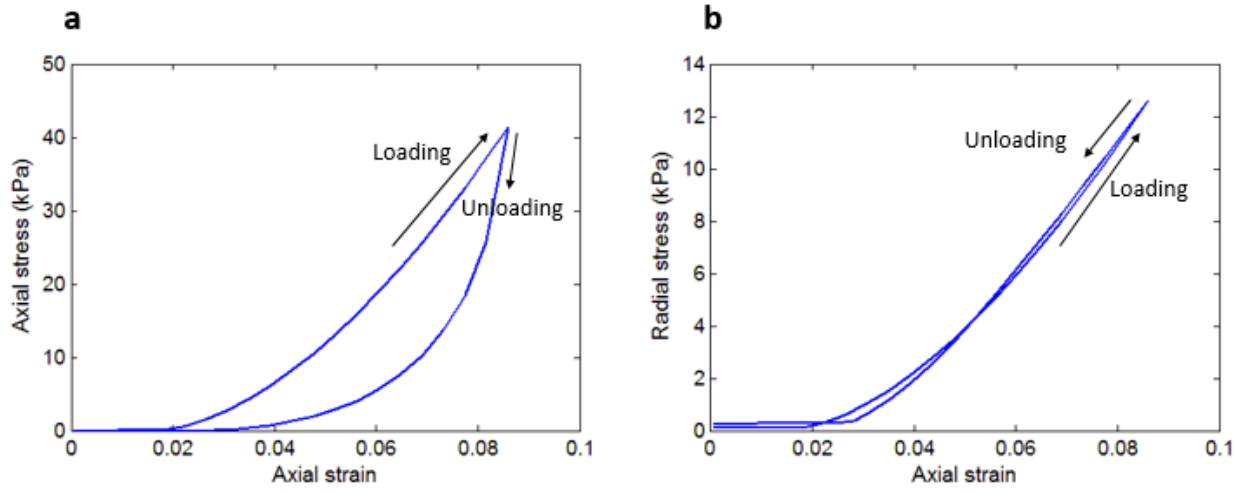

Figure 4.10 The compression and decompression curves from the uniaxial compression DEM simulation used to obtain the bulk elastic modulus and Poisson's ratio.

4.4 Comparison of the DEM and multi-scale model results

The magnitude of the steady state material velocity in the drum, predicted by DEM and FEM simulations, is shown in Figure 4.11. Figure 4.12 plots the velocity along the free surface of the material as well as in the surface-normal direction, predicted by the two different models. These two figures demonstrate that the FEM model compares favorably with the DEM models. The free surface angles predicted by the DEM and FEM simulations are 24.5° and 23.3°, respectively, with a difference of less than 5%. Moreover, the thicknesses of the active layer predicted by the two models differ by less than 5% as well. Zheng and Yu [56]showed that their FEM rotating drum predictions matched experimental measurements well, lending confidence that the FEM model is a good model for predicting velocity fields. Figure 4.11 also illustrates the well-known observation that the flow field in the drum can be divided into two distinct regions: an active region characterized by a thin, downward flowing layer adjacent to the free surface and a passive region below the active region where particles move in solid body rotation [1]. The large velocity gradient in the active region is the source of most of the diffusive mixing in the system (refer to Eq. (4.5)), which is consistent with previous work [76].

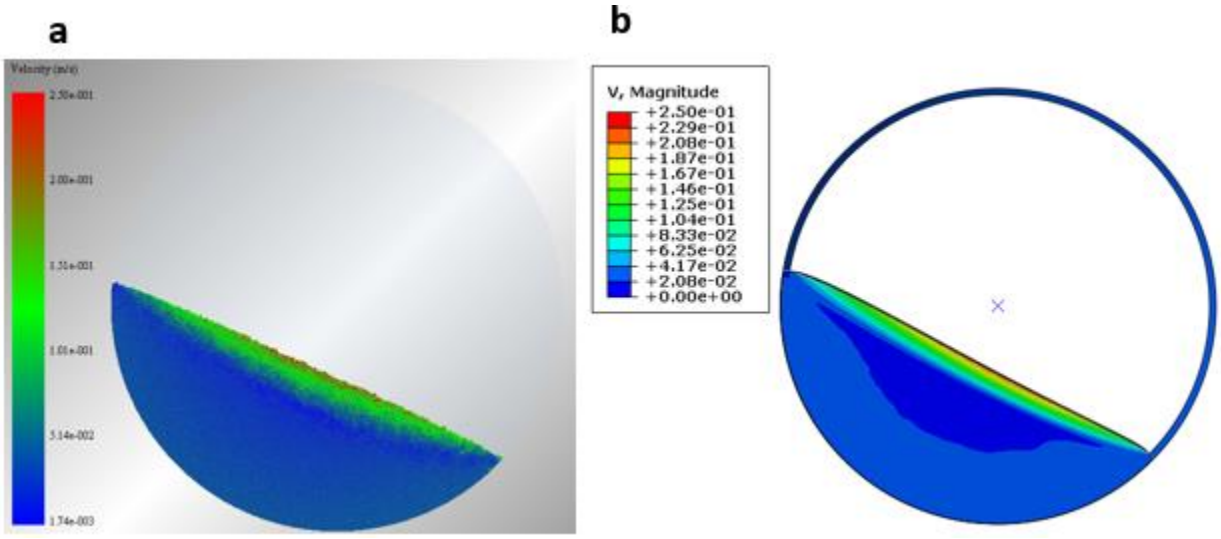

Figure 4.11 Field plots of the material speed in the (a) DEM simulation and (b) FEM simulation. The color scales used in the two figures are identical.

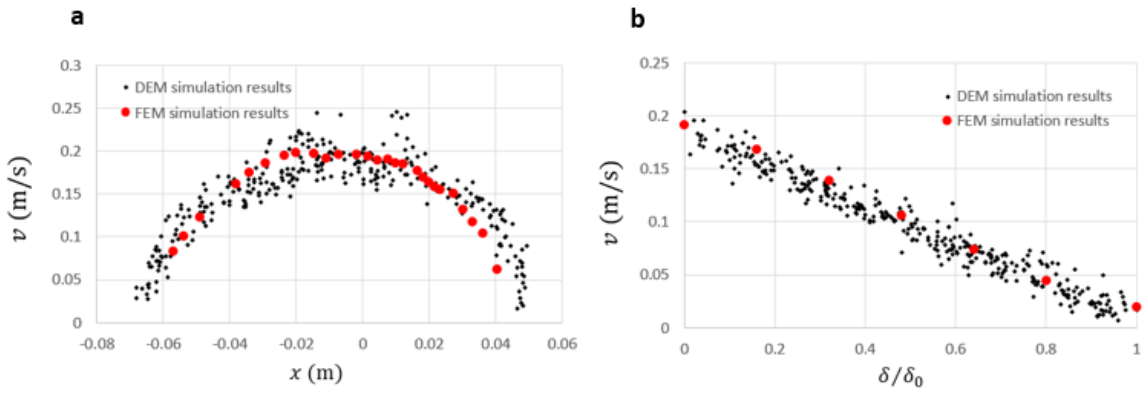

Figure 4.12 The velocity (a) along the free surface of the material, and (b) in the surface-normal direction in Figure 4.11, predicted by DEM and FEM simulations

The initial stages of mixing are shown in Figure 4.13. To enforce consistency between the multi-scale model and DEM model, all the revolutions shown in the current work start from the horizontal position. This figure shows the state of the material in the DEM and FEM (advection only) models at 0.25 revolutions, after which the changes in the velocities in various regions of the drum were observed to be typically less than 3% and steady state material movement began. Clearly the mixing during this short unsteady period was dominated by material advection, which is consistent with the assumption described before that no diffusion happens during the initial development of the bed movement. As mentioned previously, the material concentration field predicted from the FEM model at this point was used as the initial condition for the multi-scale model. Note in Figure 4.13, the edges of the bed free surface in the FEM simulation show a rounder shape than in the DEM simulation due to the method Abaqus uses to display partially filled elements. This effect has no influence on the predictions of interest, namely the free surface angle, flow velocities, and mixing rate.

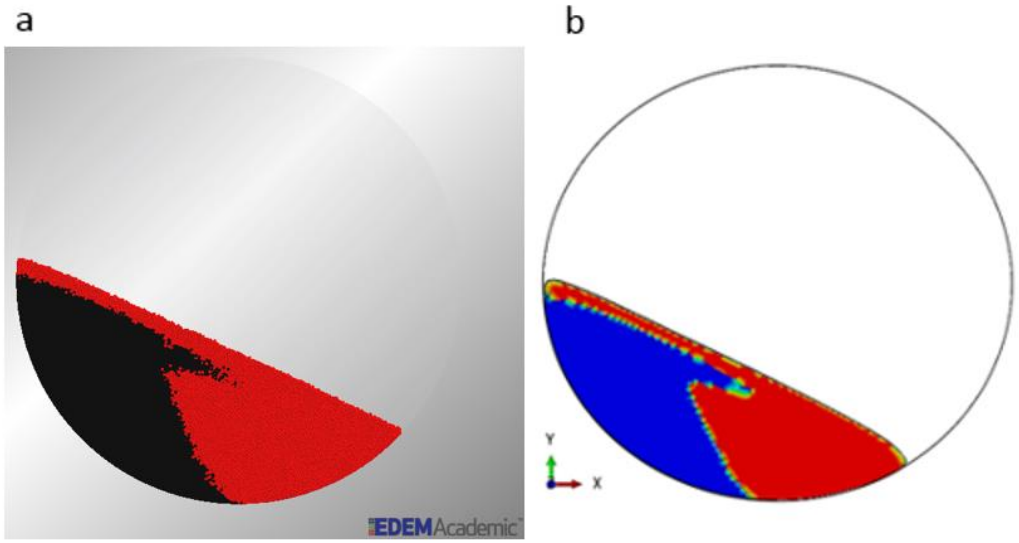

Figure 4.13 The material state in the (a) DEM simulation and (b) FEM simulation (advective material movement only) at 0.25 revolutions, which is when a steady state velocity field is reached.

The state of the material after different numbers of drum revolutions is shown in Figure 4.14 for both the DEM and multi-scale models. The colors in the DEM simulations are the individual red and black particles while the colors in the multi-scale model correspond to the concentration of red particles, with yellow indicating a large concentration of red particles and blue indicating a small concentration. As expected, as time increases the degree of mixing increases, with both advection and diffusion contributing to the mixing process. At least qualitatively, the multi-scale model reproduces the mixing observed in the DEM simulations.

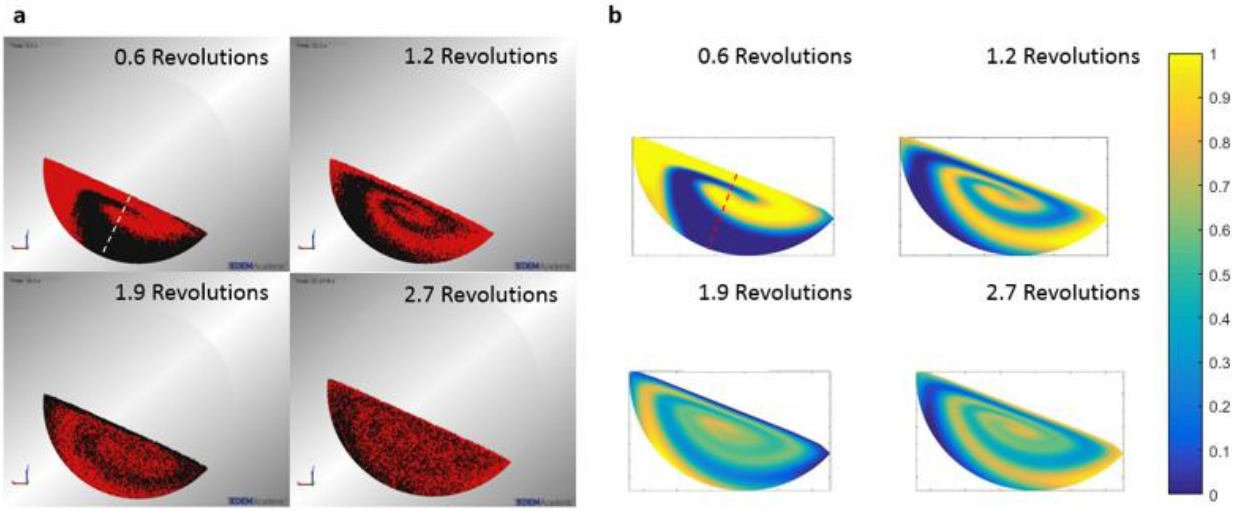

Figure 4.14 Snapshots showing the time evolutions of mixing. (a) DEM simulation and (b) multi-scale model. The vertical color scale in (b) is the red particle concentration.

To provide a more quantitative comparison of the two models, red particle concentration is plotted as a function of the perpendicular distance δ along the center of the bed starting from the free surface (refer to the dashed lines shown in Figure 4.14). The distance is made dimensionless by dividing by the maximum level depth of the drum bed h. Thus, 0 (free surface) $\leq \delta/h \leq 1$ (drum surface). In the DEM simulation, red particle concentration is calculated in cells with a square cross section and a depth spanning the drum width (10 particle diameters). The cells overlap, with each cell center located three particle diameters from its neighbors. The number of red and black particles with centers located within a cell are recorded to calculate the red particle concentration.

Note that because of the finite cell size, often referred to as the "scale of scrutiny", the concentration profile will vary with the cell size. Larger cell sizes provide less spatial resolution while cell sizes approaching the particle size produce less meaningful concentration values due to statistical fluctuations. To examine this cell size influence, three cell sizes of 3d, 5d, and 7d (d is the particle diameter) are used in the concentration calculations. In the multi-scale model, there is no cell size since the material concentration is calculated directly from the advection-diffusion equation at each node point along the path.

Figure 4.15 plots the red particle concentration profiles for the DEM (with cell size of 5d) and multi-scale models for the same number of revolutions shown in Figure 4.14. There is very good

quantitative agreement between the two models, although it does appear that there is a slight offset in the multi-scale model concentration values. As indicated previously, there is a minor difference in the free surface angle between two models, which will lead to an offset in the two results. Both sets of results show large peaks and valleys within the first two drum revolutions. These peaks and valleys diminish considerably by 2.7 revolutions due to increased advective folding of the material along with diffusion. With larger numbers of revolutions, the red particle concentration approaches the expected value of 0.5 along the entire profile. As expected, changing the cell size used in the DEM concentration calculation slightly affects the results. However, the difference is within 10% for a cell size of 5*d* plus or minus 2*d*.

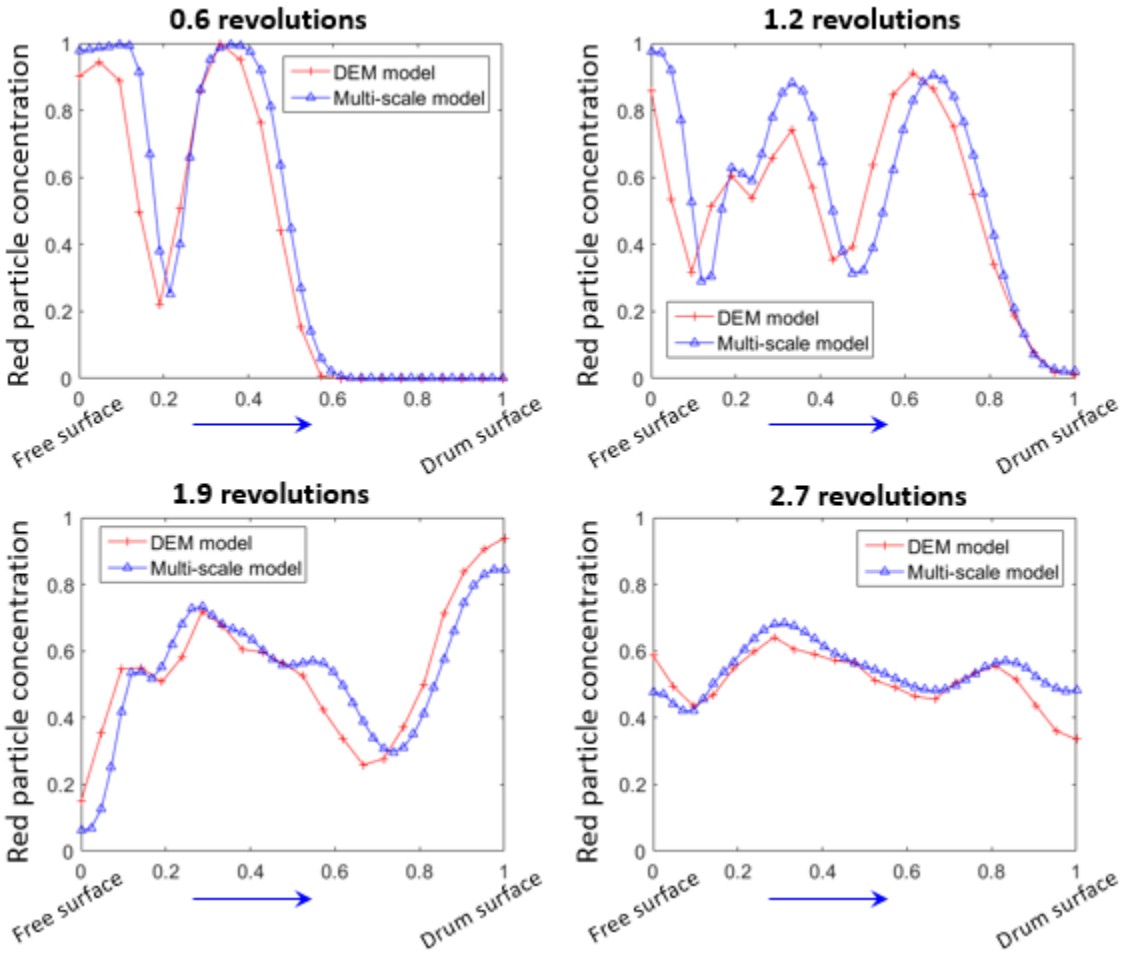

Figure 4.15 Red particle concentration plotted as a function of dimensionless distance from the free surface, δ/h, along the centerline of the drum for both the DEM and multi-scale models. Each plot corresponds to a different number of drum revolutions.

An important point to make is that the multi-scale modeling approach is much faster than the DEM modeling approach. For the parameters listed in Table 4.1, the DEM simulation completed in 5 to 6 days of wall clock time using a 16 processor desktop PC. The same geometry and simulated time using the multi-scale modeling approach (Table 4.2 for the FEM portion) completed in 4 to 5 hours on the same PC with the same number of processors. The FEM computations comprised about 60% of this time with the MATLAB advection-diffusion calculations using the remainder. The multi-scale modeling approach is expected to be even more computationally efficient as the system size increases.

Another common measure used to assess the state of mixedness in a blending operation is the segregation intensity I, which is defined as [77],

$$I_i = \frac{\sigma_i^2}{\sigma_0^2}, \tag{4.22}$$

$$\sigma_i^2 = \frac{1}{N_s - 1}\sum_{n=1}^{N}\left(c_i - c_{i,n}\right)^2, \tag{4.23}$$

$$\sigma_0^2 = c_i\left(1\text{-}c_i\right), \tag{4.24}$$

$$c_i = \frac{1}{N_s}\sum_{n=1}^{N} c_{i,n}\ . \tag{4.25}$$

In these relations, σ_i^2 is the measured variance of component i's concentration (here component i is the red particles), σ_0^2 is the variance of component i's concentration for a fully segregated system, c_i is the measured mean concentration of component i, and N_s is the total number of samples used to calculate the mean and variance. The segregation intensity varies from zero, corresponding to perfect mixing, to one, which is a fully segregated state. The segregation intensity provides less information and is a less stringent test of the multi-scale model's accuracy than the concentration profiles shown in Figure 4.15. Nevertheless, it is calculated here for both models since it is a common metric for assessing the state of blending.

In the multi-scale model, every node at which a concentration is calculated is used in the evaluation of the segregation intensity. For the DEM simulations, a non-overlapping grid of cuboidal cells, illustrated in Figure 4.16(a), is used to calculate red particle concentration. As with the

concentration profile, cell sizes of 3*d*, 5*d*, and 7*d* are used. The segregation intensity values are plotted in Figure 4.16(b) as a function of the number of drum revolutions. Both models display the frequently observed decay in segregation intensity, which is often fit to an exponential function. Significantly, the multi-scale model quantitatively predicts the DEM results well. The DEM scale of scrutiny does play a minor role with larger scales of scrutiny having smaller segregation intensities. This trend is expected from statistics [78].

The asymptotic values for the segregation intensity can be predicted analytically as originally described by Danckwerts [78]. A perfectly mixed state where $I = 0$ is generally not achievable in practice and instead a randomly mixed state is the expected asymptotic state. For a randomly mixed system, the concentration variance is,

$$\sigma_r^2 = \frac{c_i\left(1\text{-}c_i\right)}{N_p}, \tag{4.26}$$

where N_p is the number of particles in the cell used to calculate the concentration. Thus, the segregation intensity for a randomly mixed system is $I_R = \sigma_r^2/\sigma_0^2$. Clearly, as the scale of scrutiny increases, the asymptotic segregation intensity decreases, which is the trend observed in Figure 4.16(b). Interestingly, the multi-scale model predicts an asymptotic segregation intensity of zero, corresponding to a perfectly mixed state. This result stems from the fact that the multi-scale model assumes the material is a continuum and thus the number of particles in Eq. (4.26) is infinite. Hence, although the multi-scale model accurately predicts mixing behavior throughout most of the process, it will always predict a smaller segregation intensity at larger times.

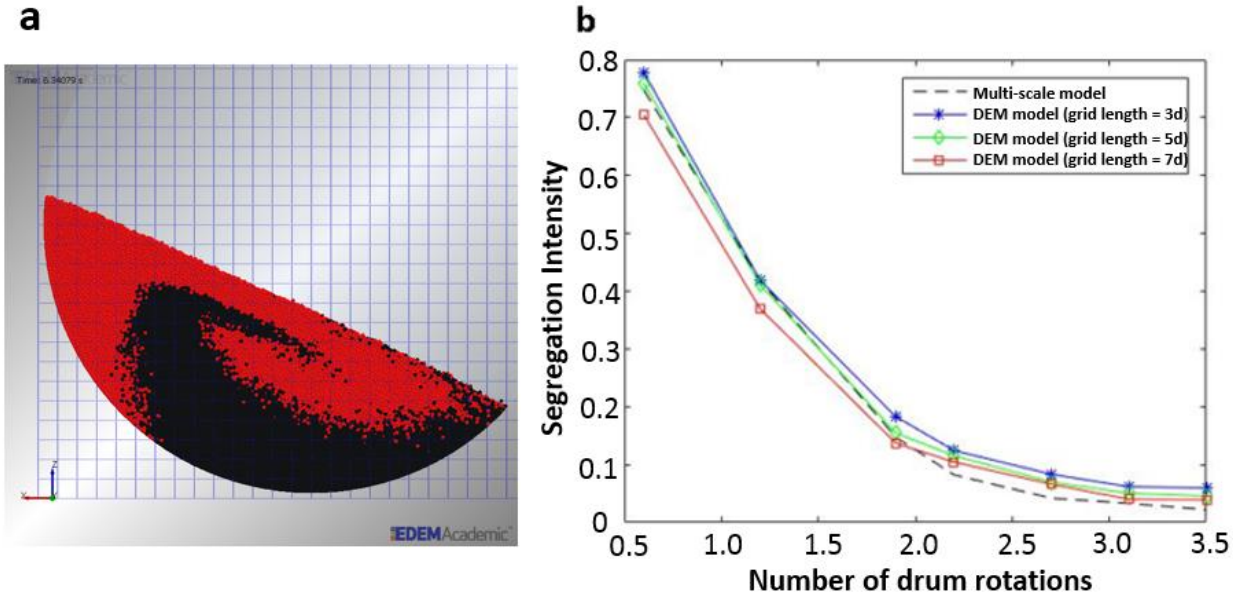

Figure 4.16 (a) The cuboidal cells in the DEM simulation; (b) the segregation intensity as a function of the number of drum revolutions for the DEM model and multi-scale model.

4.5 Parametric study of the multi-scale model

To better understand the effect of and the sensitivity to changes in different parameters of the multi-scale model, a study was performed in which several of the model parameters were varied. A sensitivity analysis of the system was also performed in order to more efficiently perform the simulations.

A mesh dependency study was performed first to ensure convergence of the advection-diffusion solution. Figure 4.17 shows the segregation intensity for different diffusion constants as a function of the number of drum revolutions for different numbers of mesh elements. For $k_1 = 0.04$, which was chosen based on prior studies, the solution was insensitive to the mesh sizes tested and, thus, 300,000 elements were used in the current study to maintain accuracy and computational efficiency (Figure 4.17(a)). Note that for a much smaller diffusion constant of $k_1 = 0.005$, a similar convergence analysis concludes that a mesh size of 600,000 is needed (see Figure 4.17(b)). This result indicates that for convection dominated flows, a refined mesh is required to avoid the artificial diffusion intrinsic to the finite difference method itself.

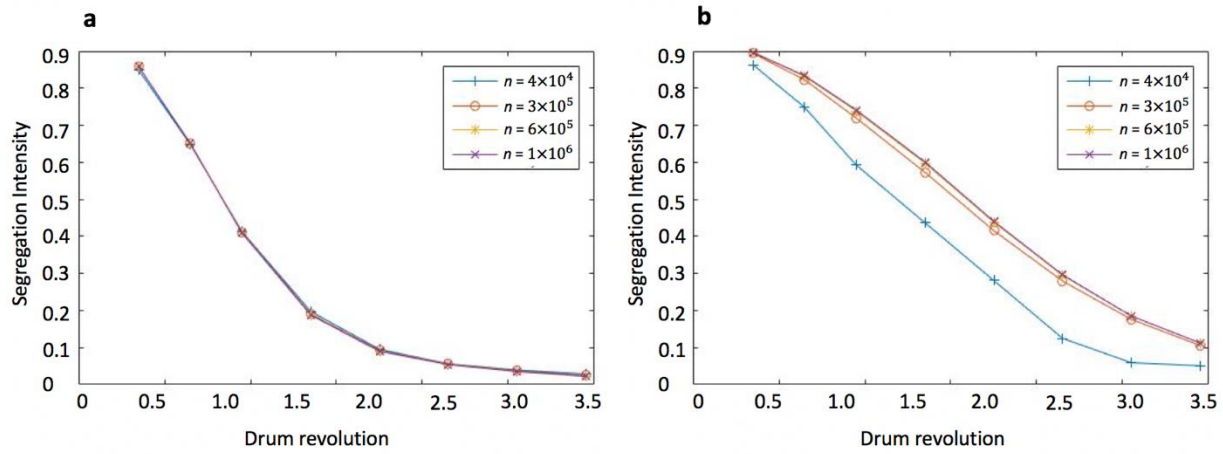

Figure 4.17 The segregation intensity for diffusion constants of (a) $k_1 = 0.04$ and (b) $k_1 = 0.005$.

To more efficiently investigate the influence of other parameters on the degree of mixing in the system (quantified using the segregation intensity), a sensitivity analysis of the system is performed first. Table 4.3 lists the dimensionless parameters resulting from the multi-scale model. For consistency, the Froude number Fr and the filling volume fraction f_v are kept constant throughout the study. Moreover, as mentioned previously, the elastic modulus E and Poisson's ratio ν have little influence on the material flow behavior and, hence, are not studied. Therefore, the internal friction angle f_i, wall friction angle f_w, drum diameter to particle diameter ratio D_{drum}/d, and diffusion constants k_1 and k_2 are included in the parametric study.

Table 4.3 Dimensionless parameters.

Parameter	Dimensionless Quantity
Segregation intensity	I
Number of drum revolutions	$\frac{\omega \cdot t}{2\pi}$
Froude number	$Fr = \frac{\omega^2 D_{\text{drum}}}{g}$
Filling volume fraction	f_v
Ratio of elastic modulus to max hydrostatic pressure	$\frac{E}{\rho_{\text{bulk}} g D_{\text{drum}} f_v}$
Poisson's ratio	ν
Internal friction angle	f_i
Wall friction angle	f_w
Drum diameter to particle diameter ratio	$\frac{D_{\text{drum}}}{d}$
Spanwise diffusion constant	k_1
Streamwise diffusion constant	k_2

The effects of internal friction angle and wall friction angle are shown in Figure 4.18. A larger internal friction angle results in slower mixing, which appears to be due to a reduction in active region surface speeds caused by the increased frictional resistance. However, the mixing process happens so fast in this lab-scale drum that the materials are well-mixed after three revolutions, regardless of the internal friction angle. Figure 4.18(b) indicates that the mixing process is unaffected by the wall friction angle. The reason for this behavior is that, if the wall friction is sufficiently large to lift the powder, the first avalanche always occurs at the same location and the free surface angle remains constant (and equal to the internal friction angle). If the wall friction angle is too small, the powder cannot be lifted and it slips against the rotating wall.

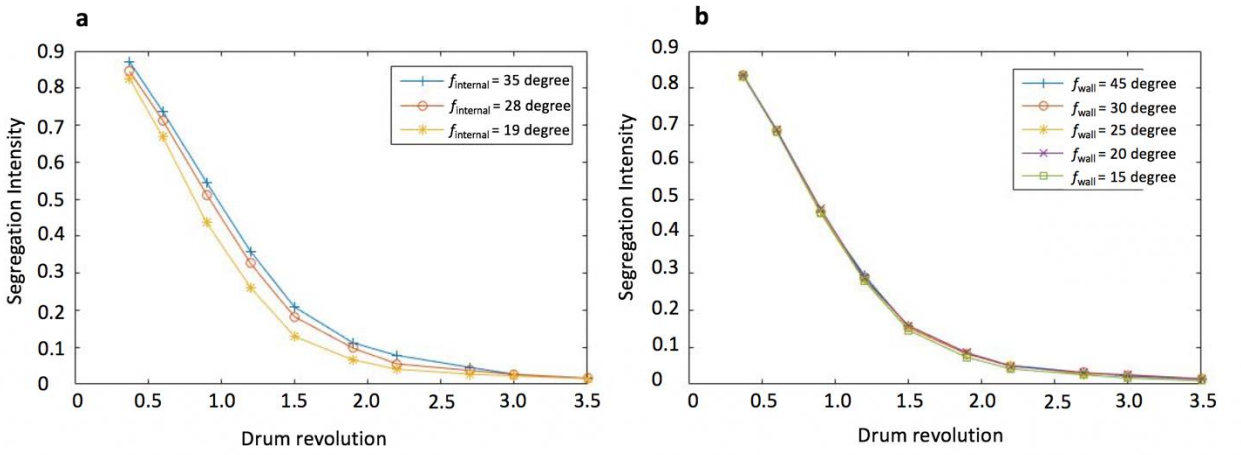

Figure 4.18 The segregation intensity I as a function of the number of drum revolutions for (a) different internal friction angles f_i, and (b) different wall friction angles f_w, as defined in Table 4.3.

The effect of drum-to-particle diameter ratio is shown in Figure 4.19. Although particles are not directly simulated in the multi-scale model, their size does indirectly appear in the calculation of the diffusion coefficient, with smaller particles resulting in smaller diffusion coefficients. The material properties remain unchanged since the material is assumed to remain cohesionless and identical in shape regardless of particle size. A larger drum-to-particle diameter ratio results in slower mixing since a larger drum diameter results in a thicker shear layer and a smaller particle diameter results in a smaller diffusion coefficient. The same trend can be found in work by Kwapinska et al. [8]. These results are useful for anticipating changes when scaling a mixing operation, for example.

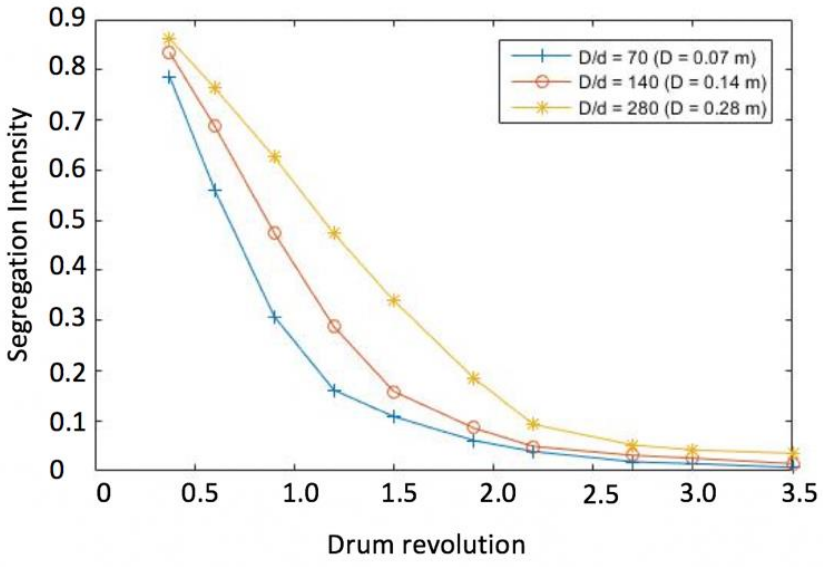

Figure 4.19 The segregation intensity as a function of the number of drum revolution for different drum diameter to particle diameter ratios D_{drum}/d, as defined in Table 4.3.

The effects of the spanwise and streamwise diffusion constants k_1 and k_2 are shown in Figure 4.20. According to Eq. (4.6), a larger diffusion constant k_1 or k_2 results in a larger diffusion coefficient and, thus, more rapid mixing. The diffusion constant k_1 is more dominant than k_2, even when k_2 is larger than k_1. In a rotating drum, as shown in Figure 4.11, the spanwise shear rate within the active region is much larger than the streamwise shear rate. Therefore, even though the streamwise diffusion constant k_2 is larger than the spanwise diffusion constant k_1, the mixing occurs mainly in the spanwise direction. However, this is not necessarily true for other geometries and hence the streamwise diffusion constant k_2 should be included in the diffusion coefficient expression for completeness.

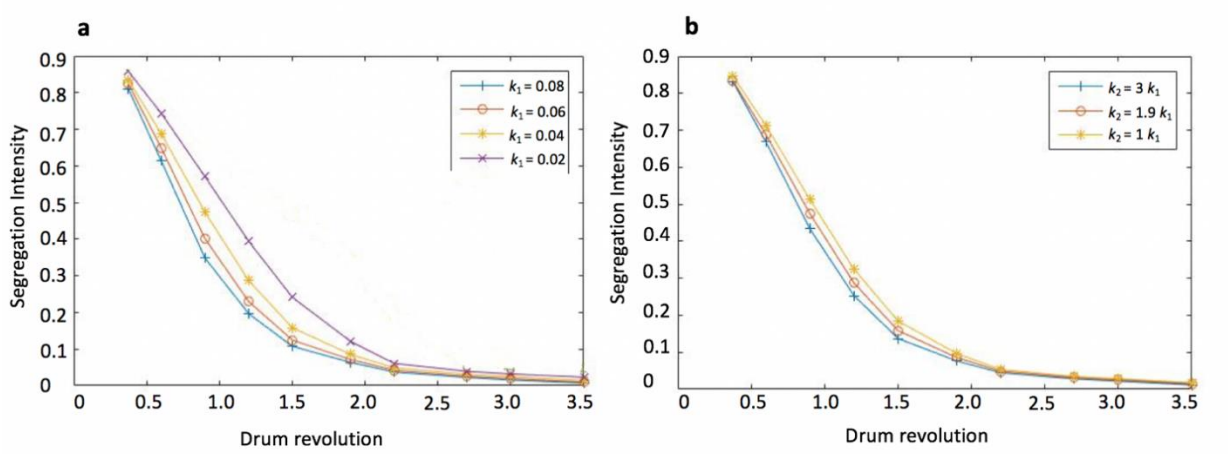

Figure 4.20 The segregation intensity as a function of the number of drum revolutions for (a) different spanwise diffusion constants k_1, and (b) different streamwise diffusion constants k_2, as defined in Table 4.3.

4.6 Summary

In the current chapter, a new multi-scale approach to modeling particulate blending processes is presented. This multi-scale modeling approach combines finite element method simulations to obtain macroscopic velocity fields with calculations from the advection-diffusion equation with computationally and experimentally obtained expressions for particle diffusion at a local scale. The potential of this approach is demonstrated with the study of a rotating drum blender, i.e., with a "benchmark" system. Predictions of concentration profiles and segregation intensity from the multi-scale model compare well quantitatively to DEM results, although the multi-scale model does predict smaller segregation intensities than those found from the DEM model at large times. This inaccuracy is due to the fact that the multi-scale model assumes continuum material behavior and, thus, the asymptotic mixing state corresponds to a perfectly mixed system as opposed to the asymptotic randomly mixed state predicted for the finite sized particles used in DEM simulations. Also, a parametric study was performed to better understand the effect of and the sensitivity to changes in different parameters of the multi-scale model.

CHAPTER 5. THREE-DIMENSIONAL MULTI-SCALE MIXING MODEL

* The content of this chapter is an extended version of a paper published in the Powder Technology Journal (doi:10.1016/j.powtec.2018.09.033).

The current chapter extends the work in Chapter 4 to investigate mixing in a more industrially-relevant Tote blender. Several key implementation details are also different. First, the model utilizes transient velocity field information from the FEM simulations instead of a steady velocity field. Second, the governing equations are extended to three dimensions instead of two dimensions. Together, these two modifications greatly increase the flexibility of the model. In addition, rotating drum experiments are used to calibrate the diffusion coefficient used in the multi-scale model and the model predictions are compared against published experimental results. Section 5.1 introduces the FEM modeling approach and implementation for the current work. Section 5.2 describes the advection-diffusion equation used in the multi-scale model and the numerical method used to solve it. Section 5.3 describes the material calibration methods and experiments. In Section 5.4, comparisons are made between published experimental results and the multi-scale model predictions. And Section 5.5 studies the effects of the initial loading condition and fill method.

5.1 Finite element method model

A three-dimensional, coupled Eulerian-Lagrangian, FEM model is used in the present work to provide predictions of the advective flow field in a Tote blender. Previous works [56,57,73,74,79] have shown that FEM models can accurately simulate granular material behavior well, including advective flow fields [56,57], and that results are mesh-independent after a critical mesh refinement. For example, in the previous work [56,57], compared to the results using 160,000 elements, the results change by less than 1% when using 40,000 elements or 10,000 elements. Details of the model implementation can be found in previous work [80] and Chapter 4. The following sub-sections describe the model geometry, boundary conditions, and initial conditions.

5.1.1 Model geometry and boundary conditions

The commercial FEM package Abaqus/Explicit v6.14 is used to perform the bulk flow simulations. The geometry of the simulated Tote blender is based on the experiments by Sudah et al. [81]. Those experiments were carried out in a 14-L GEI Gallay Tote blender. Details of the geometry and dimensions of the blender are presented in their work [81]. For convenience, the dimensions are also shown in Figure 5.1.

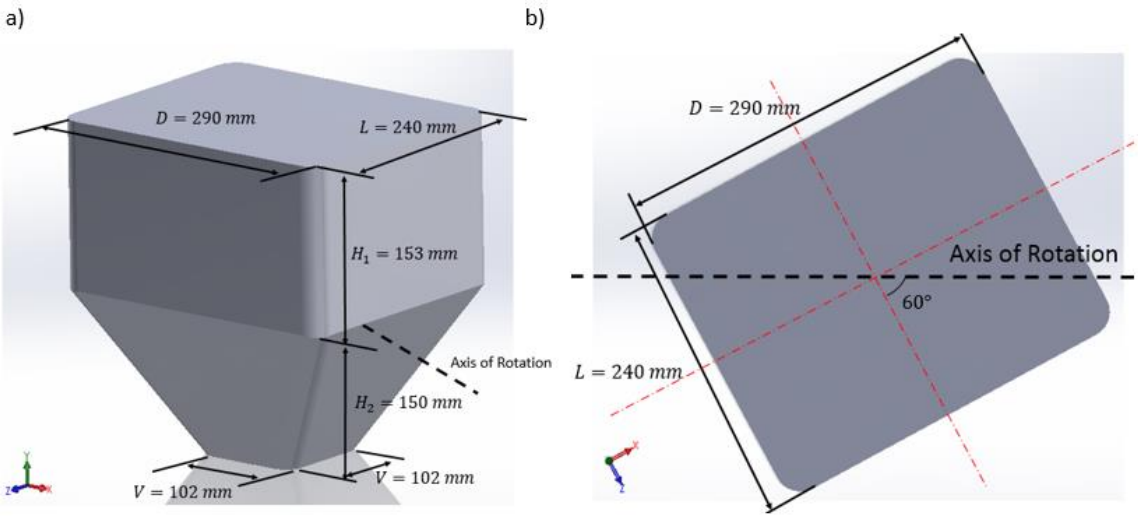

Figure 5.1 Dimensions of the GEA Gallay Tote blender used in the FEM simulation.

A Mohr-Coulomb elastoplastic model is used in the current work to describe the stress-strain behavior of the particulate material. Chapter 4 has shown that this constitutive model can accurately describe dense granular flow fields. Note that: a) The current constitutive model is shear rate-independent. Previous works [56,80] have shown that a shear rate-independent constitutive model is sufficiently accurate for the Tote blender investigated in the current work. However, other models should be considered if shear rate effects become important. b) The current constitutive model cannot predict the formation of shear bands without considering shear localization. For situations where shear bands are important, other constitutive models, such as an extended Mohr-Coulomb model, could be used to get a more accurate prediction [82]. c) The current model does not take into account changes in material porosity nor material hardening or softening since the current system does not involve large changes in porosity. For systems in which the solid fraction

changes significantly, such as during compaction, a modified Drucker-Prager Cap (DPC) model could be used to account for material hardening and softening [74,75].

The material properties needed in the model are bulk density, Young's modulus, Poisson's ratio, and material internal friction angle. These parameters can be found from independent, standard material tests. For example, the bulk density, Young's modulus, and Poisson's ratio can be calibrated from a uniaxial compression test and the material internal friction angle can be measured from a standard shear cell test. The methodology for obtaining those material properties was described in detail in Chapter 4.

Linear shape functions for 8-node hexahedrons were used in the current work and the elements use a reduced integration scheme with one integration point and hourglass effects are controlled. These techniques were used to prevent locking [83]. Boundary conditions applied in the model include the material-wall friction angle, the rotational speed along the axis of rotation, and the gravitational acceleration (g = 9.8 m/s^2 directed in the negative y direction in Figure 5.1).

5.1.2 Initial conditions

The coupled Eulerian-Lagrangian approach implemented in Abaqus is adopted in the current model. Details of this approach were described in Chapter 4. As shown in Figure 5.2, the Eulerian mesh covers the entire material domain and ensures that no material leaks outside of the mesh. The Eulerian Volume Fraction (EVF) value, as introduced in Chapter 4, is used to determine the volume of material within each element. A value of EVF = 0 indicates that no material is present in the element while EVF = 1 indicates that the element is completely filled with material.

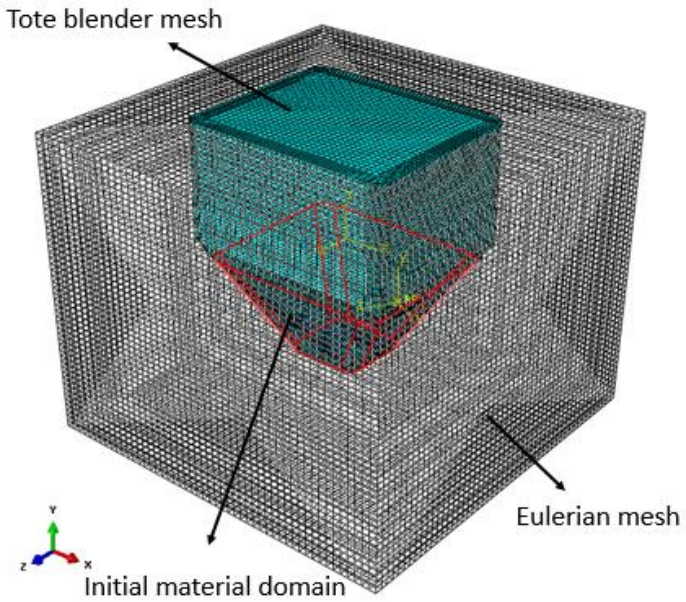

Figure 5.2 A schematic of the FEM model domain. The Eulerian mesh is shown in grey, the Tote blender mesh is shown in blue, and the outlines of the initial material domain are shown in red.

The initial bed state is generated by filling a fraction of the elements with material. Details of the process can be found in Chapter 4 as well. For monodisperse mixing, material loadings were achieved by assigning user-defined field variables at each material point to represent the initial material concentration. Details of this field variable approach can be found in the Abaqus documentation [62]. An example of left-right initial loading is shown in Figure 5.3. The color represents a field variable value from 0 (blue) to 1 (red). For monodisperse mixing with materials A and B, the field variable represents the material concentration of A. A field variable value of one indicates that the element is completely filled with material A, while a value of zero indicates that the element is completely filled with material B.

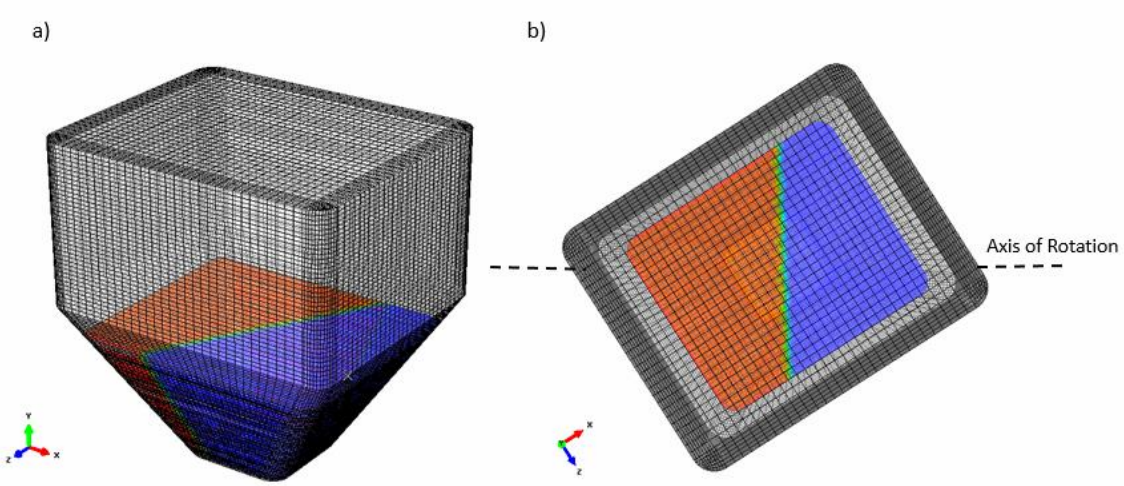

Figure 5.3 Initial material concentration for a simulation with left-right loading. The color represents field variable value from zero (blue) to one (red). The materials in this simulation have homogeneous properties, except for color.

The simulation process consists of two steps. First, the material is allowed to settle as the gravitational acceleration is slowly increased from zero to its final value. The blender remains stationary during this step. This procedure is used to eliminate the transient oscillations of material as it settles and results in a stable bed compressed under its own weight. Next, the blender is allowed to rotate immediately at the rotation speed and the simulation is considered started.

5.2 The multi-scale mixing model

The current multi-scale model is extended from the two-dimensional model introduced in Chapter 4. Details of the model description and development can be found there. Since all of the material is identical in the current chapter, except for color, a one-way coupled method is used and, thus, material properties do not change with concentration. The following sub-sections summarize the main aspects of the model and highlight its extension to transient, three-dimensional problems.

5.2.1 Advection-diffusion equation

The same advection-diffusion equation used in Chapter 4 is used in the current chapter to model the spatiotemporal evolution of the concentration of a particular material species, c. The governing equation is derived as,

$$\frac{\partial c}{\partial t} = \nabla \cdot \left(\boldsymbol{D} \nabla c \right) - \nabla \cdot \left(\boldsymbol{v} c \right), \tag{5.1}$$

where c is the local concentration of a particular species of material, $\boldsymbol{D}$ is the diffusion coefficient tensor for that species, and $\boldsymbol{v}$ is the local advective velocity vector. Using the local mass conservation equation and assuming an incompressible material, i.e.,

$$\nabla \cdot \boldsymbol{v} = 0, \tag{5.2}$$

the governing equation can be written in index notation form as,

$$\frac{\partial c}{\partial t} = \frac{\partial}{\partial x_i}\left(D_{ij} \frac{\partial c}{\partial x_j} \right) - v_i \frac{\partial c}{\partial x_i}. \tag{5.3}$$

The self-diffusion coefficient $\boldsymbol{D}$ is a tensor quantity with components D_{ij}, and with off-diagonal components D_{ij} ($i \neq j$) an order of magnitude smaller than the diagonal components D_{ij} ($i = j$) as mentioned in Chapter 4. By neglecting off-diagonal components of the self-diffusion coefficient tensor, the index notation form of Eq. (5.3) in three-dimensional form is,

$$\begin{aligned} \frac{\partial c}{\partial t} = & \left(\frac{\partial D_{xx}}{\partial x} - v_x \right) \frac{\partial c}{\partial x} + D_{xx} \frac{\partial^2 c}{\partial x^2} + \left(\frac{\partial D_{yy}}{\partial y} - v_y \right) \frac{\partial c}{\partial y} + D_{yy} \frac{\partial^2 c}{\partial y^2} \\ & + \left(\frac{\partial D_{zz}}{\partial z} - v_z \right) \frac{\partial c}{\partial z} + D_{zz} \frac{\partial^2 c}{\partial z^2} \end{aligned}, \tag{5.4}$$

The self-diffusion coefficient $\boldsymbol{D}$ is also proportional to the local shear rate $\dot{\gamma}$ and the local mean particle diameter $\bar{d}$. The particle diffusivity is approximately 1.9 times larger along the mean flow direction than it is in the perpendicular direction, according to work by Utter et al. [66]. Note that this relationship was derived for dense, granular shear flows in a 2D Couette apparatus by using round disks and it could be dependent on the material type. However, results in Chapter 4 showed that including the particle diffusivity in the mean flow direction was not significant for a tumbling system. Hence, $k_2 = 1.9k_1$ is still used in the current work. The shear rate-dependent diffusion coefficient $\boldsymbol{D}$ can be written as,

$$\begin{aligned} D_{xx} &= k_1 \dot{\gamma}_x \bar{d}^2 + k_2 \left(\dot{\gamma}_y + \dot{\gamma}_z \right) \bar{d}^2 \\ D_{yy} &= k_1 \dot{\gamma}_y \bar{d}^2 + k_2 \left(\dot{\gamma}_x + \dot{\gamma}_z \right) \bar{d}^2 \\ D_{zz} &= k_1 \dot{\gamma}_z \bar{d}^2 + k_2 \left(\dot{\gamma}_x + \dot{\gamma}_y \right) \bar{d}^2 \end{aligned}, \tag{5.5}$$

where $\dot{\gamma}_x = \left(\left|\partial v_y/\partial x\right| + \left|\partial v_z/\partial x\right|\right)$, $\dot{\gamma}_y = \left(\left|\partial v_x/\partial y\right| + \left|\partial v_z/\partial y\right|\right)$, and $\dot{\gamma}_z = \left(\left|\partial v_x/\partial z\right| + \left|\partial v_y/\partial z\right|\right)$. The constant k_1 can be found from experiments or small-scale DEM simulations, with $k_2 = 1.9k_1$.

5.2.2 Numerical method

The same as Chapter 4, A finite difference method using a central explicit scheme is used to solve Eq. (5.4) due to its simplicity and computational efficiency. A second-order Tylor Lax-Wendroff scheme is used to generate the finite difference expression of the governing equation,

$$c_{ijk}^{n+1} = c_{ijk}^{n} - \left[\nu_x \Delta_{x0} c_{ijk}^{n} - \left(\frac{1}{2}\nu_x^2 + \mu_x\right)\delta_x^2 c_{ijk}^{n}\right] - \left[\nu_y \Delta_{y0} c_{ijk}^{n} - \left(\frac{1}{2}\nu_y^2 + \mu_y\right)\delta_y^2 c_{ijk}^{n}\right] - \left[\nu_z \Delta_{z0} c_{ijk}^{n} - \left(\frac{1}{2}\nu_z^2 + \mu_z\right)\delta_z^2 c_{ijk}^{n}\right] + \nu_x\nu_y \Delta_{x0}\Delta_{y0} c_{ijk}^{n} + \nu_y\nu_z \Delta_{y0}\Delta_{z0} c_{ijk}^{n} + \nu_z\nu_x \Delta_{z0}\Delta_{x0} c_{ijk}^{n}, \tag{5.6}$$

where,

$$\nu_x = \frac{\left[v_x + \Delta_{x0}\left(D_{xx}\right)_{ijk}\right]\Delta t}{\Delta x}, \tag{5.7}$$

$$\nu_y = \frac{\left[v_y + \Delta_{y0}\left(D_{yy}\right)_{ijk}\right]\Delta t}{\Delta y}, \tag{5.8}$$

$$\nu_z = \frac{\left[v_z + \Delta_{z0}\left(D_{zz}\right)_{ijk}\right]\Delta t}{\Delta z}, \tag{5.9}$$

$$\mu_x = \left(D_{xx}\right)_{ijk}\frac{\Delta t}{\Delta x^2}, \tag{5.10}$$

$$\mu_y = \left(D_{yy}\right)_{ijk}\frac{\Delta t}{\Delta y^2}, \tag{5.11}$$

$$\mu_z = \left(D_{zz}\right)_{ijk}\frac{\Delta t}{\Delta z^2}, \tag{5.12}$$

$$\Delta_{x0} c_{ijk}^{n} = \frac{c_{i,j+1,k}^{n} - c_{i,j-1,k}^{n}}{2}, \tag{5.13}$$

$$\Delta_{y0} c_{ijk}^{n} = \frac{c_{i+1,j,k}^{n} - c_{i-1,j,k}^{n}}{2}, \tag{5.14}$$

$$\Delta_{z0} c_{ijk}^{n} = \frac{c_{i,j,k+1}^{n} - c_{i,j,k-1}^{n}}{2}, \tag{5.15}$$

$$\delta_x^2 c_{ijk}^n = c_{i,j+1,k}^n - 2c_{ijk}^n + c_{i,j-1,k}^n , \tag{5.16}$$

$$\delta_y^2 c_{ijk}^n = c_{i+1,j,k}^n - 2c_{ijk}^n + c_{i-1,j,k}^n , \tag{5.17}$$

$$\delta_z^2 c_{ijk}^n = c_{i,j,k+1}^n - 2c_{ijk}^n + c_{i,j,k-1}^n , \tag{5.18}$$

$$\Delta_{x0}\Delta_{y0} c_{ijk}^n = \frac{\left(c_{i+1,j+1,k}^n - c_{i-1,j+1,k}^n - c_{i+1,j-1,k}^n + c_{i-1,j-1,k}^n\right)}{4}, \tag{5.19}$$

$$\Delta_{y0}\Delta_{z0} c_{ijk}^n = \frac{\left(c_{i+1,j,k+1}^n - c_{i-1,j,k+1}^n - c_{i+1,j,k-1}^n + c_{i-1,j,k-1}^n\right)}{4}, \tag{5.20}$$

$$\Delta_{z0}\Delta_{x0} c_{ijk}^n = \frac{\left(c_{i,j+1,k+1}^n - c_{i,j-1,k+1}^n - c_{i,j+1,k-1}^n + c_{i,j-1,k-1}^n\right)}{4}, \tag{5.21}$$

$$\Delta_{x0}\left(D_{xx}\right)_{ijk} = \frac{\left(D_{xx}\right)_{i,j+1,k} - \left(D_{xx}\right)_{i,j-1,k}}{2}, \tag{5.22}$$

$$\Delta_{y0}\left(D_{yy}\right)_{ijk} = \frac{\left(D_{yy}\right)_{i+1,j,k} - \left(D_{yy}\right)_{i-1,j,k}}{2}, \text{ and} \tag{5.23}$$

$$\Delta_{z0}\left(D_{zz}\right)_{ijk} = \frac{\left(D_{zz}\right)_{i,j,k+1} - \left(D_{zz}\right)_{i,j,k-1}}{2}. \tag{5.24}$$

This finite difference formula is illustrated using the computational molecule shown in Figure 5.4. Details of the Taylor series expansion and stability of the numerical computations can be found in Chapter 4.

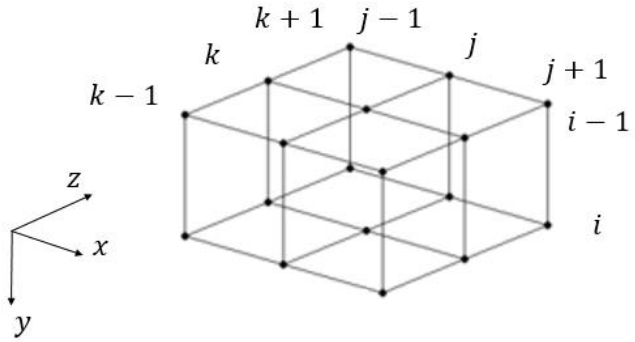

Figure 5.4 Computational molecule for the second-order, three-dimensional Taylor Lax-Wendroff scheme.

It should be emphasized that transient velocity fields are included in the solution to the advection-diffusion equation, Eq. (5.4), by extending the work in Chapter 4. Therefore, a C++ post-processing script was developed to process the FEM output files (.obd files [62]) and handle the large amount of data from these simulations.

As mentioned in Section 5.1, the initial particle concentrations used in the model are determined by the loading conditions, and the user-defined field variable used in the FEM simulation is set accordingly, as in Figure 5.3. Since transient velocity fields are used in the current model, the boundaries of the material domain change throughout the entire computation. These boundaries are computed within the FEM simulation from the EVF values and, similarly, are determined by the advection-diffusion solver, after reading EVF values from the FEM output file at each time step. Specifically, the advection-diffusion boundary conditions at the free surface are enforced by setting the material concentration of the boundary node equal to the value of the node that is one grid point inward in the direction normal to the surface. This approach is similar to the polynomial fitting approach often used in computational fluid dynamics (CFD) [71].

Next, a MATLAB program is used to iterate the finite difference form of the advection-diffusion equation given in Eq. (5.6). After generating initial particle concentrations using the extracted field variable values, the material concentration evolution is iterated using the transient velocity field obtained from the FEM simulation for each time step. A threshold is set to ensure the material concentration value remains between zero and one, and a small time step is carefully chosen to ensure the stability of the explicit scheme. Details of the iteration algorithm were presented in Chapter 4.

To achieve a converged result, the number of elements used in the advection-diffusion MATLAB program should be much larger than the number of elements in the FEM simulation. Hence, a linear interpolation algorithm is introduced in the MATLAB program to generate enough elements and ensure convergence. The MATLAB numerical algorithms are parallelized to divide the computational domain onto different cores. By using the full processing power of an eight-core desktop with the Intel Xeon CPU E5-2680 v3 processor, the iteration runs approximately 5-8 times faster than on a single core.

5.3 Calibration of material properties

5.3.1 Material properties for the FEM simulation

The published experimental work for monodisperse particle mixing by Sudah et al. [81] was used to validate the multi-scale model predictions. Those experiments utilized a 14-L GEI Gallay Tote blender containing 12-mm diameter glass beads of two different colors.

As mentioned in Chapter 4, the material density ρ, elastic modulus E, and Poisson's ratio ν are known to have little influence on the material flow behavior. Moreover, the mixing process was shown to be unaffected by the wall friction angle within a rotating blender since the first avalanche always occurs at the same location and the free surface angle remains constant. Hence, the material density, elastic modulus, Poisson's ratio, and wall friction angle used in the current FEM simulation are all based on values from Chapter 4 for hard spheres. Note that the Poisson's ratio is very small because it is for a loose powder bed (relative density around 0.3). It is expected to be small since a loose powder bed is very compressible. Previous works [73–75] have shown that the Poisson's ratio is typically small at relative densities near the poured relative density for a variety of different materials, which is consistent with the value measured in the current work. The wall friction angle is assumed constant in the current work since the wall is assumed smooth and nominally uniform. In addition, the Mohr-Coulomb dilation angle of the material was set to 0.1°, which is the minimum value allowed in Abaqus due to mathematical limitations of the model, since the dilation of cohesionless granular materials is usually small.

The internal friction angle has been shown in Chapter 4 to influence the mixing rate and, hence, must be calibrated. Previous work has shown that the internal friction angle is not sensitive to particle size or consolidation stress for the same material [84–86]. Hence, 1-mm diameter glass beads, as opposed to the 12 mm beads used in the Sudah et al. experiments [81], were used in the current work to calibrate the internal friction angle. A Schulze Ring Shear Tester (Model RST-XS) was used to make these measurements, obtaining values similar to those reported in the literature [87,88]. Note that the cohesion was measured from the same ring shear test. Normally one would consider 1 mm glass spheres to be cohesionless, but rather than set the cohesion to zero, the measured value was used instead. A summary of all of the material parameters used in the FEM

simulation is given in Table 5.1. It is worth noting that these parameters are found from independent, standard material tests, rather than being back-fit to match experimental data with the multi-scale blending simulation results. Also, note that particle shape and size effects can be considered indirectly via the bulk material properties and diffusion coefficient used in the model.

Table 5.1 Parameters used in the FEM simulation.

Parameter	Value
Material density (kg/m^3)	1500
Young's modulus (MPa)	3.65
Poisson's ratio (-)	0.065
Internal friction angle (degree)	27.1
Cohesion (Pa)	87
Dilation angle (degree)	0.1
Wall friction coefficient (-)	0.324

5.3.2 Experimental calibration of the diffusion constant

One significant parameter needed in the multi-scale model is the spanwise diffusion constant k_1. To calibrate k_1 for glass beads, a lab-scale rotating drum experiment was performed. A photograph of the experiment setup is shown in Figure 5.5. An acrylic circular drum of diameter D_{drum} = 150 mm and width W_{drum} = 50 mm was used to contain the material, and two shafts were used to stabilize and rotate the drum. The driving torque was provided by a gear motor that rotated one of the shafts. Rubber bands covered the shafts to prevent slipping. Values for the experiment parameters are listed in Table 5.2.

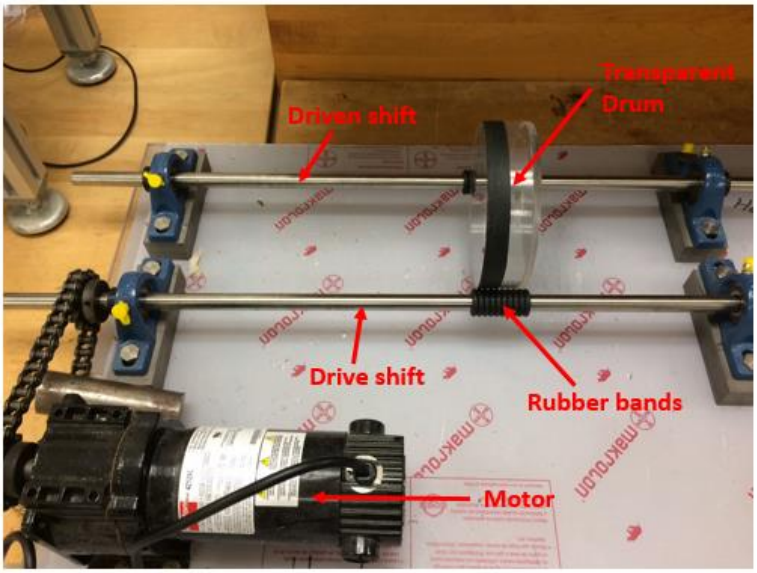

Figure 5.5 The rotating drum experiment setup.

Table 5.2 The rotating drum experiment parameters.

Parameter	Value
Inner drum diameter (mm)	150
Inner drum width (mm)	50
Glass sphere diameter (mm)	1
Filling level (% of max level depth)	32
Drum rotation speed (rpm)	3.26

As shown in Eq. (5.5), the influence of particle diameter on the diffusion coefficient has been included explicitly and thus diffusion constants k_1 and k_2 should be independent of particle diameters. Hence, the drum was filled side by side with 1 mm red and blue glass spheres. To facilitate filling of the drum, the front side of the drum was made removable and a separate barrier was used to help fill each side of the drum with equal volumes of red and blue glass beads. Friction tape was used to seal the drum and to allow the container to rotate smoothly. To analyze the degree of mixing, a high-speed camera was used to film the front of the drum. Once the drum was filled, the drive shift started to rotate and the mixing process was recorded. Several snapshots of the

system at different times are shown in Figure 5.6. Qualitatively, the mixing dynamics in the experiment followed the same trend as the simulations reported in Chapter 4.

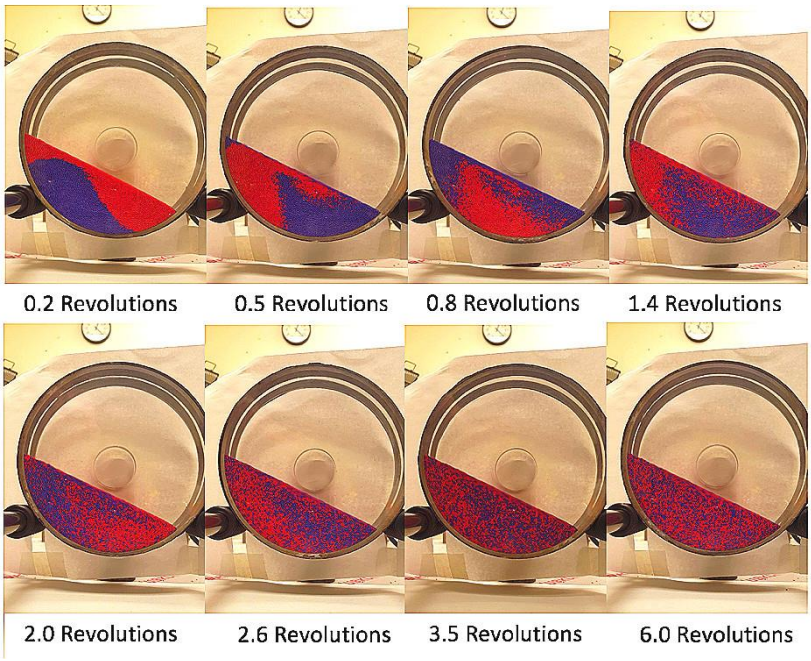

Figure 5.6 Snapshots showing the state of particle mixing for different numbers of drum revolutions in the rotating drum experiments.

To compute the segregation intensity as a function of the number of drum revolutions, a MATLAB code was developed to analyze the video images and derive the spatial distribution of material concentrations. Details of the image processing algorithm are included in the Appendix.

The experimental results were compared with predictions from the 2-D multi-scale model developed in Chapter 4. As shown in Chapter 4, a mesh dependency study was performed first to ensure convergence of the advection-diffusion solution and avoid the artificial diffusion intrinsic to the finite difference method itself. To justify a comparison, the system geometry and operating conditions, such as the drum diameter, drum width, particle diameter, filling level, and rotation speed, were consistent between the experiment and the multi-scale model. The material parameters used in the FEM simulation are shown in Table 5.1 for glass beads.

The segregation intensity I defined in Chapter 4 was computed to compare the experiment results with the 2-D multi-scale model predictions and calibrate the spanwise diffusion constant k_1. Note that the scale of scrutiny does affect the calculation, with larger scales of scrutiny having smaller segregation intensities. Hence, the same grid size used to analyze the experiment results, as described in Appendix, was used in the 2-D multi-scale model. Computationally, the concentration values of all the nodes within one grid cell were averaged to compute the material concentration for the cell. A cell size of five particle diameters was used.

Due to the fact that a continuum is assumed in the FEM simulations, the multi-scale model would predict an asymptotic segregation intensity of nearly zero, corresponding to a perfectly mixed state. However, a perfectly mixed state is generally not achievably in practice and instead a randomly mixed state is the expected asymptotic state. For a randomly mixed system, the segregation intensity is derived as,

$$I_R \approx \frac{\sigma_r^{\,2}}{\sigma_0^{\,2}} = \frac{1}{N_p}, \tag{5.25}$$

where N_p is the number of particles in the cell used to calculate the concentration. The segregation intensity for a randomly mixed system in the current work is $I = 0.04$, which is shown in Figure 5.7 as the dashed line. To save computation time, the simulation was stopped once the segregation intensity reached the randomly mixed state.

Segregation intensity plotted as a function of the number of drum revolutions is plotted in Figure 5.7 for different assumed values of the spanwise diffusion constant k_1. Figure 5.8 shows the sum of the absolute differences between the segregation intensities measured from experiments and computed from the 2-D multi-scale model for different k_1 values. It can be seen that the segregation intensities computed from the 2-D multi-scale model match best with the values measured from experiments when $k_1 = 0.01$. Hence, a calibrated spanwise diffusion constant k_1 for glass beads equal to 0.01 is adopted. Note that the asymptotic value of the experimental results is slightly larger than the value for the randomly mixed state. This difference is because the image correction algorithm described in Appendix introduces some error into the system and the perfectly random mixed state cannot be reached.

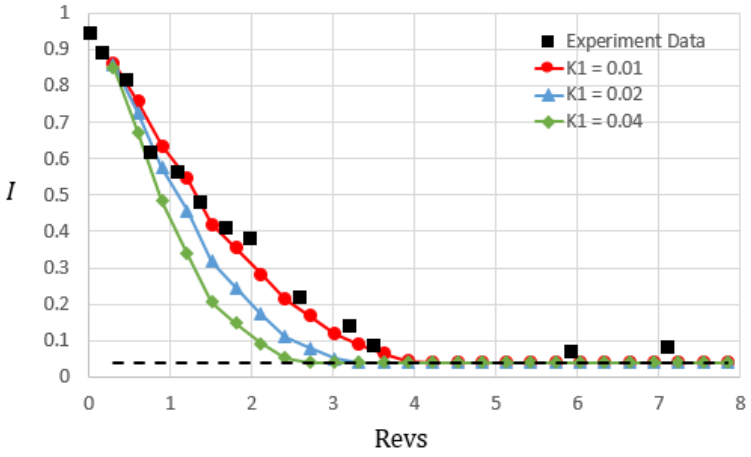

Figure 5.7 Segregation intensity with respect to the number of drum revolution for the experiment and the 2-D multi-scale model using different k_1 values.

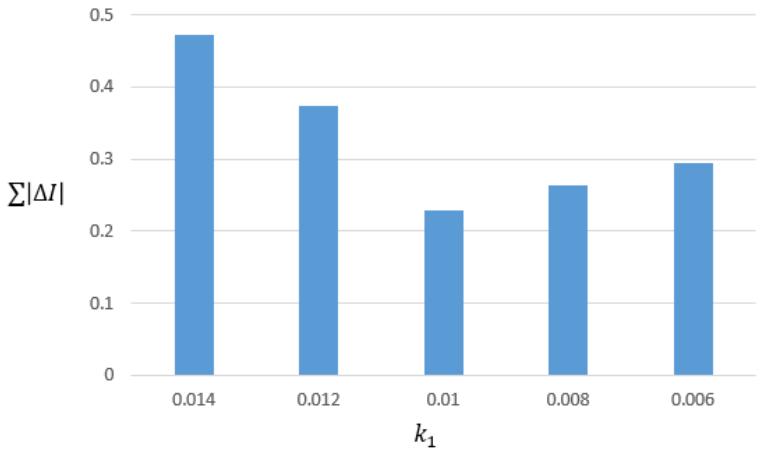

Figure 5.8 Sum of the absolute differences between the segregation intensities measured from experiments and computed from the 2-D multi-scale model for different k_1 values.

5.4 Comparison of the experiments and multi-scale model results

An FEM simulation was performed to predict the advective flow field information for the Sudah et al. Tote blender [81] using a rotation speed of 10 rpm and the material properties shown in Table 5.1. A mesh-dependency study was performed to ensure that the changes in maximum velocity in all three directions were not a function of the mesh. The maximum relative error of any velocity component was less than 5% when using a mesh with 125,000 elements as compared to a mesh consisting of 512,000 elements. Thus, the remainder of the FEM simulations were performed

using 125,000 elements. Furthermore, since transient velocity field information was used in the current work, the velocity components in all three directions needed to be outputted at every time step, which generates considerable amounts of data. Although the velocity field is not constant within a Tote blender single revolution, the material reaches a periodic steady state condition after a few initial revolutions. Table 5.3 shows the averaged velocity differences between subsequent revolutions, defined as

$$\left|\frac{\Delta v_i}{v_i}\right|_{\text{ave}} = \frac{\sum_{n=1}^{N}\left|\frac{v_{i,n}^{j} - v_{i,n}^{j+1}}{v_{i,n}^{j}}\right|}{N_n}, \tag{5.26}$$

where i is the direction of the velocity component, j is the revolution number, and N_n is the total number of nodes within the material domain. It is evident from Table 5.3 that the periodic steady state condition is reached after the first revolution. Therefore, to save computational effort without losing accuracy, the FEM simulation was only performed for two revolutions and the velocity fields within the second revolution were used in the multi-scale model subsequently.

Table 5.3 The averaged velocity differences between subsequent revolutions.

Revolution numbers (j, j+1)	(1,2)	(2,3)	(3,4)
$\left\|\Delta v_x / v_x\right\|_{\text{ave}}$	3.95%	0.56%	1.85%
$\left\|\Delta v_y / v_y\right\|_{\text{ave}}$	2.30%	0.38%	3.03%
$\left\|\Delta v_z / v_z\right\|_{\text{ave}}$	2.91%	1.18%	2.53%

In the experiments reported by Sudah et al. [81], materials were initially loaded into the Tote blender in two different ways: top-bottom loading and left-right loading. Two filling levels were also studied – 40% fill and 60% fill. The same loading conditions and filling levels were modeled in the current work, as shown in Figure 5.9. The color scale in Figure 5.9 is the same as Figure 5.3 and represents the field variable value from 0 (blue) to 1 (red). Figure 5.10 shows the evolution of the material domain within the first revolution for left-right loading and 40% fill.

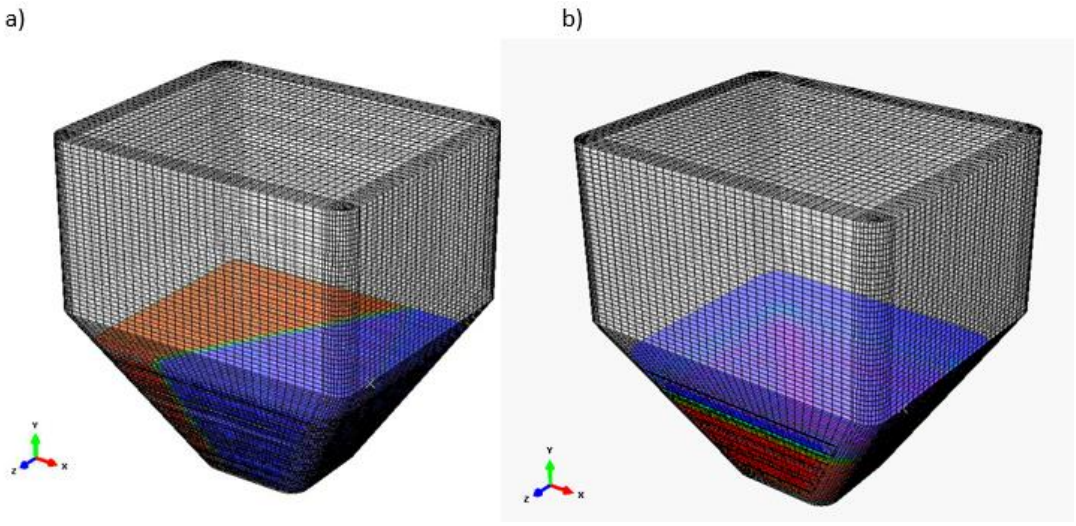

Figure 5.9 The left-right (a) and top-bottom (b) initial loadings for 40% fill.

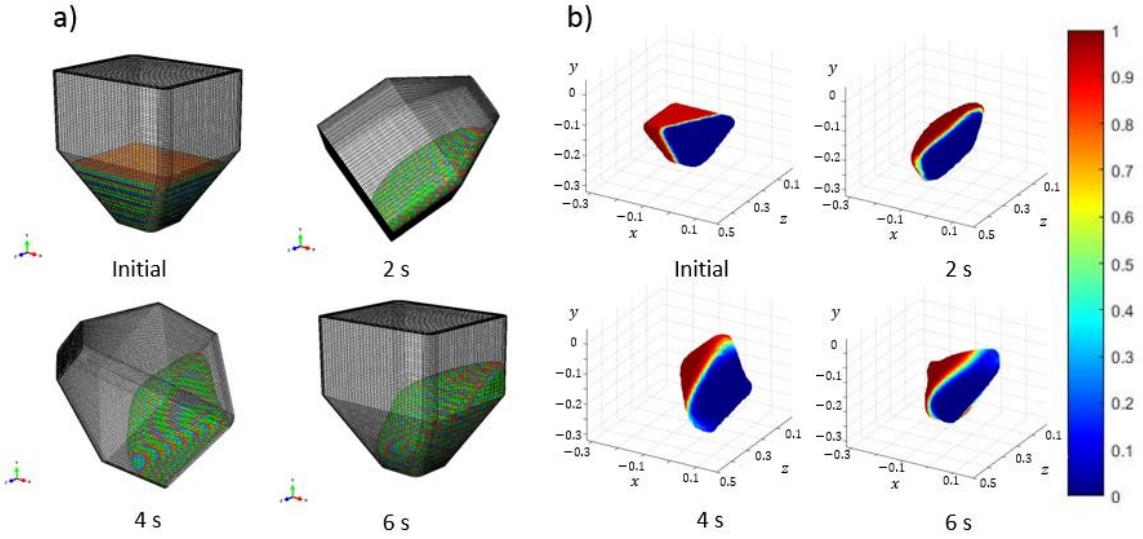

Figure 5.10 Snapshots showing the change of the material domain in the (a) FEM simulation and (b) multi-scale model for left-right loading and 40% fill. The vertical color scale in (b) is the red particle concentration.

The state of mixing predicted by the multi-scale model after different numbers of revolutions is shown in Figure 5.11. As expected, as time increases the degree of mixing increases, with both advection and diffusion contributing to the mixing process. Moreover, the top-bottom loaded materials mix much faster than the left-right loaded materials since the advective mixing is much stronger in the top-bottom loading case.

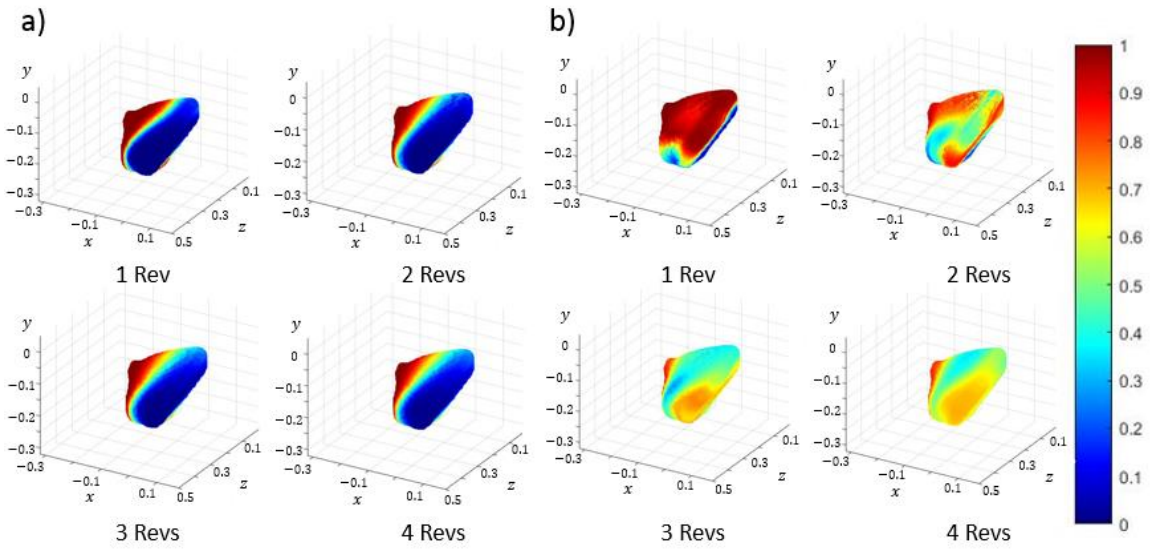

Figure 5.11 Snapshots showing the state of mixing at the end of each revolution for (a) left-right loading and (b) top-bottom loading and 40% fill. The vertical color scale is the red particle concentration for (a) and (b).

In the experiments by Sudah et al. [81], mixing curves were constructed by plotting the relative standard deviation (*RSD*) as a function of mixing time. The relative standard deviation is calculated as,

$$RSD = \frac{\sigma_i}{c_i}, \tag{5.27}$$

$$\sigma_i^2 = \frac{1}{N_s - 1}\sum_{m=1}^{M}\left(c_i - c_{i,m}\right)^2. \tag{5.28}$$

In the above equations, σ_i^2 is the measured variance of component i's concentration, c_i is the mean concentration of component i, and N_s is the total number of samples used to calculate the mean and variance. The relative standard deviation varies from zero, corresponding to perfect mixing, to one, which is a fully segregated state. The *RSD* value was also computed using the multi-scale model to compare with the published experimental results. Note that in the multi-scale model, every node at which a concentration is calculated is used in the evaluation of the segregation intensity, while in the experiments nine core samples were used [81]. Although the scale of scrutiny plays a role in the calculated results, as shown in Chapter 4, the predicted values using different grid sizes are close to each other.

Figure 5.12 plots the *RSD* values with respect to the number of revolutions for top-bottom and left-right initial loading patterns for the multiscale-model and experiments. Results for 40% and 60% fill levels were compared. In the current work, 1,000,000 cells were used to maintain accuracy and computational efficiency (i.e., 100 cells in each direction). A mesh dependency study was performed to ensure solution convergence and the error was found to be within 5% between 1,000,000 cells (i.e., 100 cells in each direction) and 3,375,000 cells (i.e., 150 cells in each direction). As shown in Figure 5.12, there is good quantitative agreement between the multi-scale model predictions and experimental measurements, although it does appear that there is some offset for the case with 40% fill and top-bottom loading. There is no error information given for the experimental results so it is difficult to determine how significant this difference is. The figure also indirectly shows the significance of the advective and diffusive components. For the side-side loading condition, the mixing is dominated by diffusive mixing while the top-bottom loading is dominated by advective mixing. Apparently, the influence of advective mixing is much stronger than the influence of diffusive mixing. The total wall-clock time required to run a single case on 10 cores, including the FEM simulation and MATLAB processing, was approximately 2.5 days.

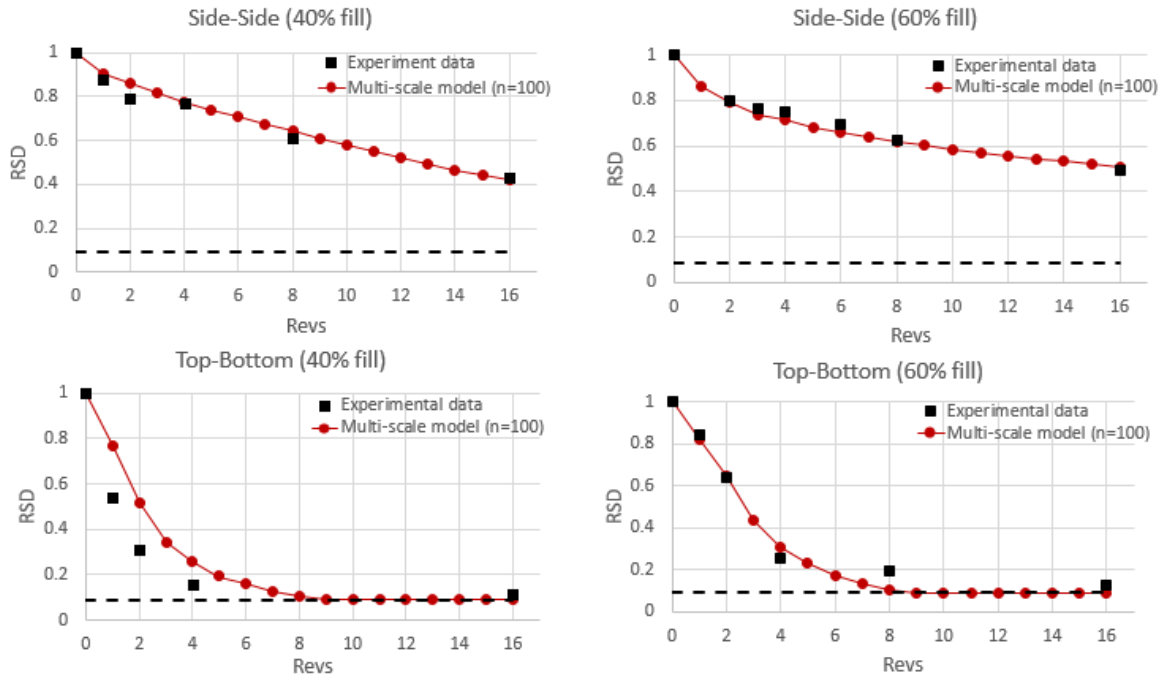

Figure 5.12 Mixing state comparison between published experimental results and the multi-scale model predictions. The random mixing state is represented by horizontal dashed lines and the spanwise diffusion constant is $k_1 = 0.01$.

To better understand the effects of model parameters, a parametric study was performed. The 60% fill and side-side loading case was used in the parametric study. As shown in Figure 5.13, the diffusion constant k_1 term is more significant than the k_2 term, and a larger diffusion constant results in a faster mixing. This result is consistent with findings in Chapter 4. Figure 5.13(a) also shows the quantitative contributions of advective and diffusive mixing. A value of $k_1 = 0$ means there is only advective mixing while $k_1 = 0.01$ means there is both advective and diffusive parts. For this loading condition, the influences of advective and diffusive mixing are both very important. However, it is expected that the relative contributions of advective and diffusive mixing will vary based on different loading and fill conditions. Simulations must be performed to quantitatively obtain the advective and diffusive contributions for a particular loading and fill condition.

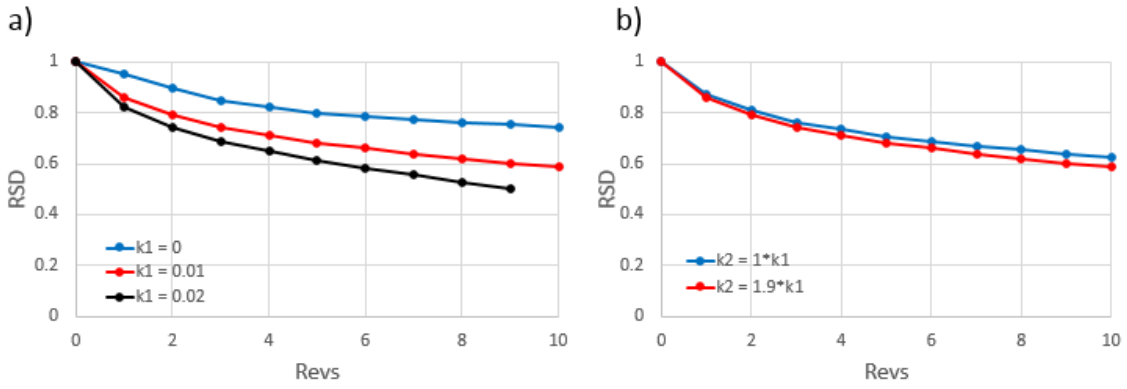

Figure 5.13 The relative standard deviation as a function of the number of revolutions for 60% fill and side-side loading for (a) different spanwise diffusion constants k_1, and (b) different streamwise diffusion constants k_2.

Figure 5.14 shows the effects of wall friction angle and internal friction angle. Figure 5.14(a) indicates that the mixing process is almost unaffected by the wall friction coefficient, which is consistent with previous findings in Chapter 4. Figure 5.14(b) shows that a larger internal friction angle results in faster mixing, resulting from a strong advective mixing contribution, but the trend is not very significant. In general, the advective movement of materials in a three-dimensional blender is difficult to estimate without predictive simulations.

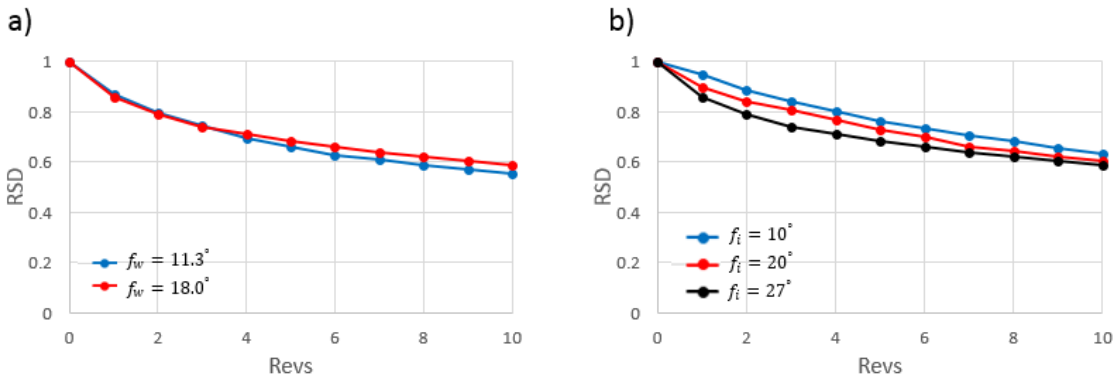

Figure 5.14 The relative standard deviation as a function of the number of revolutions for 60% fill and side-side loading for (a) different wall friction angle f_w, and (b) different internal friction angles f_i.

5.5 Study of the initial loading condition and fill method

As shown in Figure 5.12, the initial loading and fill conditions play an important role in the magnitude and rate of mixing within the Tote blender. Hence, studies have been performed to understand the effect of different loading conditions and fill methods.

5.5.1 Effect of the initial loading condition

According to the results shown in Section 5.4, one of the important factors affecting mixing rates in the Tote blender is the loading method. As shown in Figure 5.12, different loading methods lead to different mixing rates. Figure 5.15 plots three different initial loading conditions for the Tote blender simulation. The fill level for all three conditions is 60 % with 50/50 assembly, and the material properties and operation conditions are identical to those used in Section 5.4.

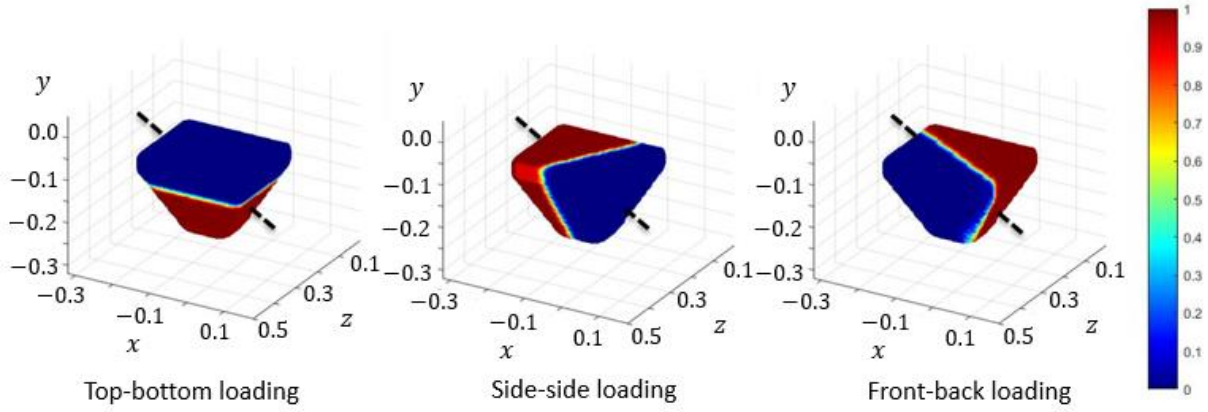

Figure 5.15 Different initial loading conditions used in the Tote blender simulation. The length scale unit is meter and the vertical color scale is the red particle concentration. The dashed line is the rotating axis.

Segregation intensity I, as defined in Chapter 4, is used to quantitatively compare the mixing rate of different loading conditions. As mentioned before, scale of scrutiny, i.e., the sample cell size, plays a minor rule with larger scales of scrutiny having smaller segregation intensities. Hence, for consistency, sample cubes with 25 mm edges were used in the current work. The segregation intensity as a function of the number of blender revolutions for the three different loading conditions is plotted in Figure 5.16. Clearly, the mixing rate is much faster for the top-bottom and front-back loading conditions than the side-side loading condition, indicating that the advective mixing is more dominant than the diffusive mixing. Moreover, it is shown that the mixing rates for top-bottom and front-back loading conditions are nearly the same, especially after 4 revolutions. In fact, both the top-bottom and front-back loading conditions belong to the same group where the normal axis of the surface that separates the particles of different color is perpendicular to the rotating axis of the blender. In these conditions, advective mixing is maximized. The side-side loading condition belongs to another group where the normal axis of the dividing surface is parallel to the rotating axis of the blender and hence, only diffusive mixing in applied. For practical purpose, to reach a faster mixing rate, the advective mixing should be always maximized and thus, top-bottom and front-back loading conditions should be used.

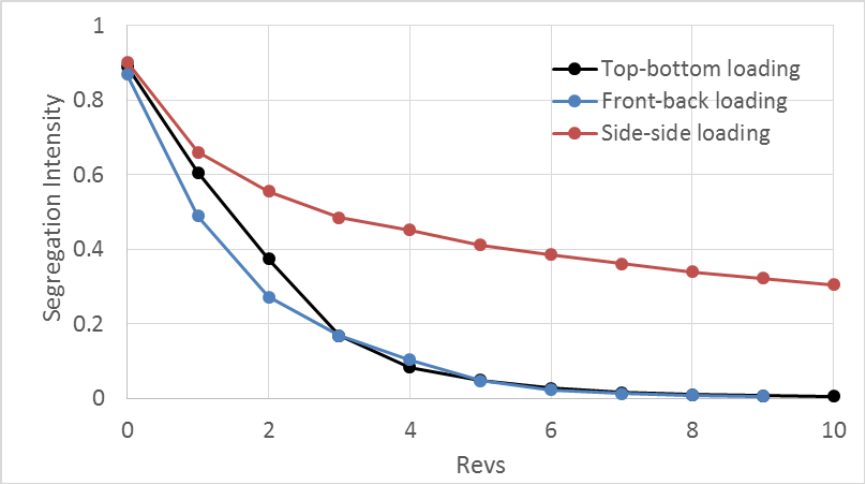

Figure 5.16 The segregation intensity as a function of the number of blender revolutions for different initial loading conditions shown in Figure 5.15.

5.5.2 Effect of the initial fill method

It is shown in Figure 5.12 that the fill level of the blender has a noticeable effect on the mixing rate. Figure 5.12 also illustrates that increasing the fill level slightly decreases the mixing rate, since increasing the fill level decreases the relative amounts of material in the flowing layer (the flowing layer depth does not significantly change with variations in fill level). However, note that previously the initial fill was always a 50/50 assembly. Hence, to further understand the effect of the initial fill method, different assemblies with different mass fractions of red particles are studied. Figure 5.17 plots three different initial assemblies for the Tote blender simulation. Here C_0 represents the mass fraction of red particles. Top-bottom loading and 60% fill were used for all three conditions and the material properties and operation conditions are identical to those used in Section 5.4.

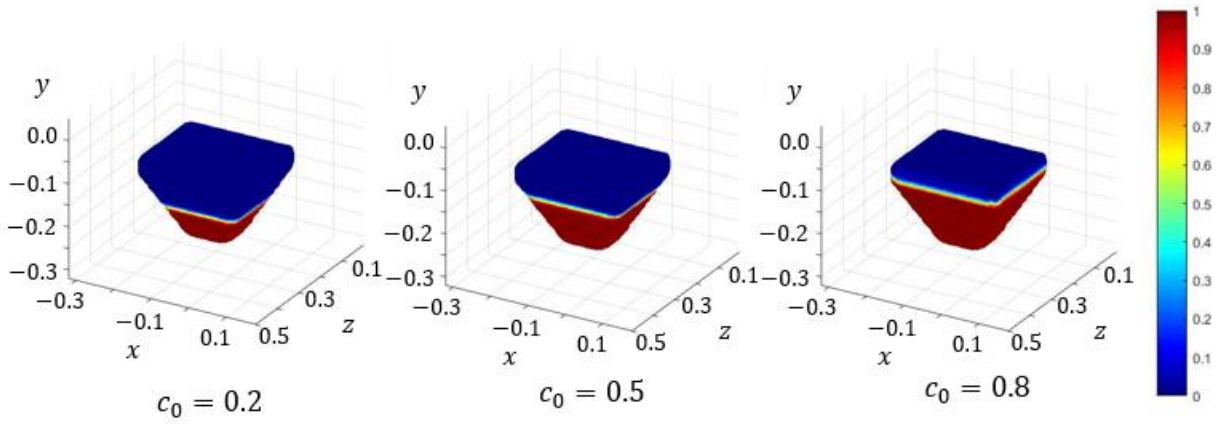

Figure 5.17 Different initial assemblies used in the Tote blender simulation. C_0 represents the mass fraction of red particles. The length scale unit is meter and the vertical color scale is the red particle concentration.

Since different initial assemblies were studied, mesh dependency tests have been performed to ensure the convergence of the results. Figure 5.18 plots the segregation intensity as a function of the number of blender revolutions for different numbers of cells. The mass fraction of red particles used here is a) 0.5 and b) 0.2. Log-linear scale is used in Figure 5.18 in order to better compare the results when segregation intensity approaches zero. Note that as mentioned in Chapter 4, the multi-scale model would predict an asymptotic segregation intensity of nearly zero, corresponding to a perfectly mixed state. However, a perfectly mixed state is generally not achievable in practice and instead a randomly mixed state is the expected asymptotic state. For practical purpose, assuming pharmaceutical tableting with granules of 500 μm diameter, and using the tablet size as the sample size, the segregation intensity corresponding to randomly mixed state is about 0.005, which is shown in Figure 5.18 as the dashed line. As mentioned in Chapter 4, the simulation is stopped after reaching the random mixed state.

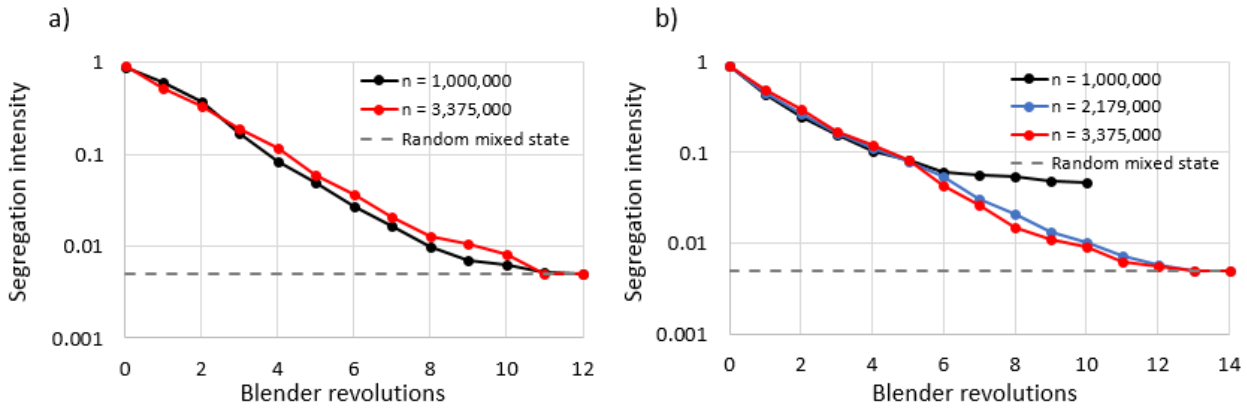

Figure 5.18 The segregation intensity as a function of the number of blender revolutions for different numbers of cells. The mass fraction of red particles, C_0, is a) 0.5 and b) 0.2.

As shown in Figure 5.18(a), the computed segregation intensity remains the same using 1,000,000 and 3,375,000 cells in the advection-diffusion calculation. However, Figure 5.18(b) shows that, when C_0 = 0.2, the computed segregation intensity is different after 6 revolutions using 1,000,000 and 3,375,000. This shows that when using 1,000,000 cells, the numerical diffusion starts to play a role and changes the mixing rate after 6 revolutions. In the contrast, the computed segregation intensity remains the same using 2,179,000 and 3,375,000 cells. Hence, to ensure the mesh convergence, a number of cells is chosen such that the numerical diffusion does not change the mixing rate until it reaches the randomly mixing state (i.e., I = 0.005 as mentioned before). According to the convergence result, 3,375,000 cells were used to run the simulation in the current study.

The segregation intensity as a function of the number of blender revolutions for different initial assemblies is plotted in Figure 5.19. The same sample size used in the previous section was used here as well. Note that the segregation intensity for the simulation with C_0 = 0.8 is slightly smaller than those for simulations with C_0 = 0.2 and 0.5 during the first few revolutions. This is because the simulation with C_0 = 0.8 has the largest dividing surface, as mentioned in the previous section and shown in Figure 5.17. Due to the linear interpolation method used to transfer data from Abaqus to Matlab, a larger dividing surface will introduce more initial mixing into the system. A finer FEM mesh can be used, if necessary, to reduce the initial mixing caused by the linear interpolation method. Overall, it is shown in Figure 5.19 that the mixing rate is not strongly affected by the mass

fraction of red particles studied in the current section. Future works should focus on studying the effect of initial assemblies with smaller mass fraction of red particles, such as C_0 = 0.1 and 0.005.

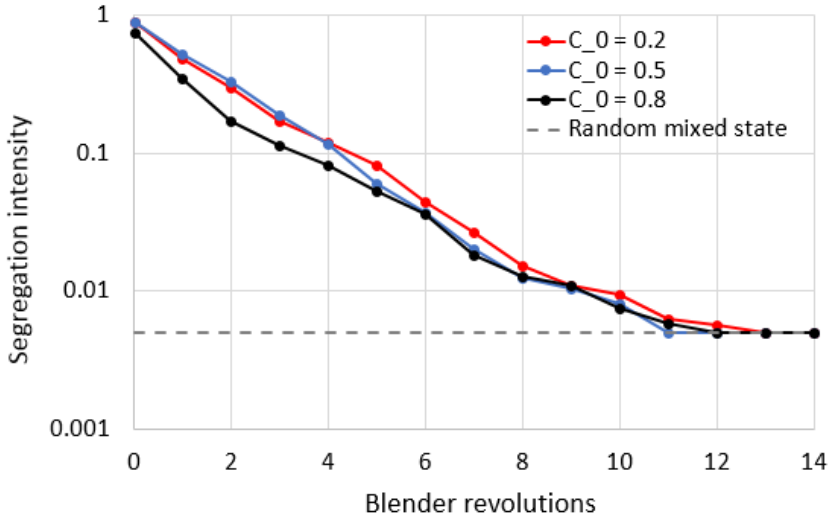

Figure 5.19 The segregation intensity as a function of the number of blender revolutions for different initial assemblies shown in Figure 5.17.

5.6 Summary

In this chapter, a three-dimensional transient multi-scale modeling approach is described for predicting blending in particulate systems. This model is extended from the two-dimensional steady model developed in Chapter 4. This three-dimensional model combines, within the advection-diffusion equation, finite element method generated transient macroscopic velocity fields with experimentally-obtained particle diffusion correlations at a local scale. The model is applied here to a three-dimensional Tote blender. Predictions of the mixing rate from the multi-scale model compare well quantitatively to published experimental data. Parametric studies demonstrate that both advective and diffusive mixing contribute significantly to the overall blending performance, but the relative importance of each component will mostly depend on the loading condition. Also, wall friction and internal friction appear to play little role in mixing for the studied conditions

CHAPTER 6. TWO-DIMENSIONAL MULTI-SCALE SEGREGATION MODEL

This chapter extends the model developed in Chapters 4 and 5 to include segregation. FEM simulations with a Mohr-Coulomb elasto-plastic material model are used to provide a prediction of the advective flow field. This flow field is combined with particle-level diffusion and shear-driven percolation segregation correlations to predict segregation in a rotating drum and hoppers of different geometries. The predictions are compared to DEM [42] and experimental [89] results available in the literature. Section 6.1 introduces the FEM modeling approach and its numerical implementation. Section 6.2 describes the advection-diffusion-segregation equation used in the model. Section 6.3 presents comparisons of the model predictions to the DEM and experimental results.

6.1 Finite element method model

Three-dimensional, coupled Eulerian-Lagrangian, FEM models [80,90,91] are used here to predict the advective flow field in a rotating drum and conical hoppers. The following sub-sections describe the model geometries, boundary conditions, and initial conditions for three different systems.

6.1.1 Simulation of a rotating drum

The commercial FEM package Abaqus/Explicit V6.14 is used to perform the simulations. The geometry of the simulated rotating drum, shown in Figure 6.1, is based on previous DEM simulations performed by Schlick et al. [42] and it mimics a lab-scale rotating drum with a diameter of 150 mm. Since a 2-D flow pattern was assumed in [42], both the front and back sides of the Eulerian mesh are regarded as planes of symmetry in the model with a narrow width of 10 mm used for computational efficiency. Gravity is included in the model with $g = 9.8$ m/s^2 directed in the negative y-direction. The rotational speed is 0.75 rad/s (7.2 rpm), corresponding to the previously published work [42]. The model setup is the same as the one in Chapter 4 and is shown in Figure 6.1 for convenience.

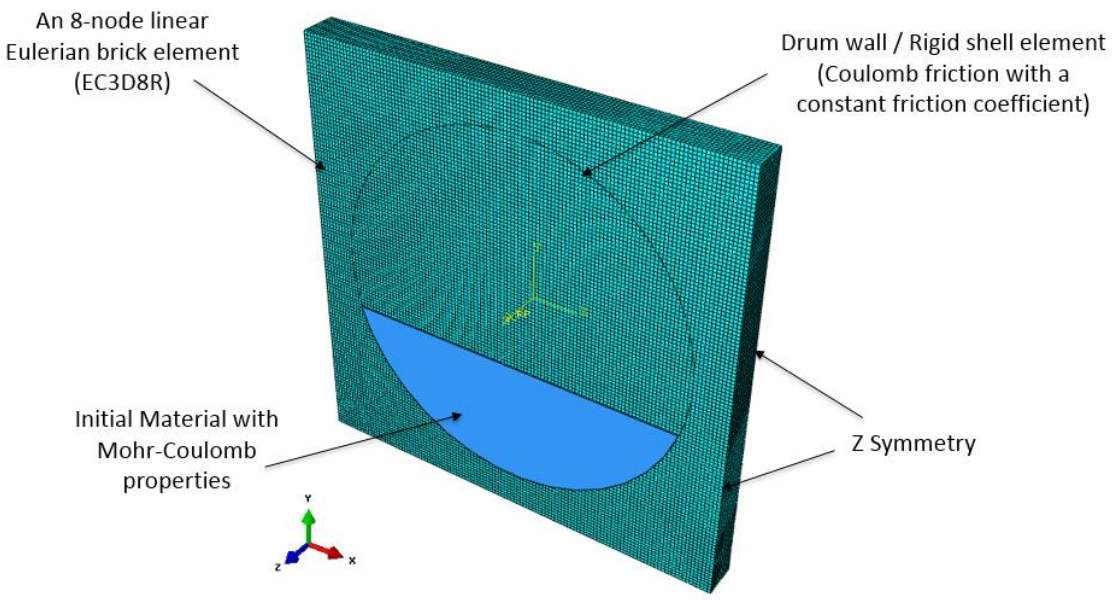

Figure 6.1 A schematic of the geometry modeled in the FEM simulations.

A Mohr-Coulomb elasto-plastic (MCEP) model is used in the current chapter to describe the stress-strain behavior of the particulate material. Details of this constitutive model are included in Chapters 3 and 4. Despite the simplicity of the MCEP model, it is shown to be sufficiently accurate at predicting velocity fields used in the quantitative prediction of segregation trends.

The material properties needed in the MCEP model are bulk density, Young's modulus, Poisson's ratio, dilation angle, material internal friction angle, and wall friction angle. All of these material parameters can be obtained from independent, standard material tests. For example, a uniaxial compression test can be used to calibrate the bulk density, Young's modulus, and Poisson's ratio, while a shear cell test can be used to calibrate the material's internal friction angle and wall friction angle. Detailed description of these experimental techniques is given in Chapter 4. As a side note, the effort required to obtain model parameters should not be underestimated. More complex material models can require many parameters, some of which may be difficult to obtain. In addition, many of the more complex material models are not implemented in commercial software, making their use for industrial practioners challenging. The MCEP provides a good balance between model accuracy, simplicity, and is already implemented in commercially available software and, thus, is worth consideration.

The Abaqus element mesh for the rotating drum is shown in Figure 6.1 and derived from the model described in Chapter 4. A Coupled Eulerian-Lagrangian (CEL) approach is used to handle the interactions between Eulerian and Lagrangian elements. The Eulerian Volume Fraction (EVF) value is used to determine the volume of material within each element. A value of EVF = 0 indicates that no material is present in the element while EVF = 1 indicates that the element is completely filled with material. Gravity is increased gradually to fill the drum and allow material to settle before the drum rotates. Further details can be found in Chapter 4.

6.1.2 Simulations of conical hoppers

Figure 6.2 shows the geometries of the simulated conical hoppers, which correspond to the hoppers used by Ketterhagen et al. [89] in their experimental work. The FEM discretization of these three-dimensional geometries is shown in Figure 6.3. A symmetry boundary condition is applied on the front side of the Eulerian mesh, as shown in Figure 6.3, and only half of the geometry is modelled to save computational time. Note that an axisymmetric boundary condition cannot be applied in the current model since it causes numerical errors along the axisymmetric axis (refer to Section 6.2.2). Hopper walls are modeled as rigid shells and fixed in all degrees of freedom. Gravity is included in the model with g = 9.8 m/s^2 directed in the negative y-direction.

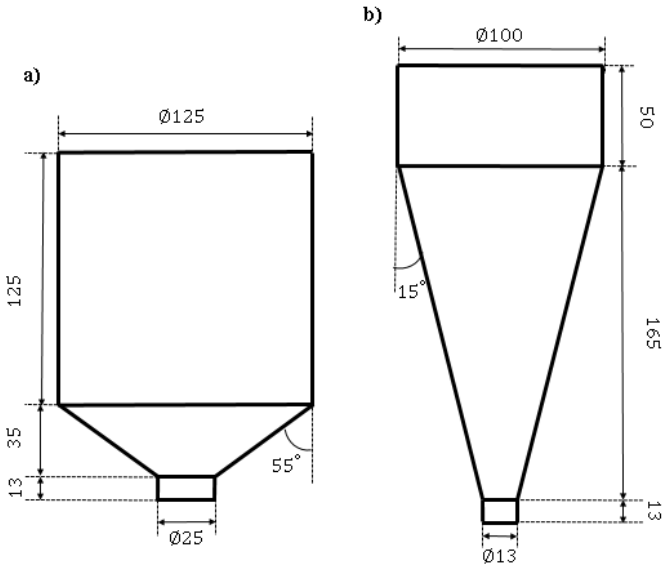

Figure 6.2 Schematics and dimensions of the experimental hoppers used by Ketterhagen et al. [89]. Length dimensions are in mm.

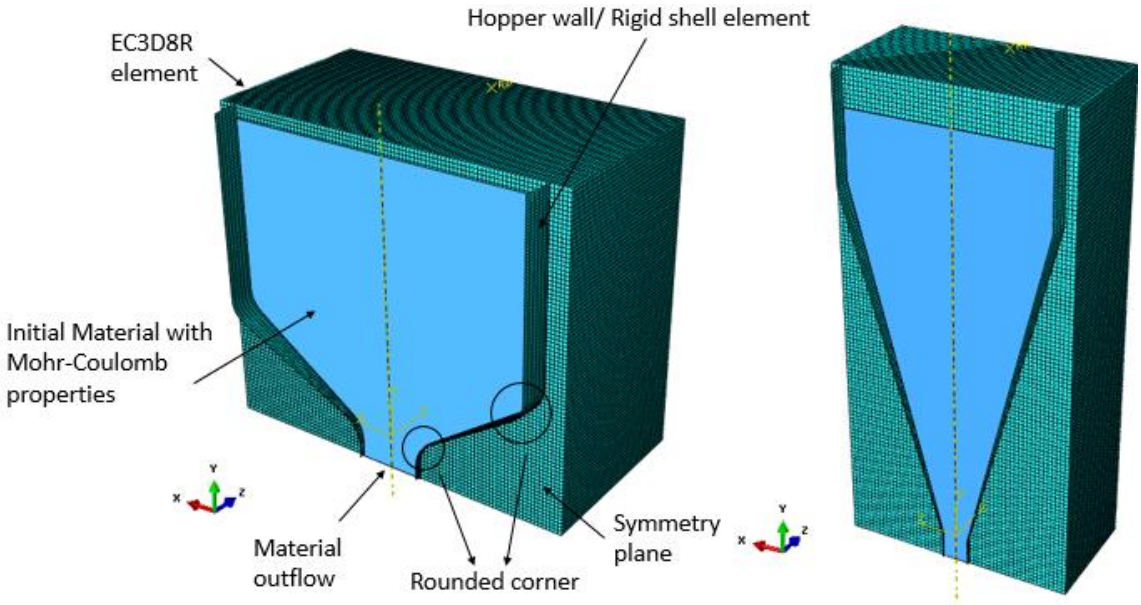

Figure 6.3 The discretization of the computational hopper domains.

Details of the material model and Abaqus implementations are the same as those described in Section 6.1.1. The hopper outlet is initially closed and, after the material settles under gravity within the Eulerian elements, the outlet is opened and discharge commences. Specifically, the outlet is opened by assigning a free-flow Eulerian boundary condition to the bottom plane, as shown in Figure 6.3.

It is worth noting that since a coupled Eulerian-Lagrangian (CEL) method is used, the Lagrangian mesh, i.e., the hopper wall, is placed inside the Eulerian mesh. A penalty method is then used to prevent material penetration and, thus, to ensure mass conservation. The algorithm calculates a repulsive contact force proportional to the penetration distance between the Lagrangian mesh and the material in the Eulerian mesh [92]. Naturally, a penalty method cannot strictly enforce the constraint and, hence, some penetration of Eulerian material into the Lagrangian boundary occurs. In most cases, this penetration is negligible; however, depending on the system geometry and material properties, severe penetration can occur in the simulation. There are a number of modeling procedures to overcome these severe cases, namely: (1) use a refined mesh in the region where penetration happens; (2) reduce the time step size so that a smaller penetration distance is used for the contact force; and (3) round sharp corners of the Lagrangian mesh, as shown in Figure 6.3.

6.2 The multi-scale segregation model

Since a quasi-2D rotating drum flow [42] and axisymmetric conical hopper flows [89] are studied in this work, a two-dimensional segregation model is developed as an extension of the two-dimensional mixing model in Chapter 4. The following sub-sections present the main aspects of the segregation model.

6.2.1 Advection-diffusion-segregation (ADS) equation

The advection-diffusion-segregation (ADS) equation is used to model the diffusion and shear-induced percolation segregation of a binary granular mixture and the resulting temporal and spatial concentration fields of the component materials. Specifically, the governing equation is,

$$\frac{\partial c_i}{\partial t} = \nabla \cdot \left(\boldsymbol{D} \nabla c_i \right) - \nabla \cdot \left(\boldsymbol{v} c_i \right) - \nabla \cdot \left(\boldsymbol{v}_p c_i \right), \tag{6.1}$$

where c_i is the local concentration of material species i (either small, $i = s$, or large, $i = l$, particles). The parameter $\boldsymbol{D}$ is the diffusion coefficient tensor for that species, $\boldsymbol{v}$ is the local advective velocity vector of the bulk material, and $\boldsymbol{v}_p$ is the percolation velocity vector. Since binary mixture is studied in the current work, $\boldsymbol{D}$ and $\boldsymbol{v}_p$ represent the mixing and segregation parameters between the two species. Note that previous work has shown that the self-diffusion coefficient $\boldsymbol{D}$ is an anisotropic tensor quantity [66,80,90]. However, Fan et al. [31] showed that for segregation-dominated flows, a constant D, namely, the mean diffusion coefficient in the spanwise direction, can still lead to an accurate prediction. Hence, for simplicity, a constant diffusion coefficient D is used in the current model, which is assumed independent of particle size, shear rate, and local concentration, consistent with previous work [31].

The percolation velocity $\boldsymbol{v}_p$ derived by Fan et al. [31] is adopted in the current model. In their work, heap flows were studied and, thus, only the normal component of the percolation velocity relative to the mean normal flow was considered. The streamwise component was neglected. Here, gravity acts in the negative y-direction and percolation is dominant in the direction of gravity [59,93]. Therefore, the x-component of the percolation velocity is neglected and only the y-component is considered. Moreover, according to Fan et al. [31], the percolation velocity can be approximated as a linear function of the shear rate and the concentration of the other species in a bi-disperse mixture, i.e.,

$$v_{p,s} = -S\left|\dot{\gamma}\right|(1-c_s)\,,\; v_{p,l} = S\left|\dot{\gamma}\right|(1-c_l)\,, \tag{6.2}$$

where S is the percolation length scale and $\left|\dot{\gamma}\right|$ is the magnitude of the spanwise shear rate. Note that, unlike the diffusion coefficient, the percolation speed does depend on the local particle concentration.

Relationships for the percolation length scale S as a function of the particle diameter and small to large particle ratio have been proposed [31,42,59,60]. However, in this work, a percolation length either previously reported [42] or fitted to experimental data [89] is used. Finally, since the percolation in the y-direction is mainly caused by the shear rate in the x-direction, the y-component of the shear rate is neglected and the shear rate is approximated by,

$$\left|\dot{\gamma}\right| \approx \left|\dot{\gamma}_x\right| = \left|\frac{\partial v_x}{\partial y}\right|. \tag{6.3}$$

Using the local mass conservation equation, adopting the relationship presented above (Eqs. (6.2) and (6.3)), and assuming an incompressible material, i.e.,

$$\nabla \cdot \boldsymbol{v} = 0\,, \tag{6.4}$$

Eq. (6.1) may be written in index notation form as,

$$\frac{\partial c_i}{\partial t} = D\left(\frac{\partial^2 c_i}{\partial x^2} + \frac{\partial^2 c_i}{\partial y^2}\right) - \left(v_x \frac{\partial c_i}{\partial x} + v_y \frac{\partial c_i}{\partial y}\right) - \frac{\partial\left[\pm S\left|\frac{\partial v_x}{\partial y}\right|(1-c_i)c_i\right]}{\partial y}\,, \tag{6.5}$$

where the $\pm$ sign is determined by the size of the particles, as indicated in Eq. (6.2).

6.2.2 Numerical method

The numerical method used to solve the ADS equation in the current chapter is the same one used in Chapters 4 and 5. A finite difference method based on a second-order Tylor Lax-Wendroff scheme is used to solve Eq. (6.5) due to the method's simplicity and computational efficiency [70]. The second order scheme can be written as,

$$\begin{aligned} c_{ij}^{n+1} = c_{ij}^n &- \left[\nu_x \Delta_{x0} c_{ij}^n - \left(\frac{1}{2}\nu_x^2 + \mu_x\right)\delta_x^2 c_{ij}^n\right] - \left[\nu_y \Delta_{y0} c_{ij}^n - \left(\frac{1}{2}\nu_y^2 + \mu_y\right)\delta_y^2 c_{ij}^n\right] \\ &+ \nu_x \nu_y \Delta_{x0}\Delta_{y0} c_{ij}^n \mp S\left[\Delta_y\left|\Delta_y\left(v_x\right)_{ij}\right|\left(1-c_{ij}^n\right)c_{ij}^n + \left|\Delta_y\left(v_x\right)_{ij}\right|\left(1-2c_{ij}^n\right)\Delta_y c_{ij}^n\right]\Delta t \end{aligned}\,, \tag{6.6}$$

where the advection and diffusion terms are given in Section 4.2.2 as Eqs. (4.8)-(4.18), with the segregation terms to be,

$$\left|\Delta_y \left(v_x\right)_{ij}\right| = \left|\frac{\left(v_x\right)_{i+1,j} - \left(v_x\right)_{i-1,j}}{2 \cdot \Delta y}\right|, \tag{6.7}$$

$$\Delta_y \left|\Delta_y \left(v_x\right)_{ij}\right| = \frac{\left|\Delta_y \left(v_x\right)_{i+1,j}\right| - \left|\Delta_y \left(v_x\right)_{i-1,j}\right|}{2 \cdot \Delta y}, \text{ and} \tag{6.8}$$

$$\Delta_y c_{ij}^n = \frac{c_{i+1,j}^n - c_{i-1,j}^n}{2 \cdot \Delta y}. \tag{6.9}$$

The computational molecule for this scheme is shown in Figure 4.4. Note that since a finite difference method is used, the Von Neumann conditions must be checked to ensure the stability of the numerical computations.

A MATLAB program is used to iterate the finite difference scheme. A C++ code was developed to read and process the large FEM output files (.obd files). The material boundaries computed within the FEM simulation from the Eulerian Volume Fraction (EVF) values are used directly by the MATLAB algorithm. To ensure mass conservation of each species, the segregation and diffusion fluxes are set to zero on the boundary and, thus, material cannot exit the domain by advection. A threshold is set to ensure the material concentration value remains between zero and one, and a small time step is carefully chosen to ensure the stability of the explicit scheme. The same as Chapter 4, a fitting approach is applied to ensure that the material concentration of the boundary node is equal to the value of the node that is one grid point inward, a scheme commonly employed in CFD computations ([71]). Note that this fitting approach restricts the use of an axisymmetric boundary condition since the material nodes along the axisymmetric axis would be treated as boundary nodes as well.

Mesh dependency studies were performed to ensure the convergence of the numerical results for both the FEM and the ADS equation calculations. For the FEM simulations, comparisons of the averaged velocity differences in the system were compared to determine convergence, with the details shown in Table 6.1. The velocity differences were averaged between 10 different points

along the free surface of the rotating drum and the outlet of the hopper. For both systems, the FEM solutions were insensitive to the mesh sizes and, thus, 500,000 and 176,000 elements were used in the rotating drum simulation and hopper simulations, respectively. Detailed mesh convergence results for the ADS equation calculations are given in Sections 6.3.

Table 6.1 Convergence study results for the FEM simulations.

	Number of elements		Averaged velocity differences
	Case 1	Case 2	
Rotating drum	500,000	1,280,000	2.74%
15° hopper	176,000	411,000	3.27%

Note that to achieve numerical convergence and stability, the number of nodes used in the second-order Tylor Lax-Wendroff scheme must be much larger than the number of nodes in the FEM mesh. A linear interpolation algorithm, implemented in MATLAB, is used to transfer data from the FEM nodes to the ADS nodes.

The initial conditions used in the simulations correspond to a perfect mixture since segregation is the main focus of this work. Refer to Chapters 4 and 5 for examples of granular systems that are initially partially mixed or separated and are then blended.

6.3 Results

In this section, predictions from the FEM-ADS equation models are compared to previously published DEM and experimental results. Specifically, the segregation profile normal to the bed surface is examined for a rotating drum and the temporal variation in the fraction of fine particles at discharge is compared for two different hoppers. In addition, qualitative examination of the particle concentration fields are discussed.

6.3.1 Rotating drum

The rotating drum FEM-ADS model predictions are compared to bi-disperse particle segregation DEM results reported by Schlick et al. [42]. The parameters used in the FEM simulations are given in Table 6.2 and correspond to the properties derived from DEM simulations of 1 mm diameter, identical spherical particles with the material properties given in Chapter 4. The FEM-ADS models described here are one-way coupled, which means that the bulk flow field determined from the FEM model is unaffected by the local particle species concentration.

Table 6.2 Parameters used in the rotating drum FEM simulation.

Parameter	Value
Material density (kg/m^3)	1500
Young's modulus (MPa)	3.65
Poisson's ratio (-)	0.065
Internal friction angle (degree)	23.6
Cohesion (Pa)	0
Dilation angle (degree)	0.1
Wall friction coefficient (-)	0.324

There are two differences between these previous DEM simulation parameters and those of the Schlick et al. work [42]. First, Schlick et al. used a particle-wall friction coefficient of 0.4 while Chapter 4 used a value of 0.3. This difference is expected to have little impact since Chapter 4 demonstrated that changing the particle-wall friction coefficient had little impact on the flow behavior. The reason is that the first avalanche always occurs at the same location and the free surface angle remains constant as long as the wall friction is sufficiently large to lift the material without sliding. Second, the Schlick et al. work used a 50/50 bi-disperse assembly of 1 mm and 3 mm spheres while the DEM simulations used in Chapter 4 to calibrate the FEM parameters used identical 1 mm particles.

The dilation of cohesionless granular materials is usually small and, thus, a dilation angle of 0.1° was adopted, which is the minimum value allowed in Abaqus for the MCEP model. The Poisson's ratio is very small because the powder bed is loose, with a relative density around 0.3, and thus it is very compressible, as shown in Chapter 4.

Schlick et al. used particles with 1 mm and 3 mm diameters in their DEM simulations [42]. As mentioned previously, the FEM material parameters were calibrated using 1 mm particles only. To verify that the FEM model predicted the flow field accurately, the surface velocity in the streamwise direction of the DEM simulation reported by Schlick et al. was compared with that of an FEM simulation using the material parameters in Table 6.2 when the rotation speed ω is 0.75 rad/s (7.2 RPM). Figure 6.4 shows that these two velocities are similar despite having different particle sizes. The maximum thickness of the flowing layer δ_0 was also compared, and the values predicted by the DEM and FEM simulations differ by, at most, 8% (14.8 mm for the former and 13.6 mm for the latter). This close similarity indicates that the Mohr-Coulomb properties listed in Table 6.2 represent the granular system used in the DEM simulations with sufficient accuracy for the rotating drum studied. This similarity may not hold true for other geometries with large particle size differences since previous work has shown that the velocity field can be influenced by the particle size [42].

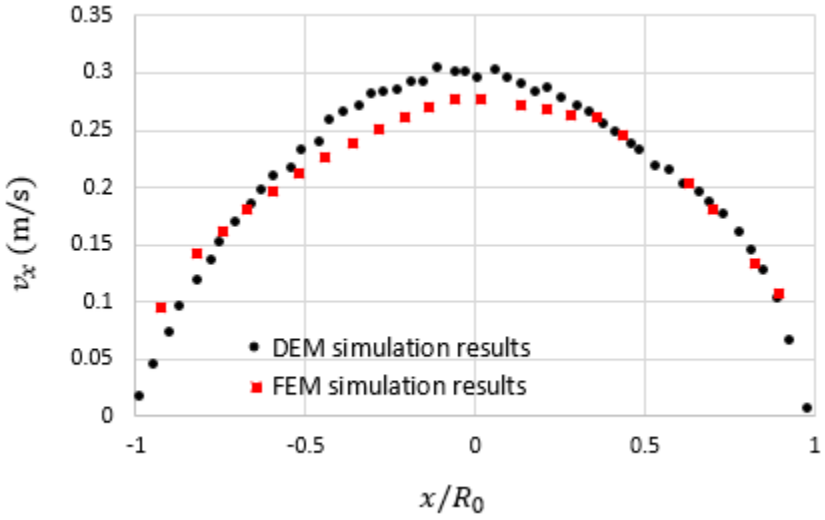

Figure 6.4 Surface velocity as a function of the streamwise position at ω = 0.75 rad/s (7.2 RPM). The coordinate system used in the plot is identical to the one used by Schlick et al. [42] for consistency, where *x* is the streamwise direction in the flowing layer.

As mentioned before, it is necessary to know the diffusion coefficient D and the percolation length scale S in order to compare results from the FEM-ADS model with those from DEM simulations. These values were found in [42] for rotating drum DEM simulations of 1 mm and 3 mm diameter spheres with $\omega = 0.75$ rad/s (7.2 RPM) to be $D = 16.1$ mm^2/s and $S = 0.29$ mm.

Figure 6.5 shows the spatial evolution of the small particle concentration at different times predicted by the FEM-ADS model. The drum is half-filled with initially well-mixed particles, i.e., $c_s = c_l = 0.5$ at every material point in the domain. As expected for a bi-disperse granular system, as time increases the degree of segregation increases. It is evident from the figure that small particles segregate to the bottom of the flowing layer and gather in the center of the material domain inside the drum. The same trend was also captured in the previous DEM simulations of Schlick et al. [42]. Hence, qualitatively, the multi-scale model reproduces the segregation pattern observed in the DEM simulations.

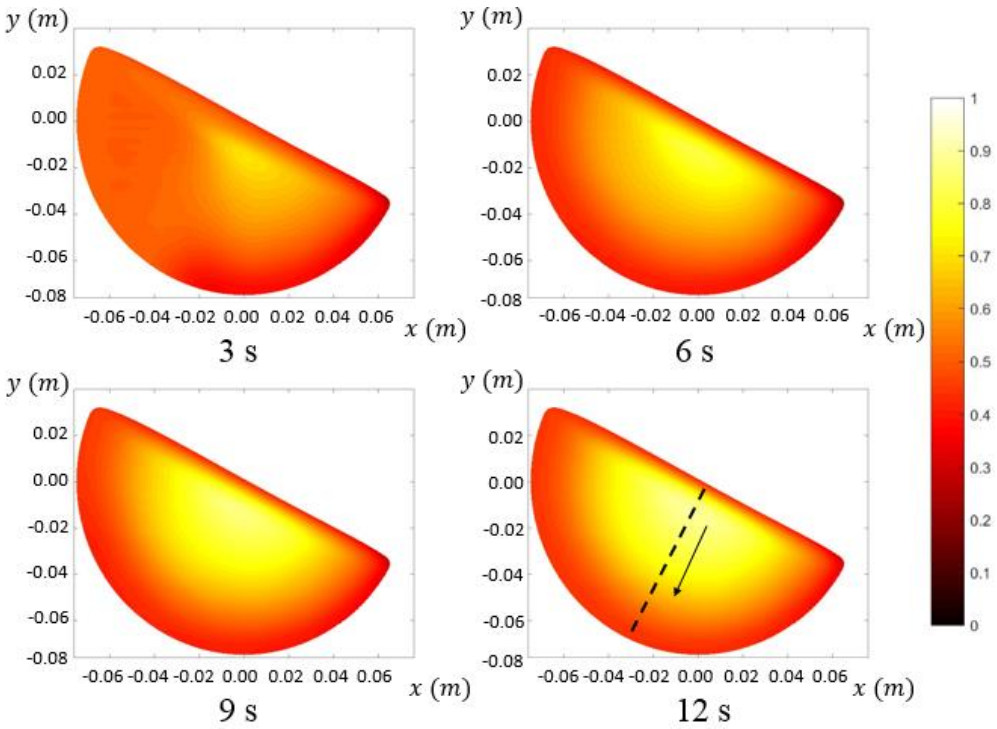

Figure 6.5 Snapshots showing the small particle concentration in the simulated rotating drum at different times. The dashed line at 12 s is the path used to plot the small particle concentration quantitatively.

To provide a quantitative comparison of the two modelling approaches, the steady-state concentration of small particles is plotted in Figure 6.6 as function of the dimensionless distance δ / R_0 along the center of the bed starting from the free surface, i.e., along the dashed line shown in Figure 6.5. The distance is made dimensionless using the radius of the drum R_0. The figure indicates that there is good quantitative agreement between the two models, although the FEM-ADS model slightly overpredicts the small particle concentration near drum walls. The total wall-clock time required to run the FEM (16 cores with the Intel Xeon CPU E5-2680 v3 processor) and ADS (MATLAB, single core with the same processor) simulations was approximately two days. Note that a mesh dependency study was performed to ensure the convergence of the ADS equation calculations. The small particle concentration along the center of the bed, as shown in Figure 6.6, was computed using 250,000 and 1,000,000 elements, respectively. The averaged error among all computed data points was 3.56% and, hence, 250,000 elements were used in the remainder of the rotating drum simulations.

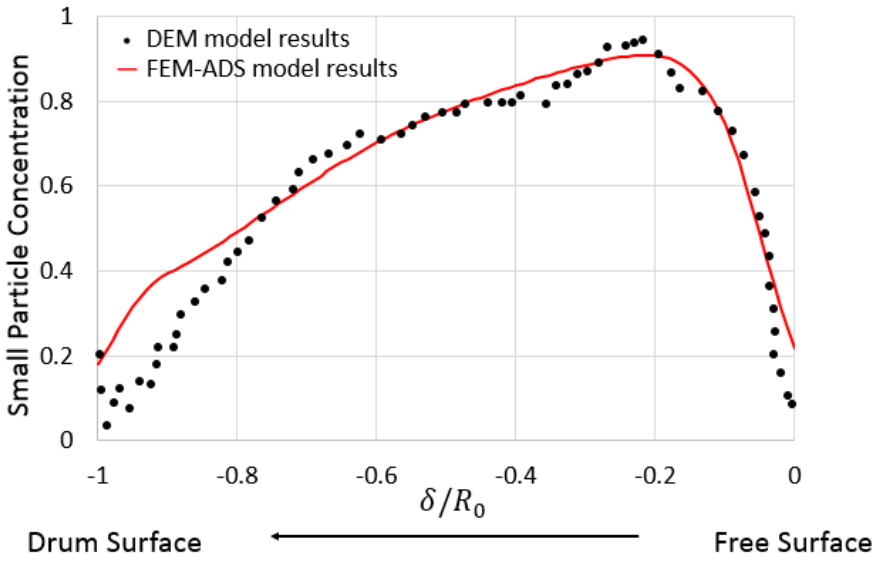

Figure 6.6 Steady-state concentration of small particles as a function of dimensionless distance from the free surface, δ / R_0, along the centerline of the drum. The DEM model results are from previous work by Schlick et al. [42].

To better understand the effects of the model parameters, a parametric study was performed using the rotating drum simulation. The model is identical to the one described previously except for the values of the diffusion coefficient *D* and percolation length scale *S*. Figure 6.7(a) shows the results

for simulations where the percolation length scale remains the same while the diffusion coefficient changes and Figure 6.7(b) shows the results when the diffusion coefficient remains the same and the percolation length scale changes. Clearly, segregation is stronger as the diffusion coefficient decreases and percolation length increases. This same trend was predicted by Schlick et al. [42]. It is also shown that segregation is dominated more by the percolation than the diffusion, and the effect of percolation and diffusion decreases as the powder bed approaches a fully segregated state. Moreover, it is noticed in both Figs. 6.7(a) and (b) that the maximum small particle concentration occurs at the bottom of the active layer since small particles fall to the bottom of the flowing layer as they move downstream and gather in the center of the bed. Also, when the diffusion coefficient is large or the percolation length scale is small, there is a small "mixing band" at around δ / R_0 = -0.9. This behavior occurs as a result of the small velocity gradient caused by wall friction close to the drum wall. A large diffusion coefficient and small percolation length scale results in more mixing in this region.

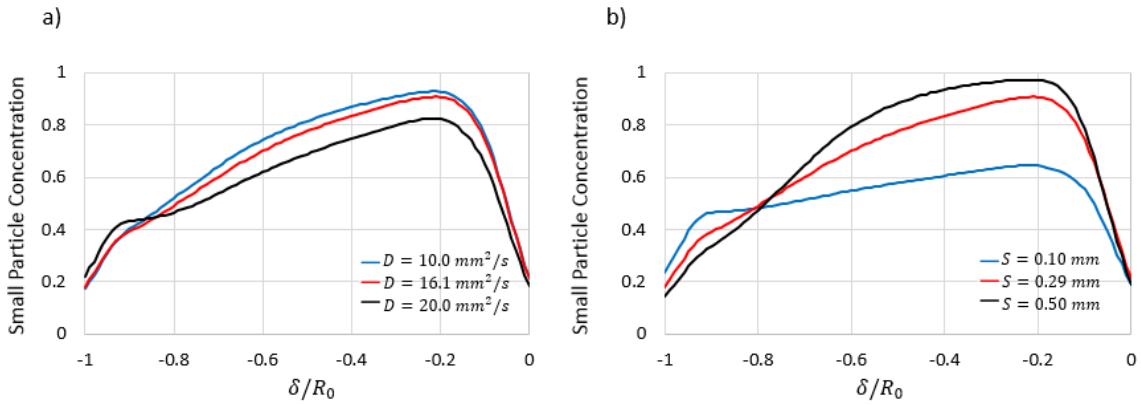

Figure 6.7 The steady state small particle concentration plotted as a function of dimensionless distance from the free surface, δ / R_0, along the centerline of the drum for a) different diffusion coefficients D and b) different percolation lengths S. Other model parameters are the same as those used in Table 6.2.

6.3.2 Conical hoppers

Experimental work on bi-disperse particle segregation carried out by Ketterhagen et al. [89] was used to further validate the predictions of the FEM-ADS model. The experimental setup consists of bench scale hoppers (ASTM D 6940-03) and binary mixtures of glass beads, as shown in Figure 6.2. The initial hopper fill height is 105 mm for the 55° hopper and 210 mm for the 15° hopper.

The Mohr-Coulomb properties used in the FEM simulations should, preferably, be calibrated from experimental characterization. Unfortunately, these values were not reported in the Ketterhagen et al. work [89] and, therefore, these material properties are determined here from the DEM particle properties used by Ketterhagen et al. [89], which showed good quantitative agreement with experimental results. Specifically, the internal friction angle and wall friction angle were calibrated using DEM simulations of an annular shear cell (see Chapter 4 for details of this calibration procedure). Note that in the experiments by Ketterhagen et al. [89], the mass fractions of small particles were relatively small (10%). Hence, the particle diameter used in the DEM calibration simulations is identical to the large particle diameter with d = 2.24 mm. Material density, elastic modulus, and Poisson's ratio are known to have little influence on the granular flow behavior, and are assumed here to be the same as those obtained for hard spheres, as shown in Table 6.2. Dilation of cohesionless granular materials is assumed here for hard spheres as well. Finally, particle shape and size effects are lumped together with bulk and transport material properties used in the model. Tables 6.3 and 6.4 show the DEM and FEM material parameters, respectively.

Table 6.3 Parameters used by Ketterhagen et al. [89] in DEM simulations.

Parameter	Value
Particle density (kg/m^3)	2520
Particle-particle coefficient of restitution (-)	0.94
Particle-wall coefficient of restitution (-)	0.90
Particle-particle friction coefficient (-)	0.1
Particle-wall friction coefficient (-)	0.5
Rolling friction coefficient (-)	0.045

Table 6.4 Parameters used in FEM hopper discharge simulations.

Parameter	Value
Material density (kg/m^3)	1500
Young's modulus (MPa)	3.65
Poisson's ratio (-)	0.065
Internal friction angle (degree)	18.4
Cohesion (Pa)	0
Dilation angle (degree)	0.1
Wall friction coefficient (-)	0.31

Since no velocity information was given in the previous work [89], the velocity profiles cannot be compared directly. However, there is extensive evidence that FEM models can accurately predict the velocity field of granular flows [56–58,80,90]. Therefore, the velocity profiles predicted by FEM simulations of the hopper geometries shown in Figure 6.2 are used to predict segregation during discharge.

As mentioned before, a single diffusion coefficient D, as opposed to an anisotropic tensor, leads to accurate predictions in segregation-dominated flows [31]. Also, as shown in Figure 6.7, segregation is dominated more by the percolation than the diffusion. Therefore, the diffusion coefficient calibrated in Chapter 5 in the spanwise direction of the active layer is adopted and assumed homogeneous. The value is then determined by averaging the diffusion coefficient in the entire flowing layer in the hopper after the flow becomes steady.

The percolation length scale S is calibrated to one set of experimental data and used to predict other experimental configurations. Specifically, the aim is to reproduce the experimentally-observed normalized mass fraction of fines x_i/x_f, where x_i is the mass fraction of fines collected at discharge in a given sample and x_f is the initial mass fraction of fines. Figure 6.8 shows the normalized mass fraction of fines x_i/x_f as a function of the fractional mass discharged M/M_{total}, where M is the cumulative mass discharged and M_{total} is the initial total mass inside the hopper.

The experiment was performed in the 55° hopper with a well-mixed initial fill. The initial mass fraction of fines is 10% with the particle diameters for small and large particles equal to 1.16 mm and 2.24 mm, respectively. The multi-scale model predictions are also shown in Fig 6.8 with different assumed values of the percolation length scale *S*. Note that in the FEM simulations, due to the penalty contact algorithm used, as described in Section 6.1, the material tends to attach to the wall when almost fully discharged. Thus, the simulations are not a good description of the final stage of the discharge process. Regardless of this limitation, it is evident from the figure that the FEM-ADS model can predict the segregation pattern during hopper discharge with good qualitative accuracy.

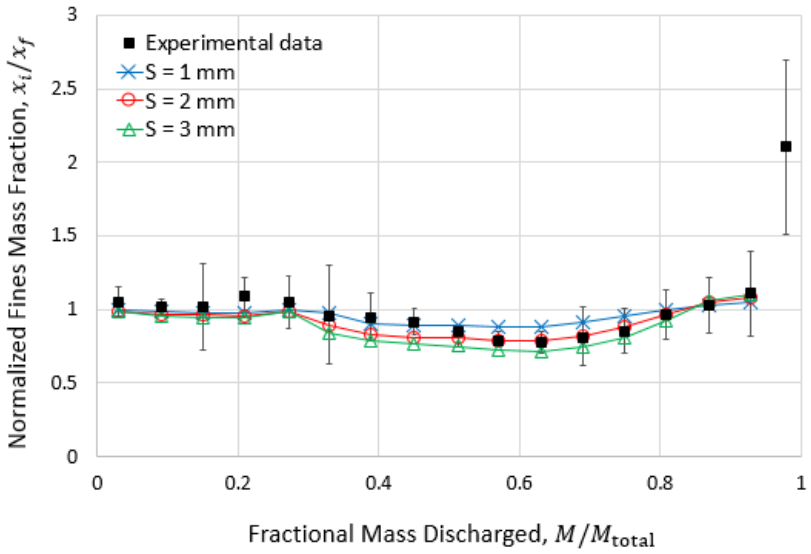

Figure 6.8 Experimental and FEM-ADS model predictions of the normalized mass fraction of fines with respect to the fractional mass discharged for different percolation length scale (*S*) values. The hopper angle is 55° and the initial fines mass fraction is 10%. Scatter bars denote the 95% confidence interval of the experimental results.

Figure 6.9 shows the calibration error for different values of *S*. The calibration error is defined as the averaged absolute differences in the normalized mass fraction of fines compared to the experimental results. The figure suggests that a value of S = 2 mm is optimal for the percolation length scale of the tested system. It is worth noting that this *S* value is about seven times larger than the one used in Section 6.3.1 for the material system in the rotating drum. The reason for the difference may be that a smaller particle-particle friction coefficient is used in the hopper discharge

simulation as compared to the rotating drum. A smaller particle-particle friction coefficient would make it easier for small particles to percolate through the large particles and, thus, give a larger percolation length scale.

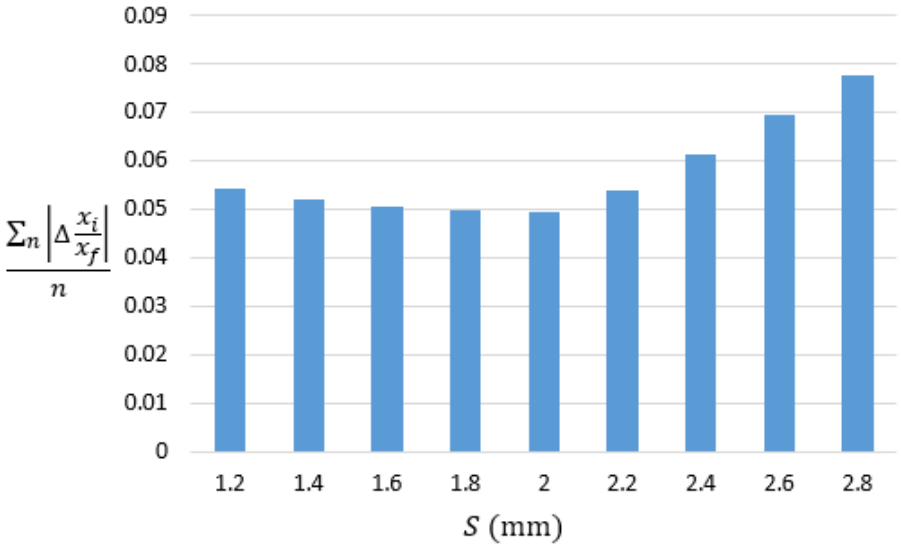

Figure 6.9 Averaged absolute differences between experimental values and FEM-ADS model predictions of the normalized mass fraction of fines, for different S values.

The FEM-ADS model calibrated with data from the 55° hopper (S = 2 mm) is now compared to the experimental data from the 15° hopper using a well-mixed initial fill and 10% initial mass fraction of fines. The diffusion coefficient D is equal to 0.6 mm^2/s for the 15° hopper discharge simulation. As mentioned previously, this value is determined by averaging the diffusion coefficient in the entire flowing layer of the 15° hopper. This value is different from the diffusion coefficient calibrated for 55° hopper since the velocity field changes between these two hoppers. Figure 6.10 depicts the small particle concentration spatial and temporal evolution. It is evident from the figure that segregation mainly occurs near the free surface where large particles tend to roll down the incline towards the hopper centerline. Since velocities are the largest near the centerline, these large particles are discharged first. This trend is in agreement with the experimental observations reported by Ketterhagen et al. [89] indicating that the multi-scale model qualitatively predicts the segregation pattern during hopper discharge.

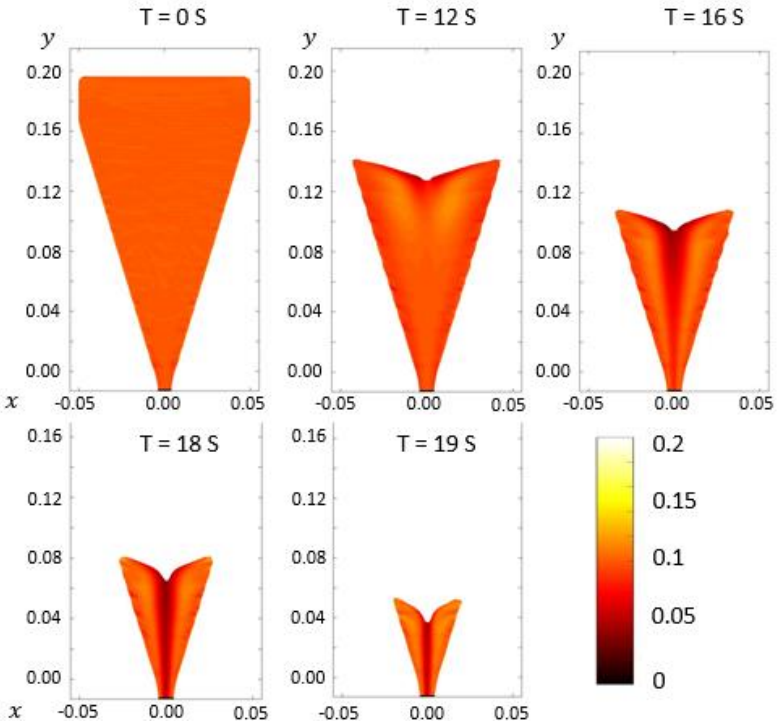

Figure 6.10 Simulation snapshots showing segregation evolution. The vertical color scale corresponds to the concentration of small particles.

Figure 6.11 shows the normalized mass fraction of fines as a function of the fractional mass discharged for the 15° hopper discharge experiment. As indicated previously, the ending stage of the discharge process is not shown in the figure because the FEM-ADS model is not appropriate for describing this stage. The figure shows good quantitative agreement between the model predictions and experimental measurements, at least within the experimental scatter. Moreover, different segregation patterns are observed in Figs. 6.8 and 6.11 due to different flow modes. The 55° hopper primarily discharges in funnel flow while the 15° hopper primarily discharges with mass flow behavior. The reasons for these two different segregation patterns were discussed by Ketterhagen et al. [89].

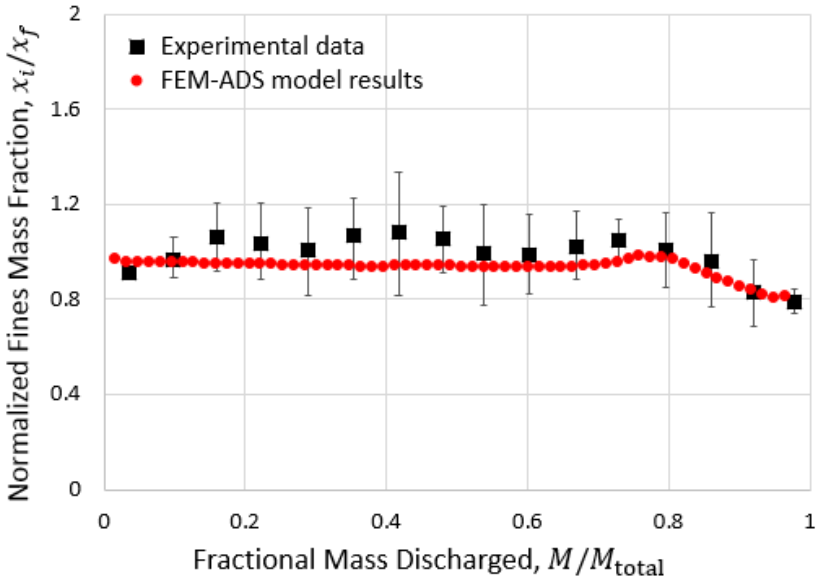

Figure 6.11 Experimental and FEM-ADS model predictions of the normalized mass fraction of fines with respect to the fractional mass discharged. The hopper angle is 15° and the initial fines mass fraction is 10%. Scatter bars denote the 95% confidence interval of the experimental results.

Note that to ensure the convergence of the ADS equation for the hopper simulations, a mesh dependency study was performed using the 15° hopper simulation. The normalized fine mass fraction, as shown in Figure 6.11, was computed using 250,000 and 640,000 elements, respectively. The averaged error among all computed data points is 0.36% and, hence, 250,000 elements were used in the hopper simulation studies.

Finally, the FEM-ADS model is further compared to experiments performed in the 55° hopper with a well-mixed initial fill, but different initial fines mass fractions, namely 20% and 50%. The same large and small particles are used in these experiments. The same diffusion coefficient (D = 2.5 mm^2/s for 55° hopper) and percolation length scale (S = 2 mm) as used previously are used in these new simulations. Figure 6.12 summarizes the good quantitative agreement between the experimental data and model predictions. The total wall-clock time required to run each of these simulations, including the FEM (32 cores with the Intel Xeon CPU E5-2680 v3 processor) and ADS (MATLAB, single core with the same processor) calculations, was two to three days.

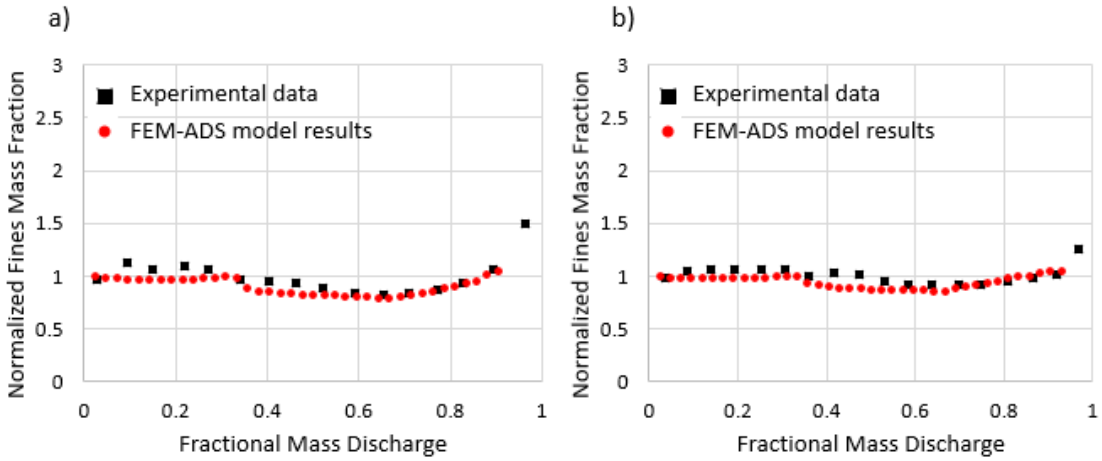

Figure 6.12 Experimental and FEM-ADS model predictions of the normalized mass fraction of fines with respect to the fractional mass discharged. The hopper angle is 55° and the initial fines mass fraction is (a) 20%, and (b) 50%.

6.4 Summary

A two-dimensional transient multi-scale modeling approach for predicting binary segregation in particulate systems was presented in the current chapter. This model is an extension of previous mixing models developed in Chapters 4 and 5, which utilize a finite element method to determine the macroscopic granular velocity field and then combine them with microscopic diffusion correlations using the advection-diffusion equation. The current chapter extends the model by including the segregation correlation using the advection-diffusion-segregation equation. This utility of the multi-scale modelling approach was demonstrated predicting segregation patterns in a rotating drum and the discharge of conical hoppers with different geometries. The model exhibits remarkable quantitative accuracy in predicting DEM and experimental segregation values reported in the literature for cohesionless granular materials.

CHAPTER 7. TWO-WAY COUPLED MULTI-SCALE MIXING MODEL

As mentioned in Chapters 4 to 6, the developed multi-scale model uses a one-way coupled method, which means material properties do not change with concentration. While this assumption is sufficient for previous studies, where the material properties do not change much across the mixture, it could raise problems when modeling mixing and segregation of materials with very different material properties. Hence, to further extend the usage of the one-way coupled multi-scale model, a two-way coupled model is developed where the material properties change with concentration. As a result, the material flow field also changes with concentration.

The multi-scale mixing model introduced in Chapter 4 is used in the current chapter to develop the two-way coupled model. Note that to derive the flow field based on material concentration, all the numerical calculations used to solve the advection-diffusion equation have to take place within the commercial software Abaqus/Explicit. Hence, an Abaqus user subroutine plugin is used to solve the equation within Abaqus for every time increment.

7.1 Abaqus user subroutines

As discussed in Chapter 4, to numerically solve the advection-diffusion equation, the velocity field and material concentration need be updated at every time increment. The Abaqus user subroutine VUSDFLD is used along with the user subroutine VUFIELD to obtain the required information. Details of these user subroutines can be found in Abaqus documentation [62] and are briefly introduce here.

Note that to develop a more efficient and user-friendly plugin, other user subroutines and utility routines are also used. For example, VEXTERNALDB is used to read the user-defined inputs and initiate the program; VGETVRM is used to derive the Eulerian volume fraction (EVF) information, which is discussed in Chapter 4, to define boundary conditions; MUTEXLOCK is used to protect the common blocks from being updated by multiple threads at the same time to ensure that the plug-in is compatible with multi-thread simulations.

7.1.1 VUSDFLD

The user subroutine VUSDFLD allows the redefinition of field variables at a material point as functions of time or any of the available material point quantities. Also, it can call the utility routine VGETVRM to access material point data, like the EVF value. Before the user subroutine VUSDFLD is called, the values of the field variables at the material point are calculated by interpolation from the values defined at the nodes and any changes to the field variables in the user subroutine are local to the material point. Thus, in the plugin, the user subroutine VUSDFLD is only used to derive the EVF values for material points. Common blocks are used to dynamically store the EVF values and transfer to other user subroutines.

Moreover, the user subroutine VUSDFLD can introduce solution-dependent material properties since such properties can be easily defined as functions of field variables. Hence, this user subroutine allows the plugin to define concentration-dependent material properties, which extend the multi-scale model to a two-way coupled method.

7.1.2 VUFIELD

The user subroutine VUFIELD allows one to prescribe predefined field variables at the nodes of a model. Since in the plugin the material concentration is used as a nodal field variable, the main part of the computational work is finished within this user subroutine. Note that in the plugin the two-dimensional advection-diffusion equation is still used due to the computed geometry, which is explained in detail later. Details of the governing equations and numerical methods can be found in Section 4.2.

As discussed previously, the EVF values for every material point are transferred through common blocks from the user subroutine VUSDFLD to VUFIELD. Next, the values derived at the material points are linearly interpolated into the values at the nodal points. These values are used to define the material domain at every time increment and to compute the boundary conditions. The nodal velocities are derived directly within this user subroutine and used to solve the advection-diffusion equation. The corresponding nodal material concentrations are then stored in a common block for use in the next time increment.

7.2 Mixing of materials with the same material properties

To first validate the two-way coupled Abaqus plugin, a rotating drum simulation is used to study the mixing of materials with the same material properties, since the multi-scale model has been proved in Chapter 4 to be quantitatively accurate for the rotating drum simulation. The model geometry and setups are the same as those used in Chapter 4. Material properties listed in Table 4.2 are used here in the FEM simulations, except that the internal friction angle is 35 degree. As shown in Figure 4.5, the drum is filled 50/50 by assigning particles with different colors (red & blue). The one-way coupled multi-scale mixing model, as developed in Chapter 4, is used in the current section to compare with the two-way coupled Abaqus plugin. Note that although the drum used in the FEM simulations is three-dimensional, the material flow within the drum is still two-dimensional due to the symmetric boundary conditions shown in Figure 4.1. Hence, the two-dimensional advection-diffusion equation, as introduced in Section 4.2, is still used in the Abaqus plugin.

Figure 7.1 shows the time evolution of mixing derived from the Abaqus plugin. The colors in the FEM simulation correspond to the value of the field variable, which is the concentration of red particles, with red indicating a large concentration of red particles and blue indicating a small concentration. The results shown in Figure 7.1 are computed by the Abaqus plugin solving the advection-diffusion equation. It is shown that as time increases the degree of mixing increases, with both advection and diffusion contributing to the mixing process. The same trend was found in Chapter 4 as well. Hence, the Abaqus plugin can at least qualitatively predict the mixing process within the rotating drum.

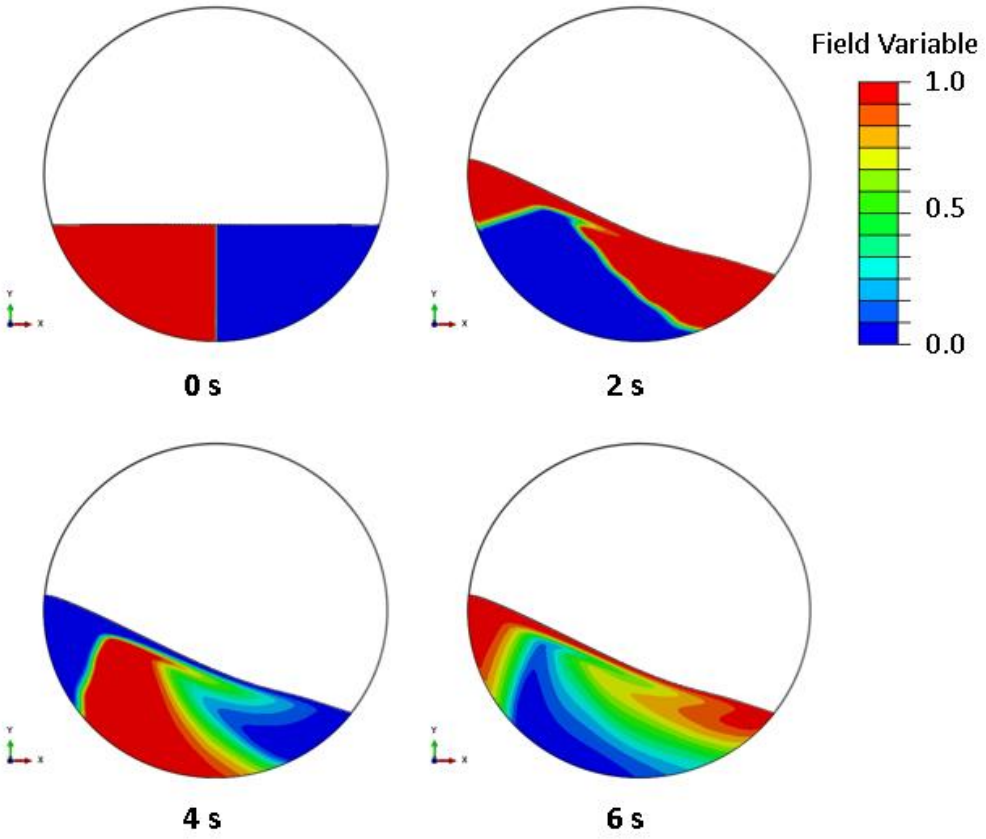

Figure 7.1 Snapshots showing the time evolutions of mixing. The vertical color scale is the red particle concentration. The rotation speed is 6 rpm.

To provide a more quantitative comparison, the segregation intensity I, as defined in Chapter 4, is used to assess the state of mixedness during the simulation. The segregation intensity is plotted in Figure 7.2 as a function of time for both the one-way coupled and two-way coupled multi-scale models using the Matlab program introduced in Chapter 4 and Abaqus plugin introduced in the current section, respectively. Note that for the one-way coupled multi-scale model, as mentioned in Section 4.2, the material concentration at 0.25 revolutions (2.5 s) was used as the initial material concentration. Hence, the segregation intensity for the one-way coupled multi-scale model was not computed for the first 2 seconds. In contrast, the two-way coupled simulation started at 0 seconds, which is not shown in Figure 7.2. Figure 7.2 clearly shows that the two-way coupled Abaqus plugin is quantitatively accurate compared to the one-way coupled multi-scale model. As mentioned before, the slight difference is caused by the different initial states used in the one-way and two-way coupled model. Overall, the results indicate that the advection-diffusion equation can be solved accurately within the Abaqus plugin. Note that the total wall-clock time for the above

two-way coupled Abaqus simulation is about 6-7 days. Future work should focus on further improving the computational efficiency.

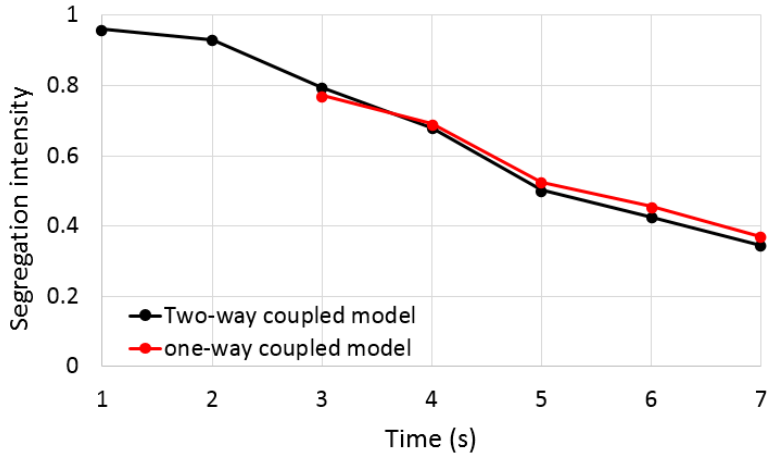

Figure 7.2 The segregation intensity as a function of time for both the one-way and two-way coupled multi-scale model simulations.

7.3 Mixing of materials with different material properties

After validating the two-way coupled Abaqus plugin presented in the previous section, studies are performed to understand the mixing of materials with different material properties. The same rotating drum simulation mentioned in the previous section is used in the current section. The material properties are the same except for the internal friction angle, which is defined as a function of the material concentration. Table 7.1 lists the internal friction angle as a function of the material concentration used in the current two-way coupled simulation. Table 7.1 is derived based on a power law mixing relation used in previous work [94]. Red and blue particles have an internal friction angle of 25 degrees and 35 degrees, respectively. Note that the power law mixing relation [94] used here is for demonstration purposes. Other mixing laws can be applied as required.

Table 7.1 The internal friction angle as a function of the material concentration used in the two-way coupled simulation.

Red particle concentration	Internal friction angle (degree)
0.0	35.0
0.2	32.7
0.4	30.6
0.6	28.6
0.8	26.7
1.0	25.0

Figure 7.3 shows the time evolution of mixing derived from the Abaqus plugin using a) constant internal friction angle of 35 degree and b) varied internal friction angle as listed in Table 7.1. The colors in the FEM simulation correspond to the value of the field variable, which is the concentration of red particles. As mentioned in Chapter 4, the internal friction angle can affect the flow field of the material. Hence, as expected, the state of mixing shown in Figure 7.3(b) is different from the one shown in Figure 7.3(a), due to the difference in the flow field.

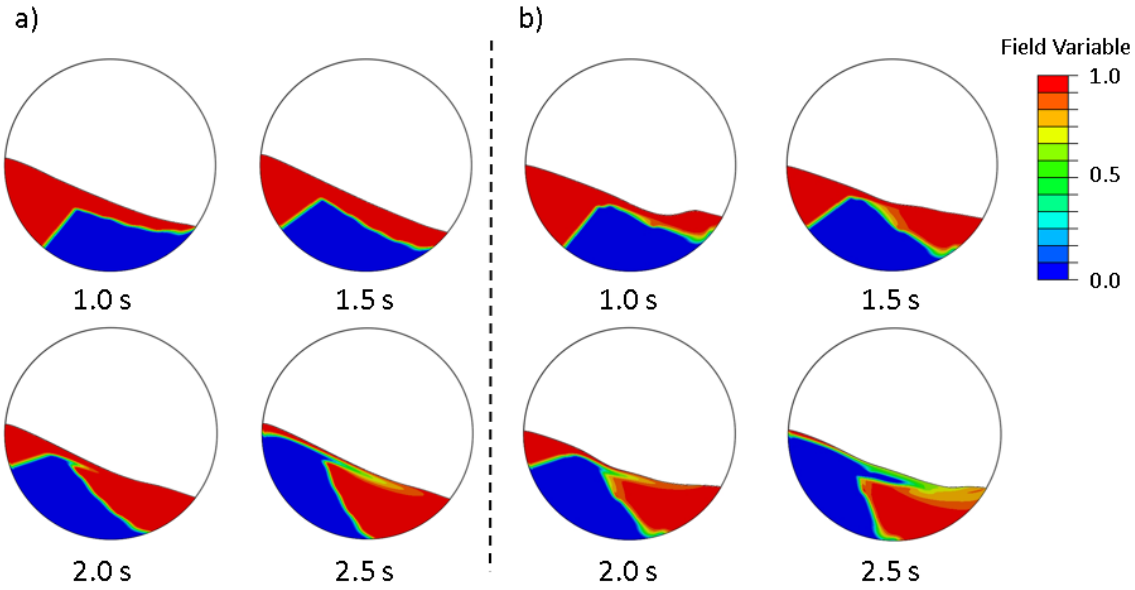

Figure 7.3 Snapshots showing the time evolutions of mixing using (a) constant internal friction angle of 35 degree and (b) varied internal friction angle listed in Table 7.1. The vertical color scale is the red particle concentration.

To further investigate the difference, the segregation intensity is plotted in Figure 7.4 as a function of time for simulations with constant and varied internal friction angles, as used in Figure 7.3. It is shown in Figure 7.4 that the mixing rate is slightly different for simulations with constant and varied internal friction angles after a few seconds (The rotation speed is 6 rpm). Hence, Figs. 7.3 and 7.4 illustrates that the two-way coupled Abaqus plugin is able to predict the mixing of materials with different material properties. Note that the results are only collected for the first few seconds, future work should focus on expanding the current work for a longer time to further illustrate the difference. Also, the change in material properties may have more of an impact in other systems.

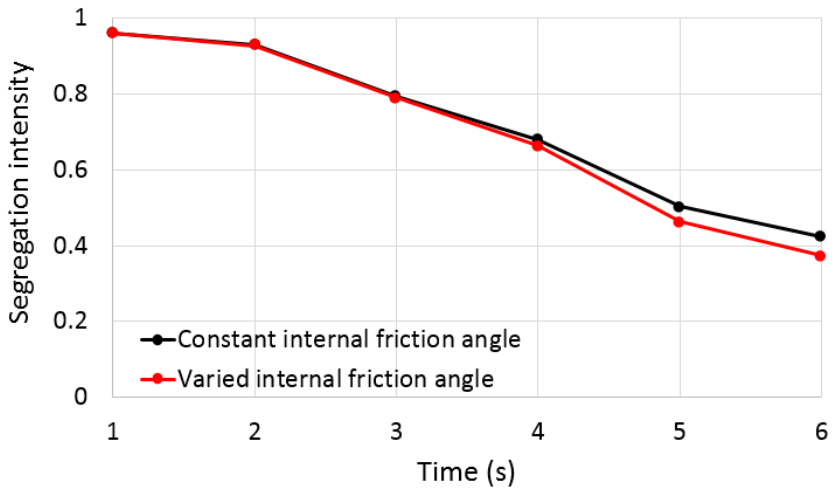

Figure 7.4 The segregation intensity as a function of time for simulations with constant and varied internal friction angles.

7.4 Summary

In the current chapter, a two-way coupled multi-scale modeling approach is described for predicting blending in particulate systems. This model is extended from the multi-scale mixing model developed in Chapters 4 and 5. This model combines, within the advection-diffusion equation, finite element method generated transient macroscopic velocity fields with particle diffusion correlations at a local scale. An Abaqus user subroutine plugin is developed to embed the advection-diffusion equation calculation within Abaqus and thus, allow material properties to change with material concentration. The model is applied here to a two-dimensional rotating drum.

Predictions of the mixing rate from the two-way coupled model are compared with the one-way coupled model. The results show that the mixing rate is different for simulations with constant and varied material properties and the two-way coupled Abaqus plugin is able to predict the mixing of materials with different material properties.

CHAPTER 8. CONCLUSIONS AND FUTURE WORK

8.1 Conclusions

In this work, a new multi-scale approach to modeling particulate mixing and segregation processes is presented. This multi-scale modeling approach combines finite element method simulations to obtain macroscopic velocity fields with calculations from the advection-diffusion equation with computationally and experimentally obtained expressions for particle diffusion at a local scale. The potential of this approach is demonstrated with the studies of mixing in a two-dimensional rotating drum, mixing in a three-dimensional Tote blender, segregation in a two-dimensional rotating drum and segregation in conical hoppers. Predictions of concentration profiles and mixing and segregation rates from the multi-scale model compare well quantitatively to published DEM results and experiments, although the multi-scale model does predict smaller segregation intensities at large times. This inaccuracy is due to the fact that the multi-scale model assumes continuum material behavior and, thus, the asymptotic mixing state corresponds to a perfectly mixed system as opposed to the asymptotic randomly mixed state predicted for the finite sized particles used in DEM simulations or experiments.

A significant advantage of the multi-scale mixing and segregation model over DEM is that the multi-scale model is much faster to calculate. For the case examined in Chapter 4, corresponding to approximately 54,000 particles in the DEM simulation, the multi-scale model required approximately four to five hours of computation while the DEM model required five to six days. The time differences are expected to increase for larger systems since the number of DEM particles increases with the cube of the ratio of the system size to particle size while the FEM nodes increase, at most, only linearly with system size. Furthermore, if particle size is reduced in the DEM simulations, then the integration time step also decreases, further increasing the time required to complete DEM simulations. Hence, the real power of the multi-scale modeling approach is its ability to model industrially-relevant system sizes.

A second advantage of the multi-scale model over DEM is that all of the parameters used in the multi-scale model were measured from independent, standard tests or obtained from the literature.

No back-fitting of the data was used to achieve good modeling accuracy. DEM models require a more complex approach to obtaining particle-level properties, such as complicated individual particle measurements, particularly for particles smaller than 1 mm, or time-consuming calibration simulations.

Parametric studies were performed using the multi-scale model to investigate the influence of various parameters on multi-scale model predictions. Chapter 4 shows that first, the domain mesh size must be increasingly refined as the diffusion constants k_1 and k_2 decrease in order to minimize the influence of numerical diffusion. Second, increasing the internal friction angle decreases the mixing rate due to the decrease in surface speed. Third, the wall friction angle has little influence as long as the material is in an avalanching mode and not slipping against the wall since the free surface remains at the internal friction angle. Fourth, increasing the drum-to-particle diameter ratio decreases the rate at which overall mixing occurs. Fifth, increasing the streamwise and spanwise diffusion constants increases the mixing rate; however, the spanwise diffusion constant dominates in a rotating drum due to the significant spanwise velocity gradient in the active zone. In addition, Chapter 5 shows that the initial loading condition largely affects the mixing rate and advective mixing should be maximized to reach a faster mixing process. Chapter 6 shows that segregation is stronger as the diffusion coefficient decreases and percolation length increases.

Finally, a two-way coupled multi-scale model is introduced in Chapter 7. An Abaqus user subroutine plugin is developed to embed the advection-diffusion equation calculation within Abaqus and thus, allow material properties to change with material concentration. The model is applied to a two-dimensional rotating drum and the results show that the mixing rate is slightly different for the case with variable material properties, at least of the system studied here. There may be other systems where the difference is more significant. Hence, the two-way coupled Abaqus plugin is able to predict the mixing of materials with different material properties.

8.2 Recommendations for future work

Several improvements to the current work should be considered in future studies. First, as introduced in Chapter 6, the current multi-scale segregation model is developed for two-dimensional geometries, since the segregation correlation used in the current work is two-

dimensional. Future work should focus on developing a three-dimensional multi-scale segregation model by considering three-dimensional segregation correlations.

Second, the current work only considers mixing and segregation of two particle species. Future work may expand the governing advection-diffusion-segregation equation to study mixing and segregation of multiple (more than two) particle species [95].

Third, as mentioned in Chapter 4, a second-order Tylor Lax-Wendroff scheme is used in the current work to solve the advection-diffusion-segregation equation due to its simplicity. However, this method may increase the computational cost, especially for the three-dimensional systems. Hence, other numerical methods, such as the matrix mapping method mentioned in Chapter 4, can be used to further improve the computational efficiency.

Fourth, as mentioned in Chapter 7, the current two-way coupled Abaqus user-subroutine plugin is a prototype. Future work should focus on embedding the three-dimensional advection-diffusion-segregation equation into the plugin and using a better numerical method to improve the computational efficiency.

Fifth, the current work uses Mohr-Coulomb constitutive model for granular materials. As mentioned in Chapter 5, there are some simplifications within the Mohr-Coulomb model, such as the model is shear rate-independent, the model cannot predict the formation of shear bands without considering shear localization and the model does not take into account changes in material hardening or softening. Other constitutive models can be used in the future work based on the type of materials used. For example, the extended Mohr-Coulomb model can be used for situations where shear bands are important and the modified Drucker-Prager Cap (DPC) model can be used for systems in which the solid fraction changes significantly [74,75,82].

Also, the current work focuses on mixing and segregation of non-cohesive materials. However, most of the particles used in industry are cohesive. Hence, future work should extend the current model to consider cohesive materials. In fact, as shown in the current work, the Mohr-Coulomb model is able to handle cohesive materials. However, the diffusion and segregation rates are

expected to be smaller in a cohesive material and hence, the mixing and segregation would be dominated by active movement of the material.

Finally, the diffusion constant k_1 and percolation length scale S used in the current work were either derived from literature or back-fitted from experimental data. Future work should develop a simple, standard method to calibrate the diffusion constant and percolation length scale. For example, the unbounded heap flow experiment could be used as a method for calibrating the model parameters [29].

APPENDIX

A flowchart of the image processing algorithm used in Section 5.3 is shown in Figure A1. For each image, the material domains (red and blue glass beads) were extracted using the freeware program ImageJ [96], which was used to identify only the glass beads among a white background. This RGB image was further analyzed to extract only the red component of each image's pixels, with a value ranging between 0 (no red) and 255 (all red). A threshold value of 80 was selected to differentiate between the red and blue pixels. A value larger than 80 indicated that a pixel corresponded to a red particle while a value smaller than 80 indicated that it was a blue particle. This threshold value was chosen to ensure that at any point in time the fraction of red pixels in the entire system was 50±5% since the system consisted of 50% red beads.

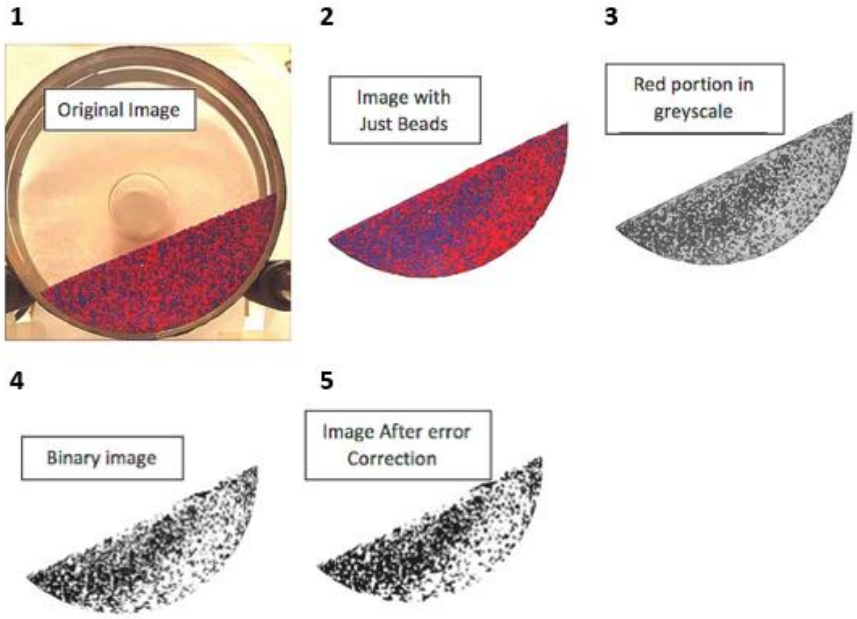

Figure A.1 The image analysis algorithm for a single image. The steps proceed from 1 to 5.

After distinguishing red and blue pixels, a black and white binary image was generated, with black corresponding to the blue pixels and white corresponding to the red ones. Note that since spherical glass beads were used in the experiment, reflections and shadows were introduced due to the light

source. An image correction algorithm was developed in the MATLAB program in an attempt to account for these effects.

The corrected binary image was used to compute the segregation intensity. A non-overlapping grid of square cells was used in the current analysis. The cell size varied from 3 to 10 particle diameters on a side. To avoid using samples containing data outside the cylinder boundary, boundary flags were used to make sure each sample contained at least 95% material. All of the qualified samples were then used to calculate the segregation intensity for the current time step.

REFERENCES

[1] R.Y. Yang, A.B. Yu, L. McElroy, J. Bao, Numerical simulation of particle dynamics in different flow regimes in a rotating drum, Powder Technol. 188 (2008) 170–177. doi:10.1016/j.powtec.2008.04.081.

[2] L.T. Fan, S.J. Chen, C.A. Watson, Solids Mixing, Ind. Eng. Chem. 62 (1970) 53–69. doi:10.1021/ie50727a009.

[3] M. Poux, P. Fayolle, J. Bertrand, D. Bridoux, J. Bousquet, Powder mixing: Some practical rules applied to agitated systems, Powder Technol. 68 (1991) 213–234. doi:10.1016/0032-5910(91)80047-M.

[4] M. Moakher, T. Shinbrot, F.J. Muzzio, Experimentally validated computations of flow, mixing and segregation of non-cohesive grains in 3D tumbling blenders, Powder Technol. 109 (2000) 58–71. doi:10.1016/S0032-5910(99)00227-2.

[5] Y. Xu, C. Xu, Z. Zhou, J. Du, D. Hu, 2D DEM simulation of particle mixing in rotating drum: A parametric study, Particuology. 8 (2010) 141–149. doi:10.1016/j.partic.2009.10.003.

[6] B.K. Mishra, A review of computer simulation of tumbling mills by the discrete element method: Part I-contact mechanics, Int. J. Miner. Process. 71 (2003) 73–93. doi:10.1016/S0301-7516(03)00032-2.

[7] K. Yamane, Discrete-element method application to mixing and segregation model in industrial blending system, J. Mater. Res. 19 (2004) 623–627. doi:10.1557/jmr.2004.19.2.623.

[8] M. Kwapinska, G. Saage, E. Tsotsas, Mixing of particles in rotary drums: A comparison of discrete element simulations with experimental results and penetration models for thermal processes, Powder Technol. 161 (2006) 69–78. doi:10.1016/j.powtec.2005.08.038.

[9] X. Liu, W. Ge, Y. Xiao, J. Li, Granular flow in a rotating drum with gaps in the side wall, Powder Technol. 182 (2008) 241–249. doi:10.1016/j.powtec.2007.06.029.

[10] R.K. Rajamani, B.K. Mishra, R. Venugopal, A. Datta, Discrete element analysis of tumbling mills, Powder Technol. 109 (2000) 105–112. doi:10.1016/S0032-5910(99)00230-2.

[11] P.Y. Liu, R.Y. Yang, A.B. Yu, DEM study of the transverse mixing of wet particles in rotating drums, Chem. Eng. Sci. 86 (2013) 99–107. doi:10.1016/j.ces.2012.06.015.

[12] Z. Asaf, D. Rubinstein, I. Shmulevich, Determination of discrete element model parameters required for soil tillage, Soil Tillage Res. 92 (2007) 227–242. doi:10.1016/j.still.2006.03.006.

[13] G.K.P. Barrios, R.M. de Carvalho, A. Kwade, L.M. Tavares, Contact parameter estimation for DEM simulation of iron ore pellet handling, Powder Technol. 248 (2013) 84–93. doi:10.1016/j.powtec.2013.01.063.

[14] C.J. Coetzee, D.N.J. Els, G.F. Dymond, Discrete element parameter calibration and the modelling of dragline bucket filling, J. Terramechanics. 47 (2010) 33–44. doi:10.1016/j.jterra.2009.03.003.

[15] A. Rosato, K.J. Strandburg, F. Prinz, R.H. Swendsen, Why the Brazil nuts are on top: Size segregation of particulate matter by shaking, Phys. Rev. Lett. 58 (1987) 1038–1040. doi:10.1103/PhysRevLett.58.1038.

[16] J.B. Knight, H.M. Jaeger, S.R. Nagel, Vibration-induced size separation in granular media: The convection connection, Phys. Rev. Lett. 70 (1993) 3728–3731. doi:10.1103/PhysRevLett.70.3728.

[17] A.E.E. Ehrichs, H.M. Jaeger, G.S. Karczmar, J.B. Knight, V. Yu, Granular Convection Observed by Magnetic Resonance Imaging, Science (80-.). 267 (1995) 1632–1634.

[18] M. Schröter, S. Ulrich, J. Kreft, J.B. Swift, H.L. Swinney, Mechanisms in the size segregation of a binary granular mixture, Phys. Rev. E - Stat. Nonlinear, Soft Matter Phys. 74 (2006) 1–14. doi:10.1103/PhysRevE.74.011307.

[19] S.B. Savage, C.K.K. Lun, Particle size segregation in inclined chute flow of dry cohesionless granular solids, J. Fluid Mech. 189 (1988) 311–335. doi:10.1017/S002211208800103X.

[20] J.M. Ottino, D. V Khakhar, mixing and Segregation of Granular Materials, Annu. Rev. Fluid Mech. 32 (2000) 55–91.

[21] S.W. Meier, R.M. Lueptow, J.M. Ottino, A dynamical systems approach to mixing and segregation of granular materials in tumblers, Adv. Phys. 56 (2007) 757–827. doi:10.1080/00018730701611677.

[22] J.C. Williams, The mixing of dry powders, Powder Technol. 2 (1968) 13–20. doi:10.1016/0032-5910(68)80028-2.

[23] Gerard Viner Middleton, Experimental studies related to problems of flysch sedimentation, Geological Association of Canada, Toronto, 1970.

[24] J.A. Drahun, J. Bridgwater, The mechanisms of free surface segregation, Powder Technol. 36 (1983) 39–53. doi:10.1016/0032-5910(83)80007-2.

[25] Y. Fan, K.M. Hill, Shear-driven segregation of dense granular mixtures in a split-bottom cell, Phys. Rev. E - Stat. Nonlinear, Soft Matter Phys. 81 (2010) 1–12. doi:10.1103/PhysRevE.81.041303.

[26] J.M.N.T. Gray, Particle Segregation in Dense Granular Flows, Annu. Rev. Fluid Mech. 50 (2018) 407–433. doi:10.1146/annurev-fluid-122316.

[27] A. Sarkar, C.R. Wassgren, Effect of particle size on flow and mixing in a bladed granular mixer, AIChE J. 61 (2015) 46–57. doi:10.1002/aic.14629.

[28] R. Chandratilleke, A. Yu, J. Bridgwater, K. Shinohara, Flow and mixing of cohesive particles in a vertical bladed mixer, Ind. Eng. Chem. Res. 53 (2014) 4119–4130. doi:10.1021/ie403877v.

[29] Y. Fan, P.B. Umbanhowar, J.M. Ottino, R.M. Lueptow, Shear-Rate-Independent Diffusion in Granular Flows, Phys. Rev. Lett. 115 (2015) 1–5. doi:10.1103/PhysRevLett.115.088001.

[30] N. Khola, C. Wassgren, Correlations for shear-induced percolation segregation in granular shear flows, Powder Technol. 288 (2016) 441–452. doi:10.1016/j.powtec.2015.11.003.

[31] Y. Fan, C.P. Schlick, P.B. Umbanhowar, J.M. Ottino, R.M. Lueptow, Modelling size segregation of granular materials: The roles of segregation, advection and diffusion, J. Fluid Mech. 741 (2014) 252–279. doi:10.1017/jfm.2013.680.

[32] A. Tripathi, D. V. Khakhar, Density difference-driven segregation in a dense granular flow, J. Fluid Mech. 717 (2013) 643–669. doi:10.1017/jfm.2012.603.

[33] J. Bridgwater, D.F. Bagster, S.F. Chen, J.H. Hallam, Geometric and dynamic similarity in particle mixing, Powder Technol. 2 (1969) 198–206. doi:10.1016/0032-5910(69)80013-6.

[34] J. Bridgwater, W.S. Foo, D.J. Stephens, Particle mixing and segregation in failure zones-theory and experiment, Powder Technol. 41 (1985) 147–158. doi:10.1016/0032-5910(85)87033-9.

[35] J.M.N.T. Gray, V.A. Chugunov, Particle-size segregation and diffusive remixing in shallow granular avalanches, 2006. doi:10.1017/S0022112006002977.

[36] J.M.N.T. Gray, A.R. Thornton, A theory for particle size segregation in shallow granular free-surface flows, Proc. R. Soc. A Math. Phys. Eng. Sci. 461 (2005) 1447–1473. doi:10.1098/rspa.2004.1420.

[37] L.B.H. May, L.A. Golick, K.C. Phillips, M. Shearer, K.E. Daniels, Shear-driven size segregation of granular materials: Modeling and experiment, Phys. Rev. E - Stat. Nonlinear, Soft Matter Phys. 81 (2010) 2–9. doi:10.1103/PhysRevE.81.051301.

[38] B. Marks, P. Rognon, I. Einav, Grainsize dynamics of polydisperse granular segregation down inclined planes, J. Fluid Mech. 690 (2012) 499–511. doi:10.1017/jfm.2011.454.

[39] J. Kowalski, J.N. McElwaine, Shallow two-component gravity-driven flows with vertical variation, J. Fluid Mech. 714 (2013) 434–462. doi:10.1017/jfm.2012.489.

[40] S. Wiederseiner, N. Andreini, G. Épely-Chauvin, G. Moser, M. Monnereau, J.M.N.T. Gray, C. Ancey, Experimental investigation into segregating granular flows down chutes, Phys. Fluids. 23 (2011) 1–10. doi:10.1063/1.3536658.

[41] K. Van Der Vaart, P. Gajjar, G. Epely-Chauvin, N. Andreini, J.M.N.T. Gray, C. Ancey, Underlying Asymmetry within Particle Size Segregation, Phys. Rev. Lett. 114 (2015) 1–5. doi:10.1103/PhysRevLett.114.238001.

[42] C.P. Schlick, Y. Fan, P.B. Umbanhowar, J.M. Ottino, R.M. Lueptow, Granular segregation in circular tumblers: Theoretical model and scaling laws, J. Fluid Mech. 765 (2015) 632–652. doi:10.1017/jfm.2015.4.

[43] H. Xiao, P.B. Umbanhowar, J.M. Ottino, R.M. Lueptow, Modelling density segregation in flowing bidisperse granular materials, Proc. R. Soc. A Math. Phys. Eng. Sci. 472 (2016) 20150856. doi:10.1098/rspa.2015.0856.

[44] D.G. Schaeffer, Instability in the evolution equations describing incompressible granular flow, J. Differ. Equ. 66 (1987) 19–50. doi:10.1016/0022-0396(87)90038-6.

[45] M. Farzaneh, A.E. Almstedt, F. Johnsson, D. Pallarès, S. Sasic, The crucial role of frictional stress models for simulation of bubbling fluidized beds, Powder Technol. 270 (2015) 68–82. doi:10.1016/j.powtec.2014.09.050.

[46] Y. Forterre, O. Pouliquen, Flows of Dense Granular Media, Annu. Rev. Fluid Mech. 40 (2008) 1–24. doi:10.1146/annurev.fluid.40.111406.102142.

[47] S. Schneiderbauer, A. Aigner, S. Pirker, A comprehensive frictional-kinetic model for gas-particle flows: Analysis of fluidized and moving bed regimes, Chem. Eng. Sci. 80 (2012) 279–292. doi:10.1016/j.ces.2012.06.041.

[48] M. Khalilitehrani, P.J. Abrahamsson, A. Rasmuson, Modeling dilute and dense granular flows in a high shear granulator, Powder Technol. 263 (2014) 45–49. doi:10.1016/j.powtec.2014.04.088.

[49] R. Artoni, A. Santomaso, P. Canu, Simulation of dense granular flows: Dynamics of wall stress in silos, Chem. Eng. Sci. 64 (2009) 4040–4050. doi:10.1016/j.ces.2009.06.008.

[50] S. Volpato, R. Artoni, A.C. Santomaso, Numerical study on the behavior of funnel flow silos with and without inserts through a continuum hydrodynamic approach, Chem. Eng. Res. Des. 92 (2014) 256–263. doi:10.1016/j.cherd.2013.07.030.

[51] S. Volpato, P. Canu, A.C. Santomaso, Simulation of free surface granular flows in tumblers, Adv. Powder Technol. 28 (2017) 1028–1037. doi:10.1016/j.apt.2017.01.007.

[52] T. Tian, J. Su, J. Zhan, S. Geng, G. Xu, X. Liu, Discrete and continuum modeling of granular flow in silo discharge, Particuology. 36 (2018) 127–138. doi:10.1016/j.partic.2017.04.001.

[53] P. Vidal, E. Gallego, M. Guaita, F. Ayuga, Finite element analysis under different boundary conditions of the filling of cylindrical steel silos having an eccentric hopper, J. Constr. Steel Res. 64 (2008) 480–492. doi:10.1016/j.jcsr.2007.08.005.

[54] Y. Wang, Y. Lu, J.Y. Ooi, Finite element modelling of wall pressures in a cylindrical silo with conical hopper using an Arbitrary Lagrangian-Eulerian formulation, Powder Technol. 257 (2014) 181–190. doi:10.1016/j.powtec.2014.02.051.

[55] Y. Wang, Y. Lu, J.Y. Ooi, A numerical study of wall pressure and granular flow in a flat-bottomed silo, Powder Technol. 282 (2015) 43–54. doi:10.1016/j.powtec.2015.01.078.

[56] Q.J. Zheng, A.B. Yu, Modelling the granular flow in a rotating drum by the Eulerian finite element method, Powder Technol. 286 (2015) 361–370. doi:10.1016/j.powtec.2015.08.025.

[57] Q.J. Zheng, A.B. Yu, Finite element investigation of the flow and stress patterns in conical hopper during discharge, Chem. Eng. Sci. 129 (2015) 49–57. doi:10.1016/j.ces.2015.02.022.

[58] Q.J. Zheng, B.S. Xia, R.H. Pan, A.B. Yu, Prediction of mass discharge rate in conical hoppers using elastoplastic model, Powder Technol. 307 (2017) 63–72. doi:10.1016/j.powtec.2016.11.037.

[59] D. Bertuola, S. Volpato, P. Canu, A.C. Santomaso, Prediction of segregation in funnel and mass flow discharge, Chem. Eng. Sci. 150 (2016) 16–25. doi:10.1016/j.ces.2016.04.054.

[60] S.K. Hajra, D. Shi, J.J. McCarthy, Granular mixing and segregation in zigzag chute flow, Phys. Rev. E - Stat. Nonlinear, Soft Matter Phys. 86 (2012) 1–7. doi:10.1103/PhysRevE.86.061318.

[61] L. Bai, Q.J. Zheng, A.B. Yu, FEM simulation of particle flow and convective mixing in a cylindrical bladed mixer, Powder Technol. 313 (2017) 175–183. doi:10.1016/j.powtec.2017.03.018.

[62] Dassault Systèmes, Abaqus analysis user's manual, Rhode Island, 2007.

[63] K. Kamrin, G. Koval, Nonlocal constitutive relation for steady granular flow, Phys. Rev. Lett. 108 (2012) 1–5. doi:10.1103/PhysRevLett.108.178301.

[64] T. Barker, J.M.N.T. Gray, Partial regularisation of the incompressible μ(I)-rheology for granular flow, J. Fluid Mech. 828 (2017) 5–32. doi:10.1017/jfm.2017.428.

[65] I.C. Christov, J.M. Ottino, R.M. Lueptow, From streamline jumping to strange eigenmodes: Bridging the Lagrangian and Eulerian pictures of the kinematics of mixing in granular flows, Phys. Fluids. 23 (2011) 1–16. doi:10.1063/1.3653280.

[66] B. Utter, R.P. Behringer, Self-diffusion in dense granular shear flows, Phys. Rev. E - Stat. Nonlinear, Soft Matter Phys. 69 (2004) 1–12. doi:10.1103/PhysRevE.69.031308.

[67] S.-S. Hsiau, Y.-M. Shieh, Fluctuations and self-diffusion of sheared granular material flows, J. Rheol. (N. Y. N. Y). 43 (1999) 1049–1066. doi:10.1122/1.551027.

[68] C.S. CAMPBELL, Self-diffusion in granular shear flows, J. Fluid Mech. 348 (1997) S0022112097006496. doi:10.1017/S0022112097006496.

[69] M.K. Singh, O.S. Galaktionov, H.E.H. Meijer, P.D. Anderson, A simplified approach to compute distribution matrices for the mapping method, Comput. Chem. Eng. 33 (2009) 1354–1362. doi:10.1016/j.compchemeng.2009.01.021.

[70] E. Sousa, Finite differences for the convection-diffusion equation: On stability and boundary conditions, University of Oxford, 2001.

[71] T.J. Chung, Computational Fluid Dynamics, Cambridge University Press, Cambridge, 2015.

[72] P. Jop, Y. Forterre, O. Pouliquen, Crucial role of sidewalls in granular surface flows: Consequences for the rheology, J. Fluid Mech. 541 (2005) 167–192. doi:10.1017/S0022112005005987.

[73] S. Swaminathan, J. Hilden, B. Ramey, C. Wassgren, Modeling the Formation of Debossed Features on a Pharmaceutical Tablet, J. Pharm. Innov. 11 (2016) 214–230. doi:10.1007/s12247-016-9257-6.

[74] Y. Liu, C. Wassgren, Modifications to Johanson's roll compaction model for improved relative density predictions, Powder Technol. 297 (2016) 294–302. doi:10.1016/j.powtec.2016.04.017.

[75] A.R. Muliadi, J.D. Litster, C.R. Wassgren, Validation of 3-D finite element analysis for predicting the density distribution of roll compacted pharmaceutical powder, Powder Technol. 237 (2013) 386–399. doi:10.1016/j.powtec.2012.12.023.

[76] A.A. Boateng, Boundary layer modeling of granular flow in the transverse plane of a partially filled rotating cylinder, Int. J. Multiph. Flow. 24 (1998) 499–521. doi:10.1016/S0301-9322(97)00065-7.

[77] P. V. Danckwerts, The effect of incomplete mixing on homogeneous reactions, Chem. Eng. Sci. 8 (1958) 93–102. doi:10.1016/0009-2509(58)80040-8.

[78] P. V. Danckwerts, The definition and measurement of some characteristics of mixtures, Appl. Sci. Res. Sect. A. 3 (1952) 279–296. doi:10.1007/BF03184936.

[79] S. Swaminathan, B. Ramey, J. Hilden, C. Wassgren, Characterizing the powder punch-face adhesive interaction during the unloading phase of powder compaction, Powder Technol. 315 (2017) 410–421. doi:10.1016/j.powtec.2017.04.003.

[80] Y. Liu, M. Gonzalez, C. Wassgren, Modeling granular material blending in a rotating drum using a finite element method and advection-diffusion equation multiscale model, AIChE J. 64 (2018) 3277–3292. doi:10.1002/aic.16179.

[81] O.S. Sudah, P.E. Arratia, A. Alexander, F.J. Muzzio, Simulation and experiments of mixing and segregation in a tote blender, AIChE J. 51 (2005) 836–844. doi:10.1002/aic.10448.

[82] J.P. Bardet, Orientation of Shear Bands in Frictional Soils, J. Eng. Mech. 117 (1991) 1466–1485. doi:10.1061/(ASCE)0733-9399(1991)117:7(1466).

[83] O.C. Zienkiewicz, R.L. Taylor, J.M. Too, Reduced integration technique in general analysis of plates and shells, Int. J. Numer. Methods Eng. 3 (1971) 275–290. doi:10.1002/nme.1620030211.

[84] Y. Liu, X. Guo, H. Lu, X. Gong, An investigation of the effect of particle size on the flow behavior of pulverized coal, Procedia Eng. 102 (2015) 698–713. doi:10.1016/j.proeng.2015.01.170.

[85] E.M. Kara, Contribution of particles size ranges to sand friction, Eng. Technol. Appl. Sci. Res. 3 (2013) 497–501.

[86] F. Podczeck, Y. Miah, The influence of particle size and shape on the angle of internal friction and the flow factor of unlubricated and lubricated powders, Int. J. Pharm. 144 (1996) 187–194. doi:10.1016/S0378-5173(96)04755-2.

[87] A. Castellanos, C. Soria-Hoyo, J.M. Valverde, M.A.S. Quintanill, Cohesion and internal friction of fine glass beads as affected by small intensity vertical vibration, AIP Conf. Proc. 1145 (2009) 707–710. doi:10.1063/1.3180025.

[88] N. Mitarai, F. Nori, Wet granular materials, Adv. Phys. 55 (2006) 1–45. doi:10.1080/00018730600626065.

[89] W.R. Ketterhagen, J.S. Curtis, C.R. Wassgren, A. Kong, P.J. Narayan, B.C. Hancock, Granular segregation in discharging cylindrical hoppers: A discrete element and experimental study, Chem. Eng. Sci. 62 (2007) 6423–6439. doi:10.1016/j.ces.2007.07.052.

[90] Y. Liu, A.T. Cameron, M. Gonzalez, C. Wassgren, Modeling granular material blending in a Tote blender using a finite element method and advection-diffusion equation multi-scale model, Powder Technol. 340 (2018) 428–439. doi:10.1016/j.powtec.2018.09.033.

[91] Y. Liu, M. Gonzalez, C. Wassgren, Modeling granular material segregation using a combined finite element method and advection-diffusion-segregation equation model, (2018). http://arxiv.org/abs/1810.02794.

[92] D.J. Benson, S. Okazawa, Contact in a multi-material Eulerian finite element formulation, Comput. Methods Appl. Mech. Eng. 193 (2004) 4277–4298. doi:10.1016/j.cma.2003.12.061.

[93] N. Christakis, M.K. Patel, M. Cross, J. Baxter, H. Abou-Chakra, U. Tüzün, Predictions of segregation of granular material with the aid of PHYSICA, a 3-D unstructured finite-volume modelling framework, Int. J. Numer. Methods Fluids. 40 (2002) 281–291. doi:10.1002/fld.319.

[94] A. Michrafy, M. Michrafy, M.S. Kadiri, J.A. Dodds, Predictions of tensile strength of binary tablets using linear and power law mixing rules, Int. J. Pharm. 333 (2007) 118–126. doi:10.1016/j.ijpharm.2006.10.008.

[95] C.P. Schlick, A.B. Isner, B.J. Freireich, Y. Fan, P.B. Umbanhowar, J.M. Ottino, R.M. Lueptow, A continuum approach for predicting segregation in flowing polydisperse granular materials, J. Fluid Mech. 797 (2016) 95–109. doi:10.1017/jfm.2016.260.

[96] C.A. Schneider, W.S. Rasband, K.W. Eliceiri, NIH Image to ImageJ : 25 years of image analysis HISTORICAL commentary NIH Image to ImageJ : 25 years of image analysis, Nat. Methods. 9 (2012) 671–675. doi:10.1038/nmeth.2089.

VITA

Yu Liu obtained his Bachelor's degree in Mechanical Engineering from Shanghai Jiao Tong University in May 2015. He was accepted in the Master's program in the School of Mechanical Engineering at Purdue University in September 2015. He worked with Prof. Carl Wassgren in Purdue's Center for Particulate Products and Processes (CP3), and obtained a Master's degree in May 2016. He continued with his PhD with Prof. Carl Wassgren and Prof. Marcial Gonzalez and is expected to obtain his degree in December 2018. Yu is a recipient of the Bilsland Dissertation Fellowship from College of Engineering at Purdue. While in graduate school he did two internships at The Dow Chemical Company (Midland, MI) and Genentech, Inc. (South San Francisco, CA). Yu accepted a position at The Dow Chemical Company in Lake Jackson, TX and is expected to begin in February 2019.